ABSTRACT

NEUTRON YIELDS FROM PROTON
BOMBARDMENT OF THICK TARGETS

Stopping targets of natural C, Al, Cu, Ag, Ta and Pb were bombarded by 22, 30, and 40 MeV protons, and the resulting neutron energy spectra were measured by the time-of-flight technique at laboratory angles of 0, 30, 60, 90, 120, and 150 degrees.

The data may be used in practical experimental situations where thick target neutron yields are needed, for example, in shielding or neutron background calculations. The data also provide useful information in the area of nuclear reaction mechanisms, specifically, the magnitudes of and competition between compound nuclear reactions and reactions which do not proceed via compound nucleus formation.

Also, extensive information is provided on the design and construction of the experimental neutron time-of-flight facility used, with a view toward assisting interested physicists to operate such a facility, or to design, construct, and operate their own facility.

Analysis of the data indicates that non-compound processes increase in importance rapidly with increasing bombarding energy, until at 40 MeV approximately 20% of all reactions resulting in neutron emission are non-compound reactions, at least in the heavy elements (A>60). For the light elements C and Al, no clear distinction between the two types of processes could be made.

For the heavier elements it was found that the statistical fermi-gas model of the compound nucleus adequately describes the neutron energy spectra for neutron energies less than ~6 MeV. At higher neutron energies the spectra can be explained qualitatively by pre-equilibrium models, currently under development. It appears that further refinements in these models will yield better quantitative agreement between experiment and theory, although current agreement is not unreasonable.

NEUTRON YIELDS FROM PROTON BOMBARDMENT OF THICK TARGETS

by

Thomas Marshall Amos, Jr.

A THESIS

Submitted to
Michigan State University
in partial fulfillment of the requirements
for the degree of

DOCTOR OF PHILOSOPHY

Department of Physics

1972

ACKNOWLEDGEMENTS

I would like to thank my thesis advisor, Professor Aaron Galonsky, for his guidance. His encouragement, advice, and assistance were indispensible to the completion of this work.

To Professor Robert J. Sprafka and his wife, Sally, I give thanks for their personal concern and advice during the course of this work.

I gratefully acknowledge the assistance of Dr. R. K. Jolly and Mr. Robert Doering in taking the data, and the assistance of Mary Kay Zigrang in data reduction and analysis.

For their assistance in construction of the experimental apparatus and in running the cyclotron, I thank the cyclotron technical staff, especially Mr. Norval Mercer and his machine shop staff.

I would also like to thank the National Science Foundation and Michigan State University for their financial support.

TABLE OF CONTENTS

		Page
ACKNOWLEDGEMENTS		ii
LIST OF FIGURES		v
LIST OF TABLES		vii
Chapter		
I.	INTRODUCTION	1
II.	THE EVAPORATION THEORY OF COMPOUND NUCLEUS DECAY	5
	A. Basic Statistical Arguments	5
	B. The Fermi Gas Model Of The Nucleus	10
III.	APPLICATION OF THE STATISTICAL-FERMI-GAS MODEL TO THE PRESENT EXPERIMENTAL PROBLEM	12
	A. The Inelastic Collision Probability And Assumptions Concerning Compound Nucleus Formation	12
	B. Procedure Used In Calculating Absolute Thick Target Neutron Spectra And Yields	13
IV.	THE EXPERIMENT	20
	A. Measurement Of Neutron Energy Spectra By The Time-Of-Flight Technique	20
	1. General Comments On The Time-Of-Flight Technique	20
	2. Experimental Design And Procedure	25
	3. The Detector	28
	4. The Time-Of-Flight Electronics	31
	5. Pulse Shape Discrimination	34
	a. Application To Neutron Time-Of-Flight	34
	b. Basis Of The Pulse Shape Effect	35
	c. Electronics	36
	B. Beam Line	44
	C. Targets And Target Chamber	47
	D. Charge Collection And Integration	50
	E. Data Acquisition	51

Page

F. Data Reduction 51
1. Conversion Of Time-Of-Flight Spectra To Energy Spectra 51
2. Calculation of Detector Efficiency 54
a. Statement Of The Problem 54
b. Measurement Of Detector Threshold And Light Resolution 55
c. Measurement Of Detector Response Function 65
G. Corrections 69
1. Absorption And Inscattering 69
2. Deadtime Correction 72
H. Absolute Neutron Yield Spectra, Angular Distributions And Total Yields 75
I. Estimate Of Experimental Uncertainties 101

V. DATA ANALYSIS 103

A. Extraction Of Nuclear Level Density and Radius Parameters 103
B. Extraction Of Neutron Yields From Non-Compound Processes 110

VI. CONCLUSIONS 127

REFERENCES 130

APPENDIX 133

LIST OF FIGURES

Figures		Page
1.	Neutron Evaporation Decay Chain	18
2.	Exploded View of Detector	22
3.	Overall Resolution as a Function of Neutron Energy	24
4.	Overlap Effect	26
5.	Schematic of Detector	30
6.	Time-of-Flight Electronics	32
7.	Pulse Shape Discrimination Electronics	38
8.	Pulse Shape Discriminator Cross-Over Time Spectrum	41
9.	Two-Dimensional Pulse Shape Discrimination Display	42
10.	Three-Dimensional Pulse Shape Discrimination Display	43
11.	Time-of-Flight Spectrum Measured with Pulse Shape Discrimination	45
12.	Beam Line Layout	46
13.	Target Chamber Assembly	49
14.	Typical Neutron and Gamma-Ray Time-of-Flight Spectra	52
15.	Calculated Neutron Detection Efficiencies	56
16a.	^{60}Co and ^{57}Co Compton Recoil Spectra	57
16b.	^{60}Co and ^{57}Co Compton Recoil Spectra	58
17.	Single Channel Analyzer Calibration Curve	60
18.	Single Channel Analyzer Calibration Curve	61
19.	^{60}Co Compton Recoil Spectrum Showing Detector Light Resolution	63
20.	Detector Light Resolution Curve	64

Figures Page

21a. Proton Recoil Energy and Pulse Height Spectra 66

21b. Proton Recoil Energy and Pulse Height Spectra 66

22. Relative Neutron Energy Spectrum 68

23. Detector Response Curve 70

24. Target Geometry for Corrections 73

25. Neutron Yield Spectra 76

26. Neutron Angular Distributions 94

27. Neutron Total Yields 100

28. Comparison Between Evaporation Theory and Experimental Data. The Solid Curves Represent the Data. 104

29. Extracted Nuclear Level Density Parameters as a Function of Mass Number 106

30. Extracted Nuclear Radius Parameters as a Function of Mass Number 108

31. Differential Neutron Energy Spectra with Extrapolated Evaporation Spectra 112

32. Non-Compound Neutron Angular Distributions 114

33. Total Non-Compound Neutron Yields 115

34. Probability for Collision Resulting in Pre-Equilibrium Neutron Emission 120

35. Theoretical and Experimental Angular-Integrated Neutron Energy Spectra 122

36. Angular Integrated Neutron Energy Spectra 124

LIST OF TABLES

Table | Page

1. Gamma-Ray Sources, Their Decay Energies, and Compton Edge Energies 62

2. Absorption and Inscattering Corrections for 2.0 MeV Neutrons at Neutron Angle of 120° at Ep = 30 MeV 74

I. INTRODUCTION

Nuclear reactions at moderate proton bombarding energies (<100 MeV) are usually characterized as either "direct", or "non-compound" reactions or "compound nuclear" reactions. In purely direct reactions, the time interval between the impact of the incident proton upon the target nucleus and the emergence of an outgoing particle is close in order of magnitude to the transit time of a nucleon across the nucleus (10^{-22} sec), and the outgoing particle generally carries away a large fraction of the available excitation energy. In strictly compound nuclear reactions, on the other hand, particle emission occurs after a much longer interval has elapsed (10^{-16} sec); this interval is sufficiently long that the incident particle and target nucleus may be considered to amalgamate and form a "compound nucleus" in which the available excitation energy is shared equally, on the average, among all nucleons present (Bo 36). In reaching this dynamic equilibrium, the compound nucleus loses all knowledge of the details of its formation and is required only to obey general conservation laws. The compound nucleus decays when fluctuations from this equilibrium concentrate enough energy on a particular particle that it is able to escape from the nucleus, at high excitation energies taking away only a small fraction of the total available energy.

The two types of reactions have distinctive characteristics which manifest their occurrence. Outgoing particles resulting from non-compound reactions are in general high energy particles, and their angular distributions are forward peaked in the center of mass system. Non-compound reaction cross sections also exhibit reasonably smooth behavior as a function

of bombarding energy. Compound nuclear reactions result in low energy particles, have isotropic angular distributions in the center of mass system, and their cross sections fluctuate rapidly as a function of bombarding energy.

Compound nuclear reactions are dominant at proton bombarding energies of the order of nucleon binding energies (typically somewhat less than 10 MeV), whereas non-compound reactions are usually considered to become significant at energies greater than roughly 20 MeV. There is, however, no particular energy at which compound nuclear reactions abruptly cease to occur, and there has been available only scant experimental information on the actual competition between the two processes at higher bombarding energies.

Any thorough experimental attempt to determine this competition quantitatively for a given reaction at a given bombarding energy entails measurement of complete energy spectra of the outgoing particles, from the maximum possible energy down to zero; the energy spectra should be taken over a wide range of angles. In such a case, the distinguishing features of compound and non-compound reactions may then be employed as guides to determining the magnitudes of the contributions of the two different processes to the experimental results. If the bombarding energy is varied, new insight into the energy dependence of nuclear reaction processes may be gained.

Although they present formidable experimental difficulties, reactions involving neutrons as the emitted particle are quite significant with regard to the above discussion, since the dominant process for decay of most compound nuclei is neutron emission. Charged particle emission is strongly inhibited by the Coulomb barrier, and for this

reason the contribution from charged particles of all types is small for the great majority of cases.

Previous measurements of neutron yields from proton bombardment of a large number of targets have been made (Ta 57), but these were measurements of total yields only. With such integral information it is not possible to draw convincing conclusions regarding compound and non-compound processes. Recently, Wood et al (Wo 65) and Verbinski and Burrus (Ve 71) have obtained neutron energy spectra and angular distributions from thin targets in the proton bombarding energy range from 8 to 21 MeV; but until the present measurements were made, such data had not been taken at higher bombarding energies.

This paper reports the results of a systematic survey of neutron production by 22, 30, and 40 MeV protons. Six targets, C, Al, Cu, Ag, Ta, and Pb were bombarded, and the neutron yields measured as time-of-flight spectra at each of six angles per target, for neutron energies above 0.5 MeV. The data are presented as absolute neutron energy spectra, and additionally as energy-integrated angular distributions, and energy- and angle-integrated total yields.

Comparison of the data to predictions of the statistical-fermi-gas model of the compound nucleus, adapted to the present experimental case, gives specific quantitative information concerning the competition between compound and direct processes, both of which were observed in the experiment.

In addition, the data are valuable in various practical applications; design of accelerator shielding, estimation of neutron background in accelerator experiments, calculation of efficiency corrections for solid state devices used to measure proton spectra in the energy range 22-40 MeV, estimation of dose rates when neutron beams produced by accelerators

are used in engineering and biological irradiations, and, in fact, in almost all situations in which neutron production by protons in the energy range covered by the experiment is an important consideration.

II. THE EVAPORATION THEORY OF COMPOUND NUCLEUS DECAY

A. Basic Statistical Arguments

In most nuclei the first few lowest excited energy levels are separated from each other, and the ground state, by energies typically on the order of several hundred keV. The independent-particle shell model of the nucleus has met with great success in predicting the detailed properties of these low-lying levels. However, at higher excitation energies, say, greater than 15 MeV, the independent particle model becomes inadequate because the number of levels of closely neighboring energies is too great, particularly in heavy nuclei.

The very concept of the formation of a compound nucleus, which subsequently behaves in ignorance of its mode of formation, implies that the mean free path of a nucleon inside the nucleus is very short; this is not surprising since the nucleon-nucleon force is known to be among the strongest of the known types of interactions between fundamental particles. A consequence of this is that individual nucleons in an excited compound nucleus share their energy in a manner which so far defies detailed analysis (Ev 55), the interaction of a particular nucleon with its neighbors being a highly fluctuating function of time.

When a compound nucleus is formed, the energy of the incident particle is shared by the collective motion of all the nucleons; each nucleon will have some additional energy, but no one particle is likely to have even a sizeable fraction of the incident energy (Mo 53). It may take a long time and many collisions before a sizeable amount of energy can be concentrated upon a single nucleon with the result that

it escapes, cooling the nucleus by "evaporation". The particle which escapes will not in general be the incident particle, and will have neither the direction nor the energy of the incident particle.

A reaction which results in evaporation of more than one particle proceeds by repetition of this process: the first particle is evaporated, and the residual nucleus is another excited compound nucleus which evaporates another particle, and so on, until the remaining excitation energy is insufficient to "boil off" another particle.

With such behavior dominating the picture, the nuclear levels may more profitably be viewed as quantized states of the nucleus as a whole, rather than as configurations of distinguishable nucleons, so that the methods of statistical mechanics and thermodynamics may be applied.

The above qualitative discussion sketches the rationale behind the introduction of the statistical model. It contains several assumptions which will be set forth explicity here, and which should be kept in mind during the development of the model. First, nuclear matter consists of closely packed, strongly interacting particles which interchange energy rapidly with one another. Second, the results obtained from such considerations are meant to apply not to a single well defined state, but to the average properties of many states of closely neighboring energies. Finally, the compound nucleus behaves in a manner which is independent of the details of its formation.

If this last assumption is valid, the cross section of a compound nuclear reaction X(a,b)Y, proceeding as $X + a \rightarrow C^* \rightarrow b + Y^*$ can be written as (Bl 52)

$$\sigma(a,b) = \sigma_c(a)G_c(b) \qquad \text{(II-1)}$$

where $\sigma_c(a)$ is the cross section for the formation of compound nucleus C by particle a striking nucleus X. $G_c(b)$ is the probability that C decays by emission of b, leaving Y as the residual nucleus; it is a pure number.

Equation (II-1) can be rewritten as

$$\sigma(\alpha,\beta) = \sigma_c(\alpha)G_c(\beta) \qquad \text{(II-2)}$$

where α and β denote all the quantum numbers of the reaction partners in the entrance and exit channel, respectively.

Now, $G_c(\beta)$ can be expressed as

$$G_c(\beta) = \frac{\Gamma_\beta}{\Gamma} \qquad \text{(II-3)}$$

where Γ_β is the decay rate of C into channel β, and Γ is the total decay rate of the nucleus, given by

$$\Gamma = \sum_\beta \Gamma_\beta \qquad \text{(II-4)}$$

where sum extends over all channels into which C can decay.

The reciprocity theorem (We 37) relates the cross sections for formation of C via any two channels α and β:

$$\frac{\sigma_c(\alpha)}{\Gamma_\alpha \lambda_\alpha^2} = \frac{\sigma_c(\beta)}{\Gamma_\beta \lambda_\beta^2} \qquad \text{(II-5)}$$

Use of this expression in (II-3) gives

$$G_c(\beta) = \frac{k_\beta^2 \sigma_c(\beta)}{\sum_\gamma k_\gamma^2 \sigma_c(\gamma)} \qquad \text{(II-6)}$$

where as before, the sum extends over all open channels and $k = (\lambda)^{-1}$.

The kinetic energy available to channel β is

$$T = T_{max} - U \qquad \text{(II-7)}$$

where U is the excitation energy of the residual nucleus, and T_{max} is the maximum possible value of T, which will occur if the residual nucleus is left in its ground state (U = 0).

If U is large enough many levels of the residual nucleus may be excited. The measured energy spectrum of the emitted particles becomes continuous when the separation of these levels is less than the overall experimental resolution, or when the levels overlap. The probability that particle b will be emitted with kinetic energy between T and T + dT, $G_b(T)$, is then

$$G_b(T)dT = \sum G_c(\beta)dT \qquad \text{(II-8)}$$

where here the sum extends over all channels β which are open in the energy interval dT about T.

The number of terms in this sum is the number of states in the residual nucleus with excitation energies between U and U-dT, where U and T are related by (II-7). This number is written as $\omega(U)dT$, and the quantity $\omega(U)$ is called the "level density".

Substitution of (II-6) into (II-8) gives the relative intensity

distribution of the emitted particles

$$P(T)dT = \text{const. x } T\sigma_c(\beta)\omega(T_{max}-T)dT \qquad \text{(II-9)}$$

where k_β^2 has been replaced by T. $\omega(T_{max}-T)$ is a rapidly decreasing function of T, that is, a rapidly increasing function of U (Be 38).

To get an idea of the shape of P(T), it is only necessary to consider the quantity

$$S = \ln k\omega(T_{max}-T) \qquad \text{(II-10)}$$

where k is either constant or a very slowly varying function of T (Pr 62). Expanding this quantity in a Taylor series about $U = T_{max}$ gives (We 37)

$$S(T_{max}-T) = S(T_{max})-T\left.\frac{dS}{dU}\right|_{U = T_{max}} +\ldots \qquad \text{(II-11)}$$

If this expansion is used to approximate $\omega(T_{max}-T)$ in (II-9), this gives

$$P(T)dT = \text{const. x } T\sigma_c(T)\exp\left(\frac{-T}{\tau}\right)dT \qquad \text{(II-12)}$$

where the factors due to k and $S(T_{max})$ have been absorbed into the constant and the quantity τ is given by

$$\frac{1}{\tau} = \frac{dS}{dU} \qquad \text{(II-13)}$$

τ has the dimension of an energy and can be interpreted as a nuclear "temperature" inasmuch as $S = \ln k\omega(U)$ can be considered as the entropy of the residual nucleus. Then (II-13) is simply the well known thermodynamic relation between temperature and entropy.

For neutrons $\sigma_c(T)$ is a slowly varying function of T, except at very low energies (Bl 52) so that the product $T\exp(-T/\tau)$ principally determines the behavior of P(T). The energy distribution P(T) is the "Maxwellian" emission spectrum of molecules evaporated from a surface of temperature τ. It has a maximum at $T = \tau$, which should be small with respect to T_{max} if approximation II-11 is to be valid. τ should be interpreted as the temperature of the residual nucleus after emission of a particle, not as the temperature of the compound nucleus before emission.

Thus the shape of the spectrum is given by equation II-12 provided the relation between T and τ (or U and τ, see II-7) is known. This relation depends upon the adoption of a particular nuclear model, which is described in the next section.

B. The Fermi Gas Model Of The Nucleus

The internal energy of almost every system is an increasing function of temperature, and, if the temperature is low, can be written as a power series

$$U = c_0 + c_1\tau + c_2\tau^2 + \ldots. \qquad \text{(II-14)}$$

At high temperatures, equipartition is reached and $U \propto \tau$, but the third law of thermodynamics (Nernst Heat Theorem) requires the heat capacity of any system to vanish at $\tau = 0$ (Ze 43) so that the above series must start, for low temperature, with at least the quadratic term. The coefficients of the various terms depend upon the particular model chosen for the system.

For excitation energies below roughly 50 MeV, a nucleus of mass number A may be considered a degenerate gas of A nucleons confined within a radius R (Mo 53). The internal energy of such a gas is given, to second order in τ, by (Fe 50, Ki 58, Bo 69)

$$U = \frac{3}{5} AE_f + \frac{3\pi^2}{8} \frac{A}{E_f} \tau^2 \qquad \text{(II-15)}$$

where E_f is the energy of the highest filled level at $\tau = 0$, and is given by (Fe 50)

$$E_f = \frac{\hbar^2}{2M} (3\pi^2 A) \qquad \text{(II-16)}$$

where M is the nucleon mass.

So the internal energy of the nucleon gas, measured from the zero point energy, may be written as

$$U = a\tau^2 \qquad \text{(II-17)}$$

which defines the parameter a, and determines the form of the level density, through (II-7), for this model.

It is important to note that, since τ is a function of the kinetic energy T through II-7, the expression II-12 can be written with T as the only independent variable, provided that the level density parameter a is specified.

III. APPLICATION OF THE STATISTICAL-FERMI-GAS MODEL TO THE PRESENT EXPERIMENTAL PROBLEM

A. The Inelastic Collision Probability And Assumptions Concerning Compound Nucleus Formation

The probability that a particle will undergo an inelastic nuclear collision in traversing a thickness x of material is

$$\frac{I}{I_o} = 1-\exp(-n\sigma x) \qquad \text{(III-1)}$$

where I_o is the incident particle flux, n is the number of nuclei per cm^3, and σ is the total reaction cross section for the reaction.

An approximate expression has been derived for the cross section for compound nucleus formation by a charged particle of energy E (Bl 52)

$$\sigma = \pi(R+\lambda\!\!\!^{-})^2\left(1-\frac{V}{E}\frac{R}{R+\lambda\!\!\!^{-}}\right) \qquad \text{(III-2)}$$

where V is the Coulomb potential at radius $R+\lambda\!\!\!^{-}$. The cross section vanishes when the quantity in brackets becomes negative. This expression is derived basically from the assumption that a nucleus of mass number A has a well defined spherical surface of radius R given by

$$R = r_o A^{1/3} \qquad \text{(III-3)}$$

where r_o is the nuclear radius parameter. The quantity $\lambda\!\!\!^{-}$ appears since the position of the incident particle is undefined within that length; for 40 MeV protons $\lambda\!\!\!^{-}\simeq.6$f.

(III-2) is based upon very simple semiclassical arguments and might

be expected to give only order of magnitude estimates, but it agrees quite well, for the range of incident energies covered by this experiment, with the reaction cross sections given by Janni (Ja 66); Janni's cross sections are compilations of experimental data for energies below 40 MeV, and are taken from Monte Carlo calculations (Be 63) for higher energies. It should be noted that the value of σ and therefore of I/I_o is strongly dependent upon the value of r_o used, because of III-3.

Use of (III-2) in (III-1) is based upon the assumption that every incident particle which strikes the surface of a target nucleus forms a compound system, that is, all the flux lost from the incident beam goes to form compound nuclei. Because direct reactions do occur at the bombarding energies used in the experiment, this assumption is not strictly valid, but detailed discussion of this point awaits comparison of its consequences with the experimental data.

B. Procedure Used In Calculating Absolute Thick Target Neutron Spectra And Yields

The problem is to calculate absolutely the number of neutrons produced when a thick (stopping) target of nuclei of charge Z and mass A is bombarded by protons of initial energy E_1. It may be divided into two parts: formation of compound nuclei, and their subsequent decay.

A given target of thickness t is divided into, say, n equal slices. Then the energy loss of the protons in the first slice, ΔE_1, is calculated using formulae referenced by Williamson *et al.* (Wi 62), so that the average bombarding energy for the first slice is given by

$$E_1' = E_1 - \tfrac{1}{2}\Delta E_1 \qquad \text{(III-4)}$$

Then the inelastic collision probability is calculated using (III-1) with x = t/n, and employing the assumption that all flux loss goes to form compound nuclei, as discussed in the previous section. Unit incident flux is assumed, so that the final result will be in units of neutrons/proton.

The excitation energy available in the initial compound nucleus is given by

$$U_A = \frac{A}{A+1} E_1' + M_p + M(Z,A) - M(Z+1,A+1) \qquad \text{(III-5)}$$

where M_p is the proton mass, M(Z,A) is the mass of the target nucleus, and M(Z+1,A+1) is the mass of the compound nucleus; the mass differences are calculated using the mass excesses calculated by Garvey et al. (Ga 69). III-5 is based upon the assumption that all the energy of the incident particle is given to the compound nucleus; for the beam energies used, the results of this experiment indicate to what extent this assumption is valid. For very high incident energies (>100 MeV) it cannot be true (Le 52).

The number of neutrons emitted is calculated under the assumption that the compound nucleus emits only neutrons or protons, neglecting competition from heavier particles, and gamma rays. Formation of composites inside a compound nucleus is relatively rare, and, except for deuterons and tritons, the Coulomb barrier strongly inhibits emission. So, if P_n and P_p are respectively the probabilities for neutron and proton emission, then $P_n + P_p = 1$. P_n and P_p can then be calculated if their ratio is known. This ratio is given by (Le 50, Le 52)

$$\frac{P_n}{P_p} = (R_n/R_p)^{1/4} \exp(2(aR_n)^{1/2} - 2(aR_p)^{1/2}) \qquad \text{III-7}$$

where

$$R_n = U_A - S_n, \qquad \text{III-8a}$$

$$R_p = U_A - S_p - 0.7V_c, \qquad \text{III-8b}$$

and

$$U_A = \frac{A}{\varepsilon}\tau^2 \qquad \text{III-8c}$$

The factor $\frac{A}{\varepsilon}$ is the level density parameter a as previously discussed, and ε takes on values typically between 8.5 and 20, depending on the nucleus under consideration. III-7 is an expression for the ratio of the level densities of the two possible residual nuclei which are left with excitation energies R_n and R_p; R_n and R_p are the effective energies available for the emission of neutrons and protons from nucleus A excited to energy U_A, and become U_A for the next evaporation, when the outgoing particle energies are accounted for. S_n and S_p are the neutron and proton separation energies, as calculated from the mass excess tables of Garvey et al.; V_c is the Coulomb barrier, and the factor 0.7 allows for some barrier penetration; τ is the temperature of the residual nucleus.

$$N(U) = 3P_nP_{nn}P_{nnn} + 2(P_nP_{nn}P_{nnp} + P_nP_{np}P_{npn} + P_pP_{pn}P_{pnn}) + P_nP_{np}P_{npp} + P_pP_{pn}P_{pnp} + P_pP_{pp}P_{ppn} \quad \text{(III-9a)}$$

If two neutrons are possible,

$$N(U) = 2P_nP_{nn} + P_nP_{np} + P_pP_{pn} \quad \text{(III-9b)}$$

If only one neutron is possible,

$$N(U) = P_n \quad \text{(III-9c)}$$

$P_{ijk}(U)$ is the probability that particle k is emitted from a compound nucleus following emission of i in the first stage and j in the second when the initial excitation energy is U.

If the probability for proton emission is less than .05 at any stage, it is neglected, and that stage is considered to decay totally by neutron emission. From III-7 it is easy to see that the Coulomb barrier strongly inhibits proton emission. Apart from this effect of the barrier, the evaporation sequence is governed largely by the separation energies with the consequence that it tends roughly to follow the valley of stability, or tends toward it. Only for light nuclei, where the barrier is low, and for neutron-deficient nuclei, is the proton emission expected to be important.

The emission of particles is followed until the excitation energy of the residual nucleus is insufficient to permit further neutron or proton emission; the remaining energy is assumed to be lost by gamma-ray decay, and is not considered further. A diagram of a part of the

evaporation chain for which the calculation is performed is presented in Figure 1. It is worth pointing out here that the calculation is complicated by the fact that some nuclei in the chain have the same (Z,A), but their excitation energies depend upon the specific manner in which they are reached. Fortunately this difficulty is surmountable with a limited decay chain (<6 particles emitted), resulting only in inconvenience for the programmer; for longer decay chains the calculation becomes quite cumbersome.

Modifications of the level density due to angular momentum effects (Pr 62) are not included in the calculation since they are thought not to be very important in single-nucleon-induced reactions (Be 63). Likewise, "thermal" expansion of the nuclear radius is neglected, because such an effect has been estimated to be small, on the order of 1% for 48 MeV of excitation (Bo 62), the highest excitation energy possible in this experiment.

If a neutron is emitted at a given stage, the energy spectrum is assumed to have the form

$$P(T)dT = N\ T\ \exp\ \sqrt{2a(T_{MAX}-T)}\ dT \qquad \text{(III-10)}$$

where the normalization factor N is the absolute probability for reaching that stage. In this way, the absolute energy spectrum is constructed for comparison with the experimental data.

The whole process is repeated for successive slices of the target, until the incident proton energy is below 0.7 of the Coulomb barrier. The dependence of results of the calculation upon the number of slices, n, was investigated; the results were independent of n for $n \geq 10$, so ten

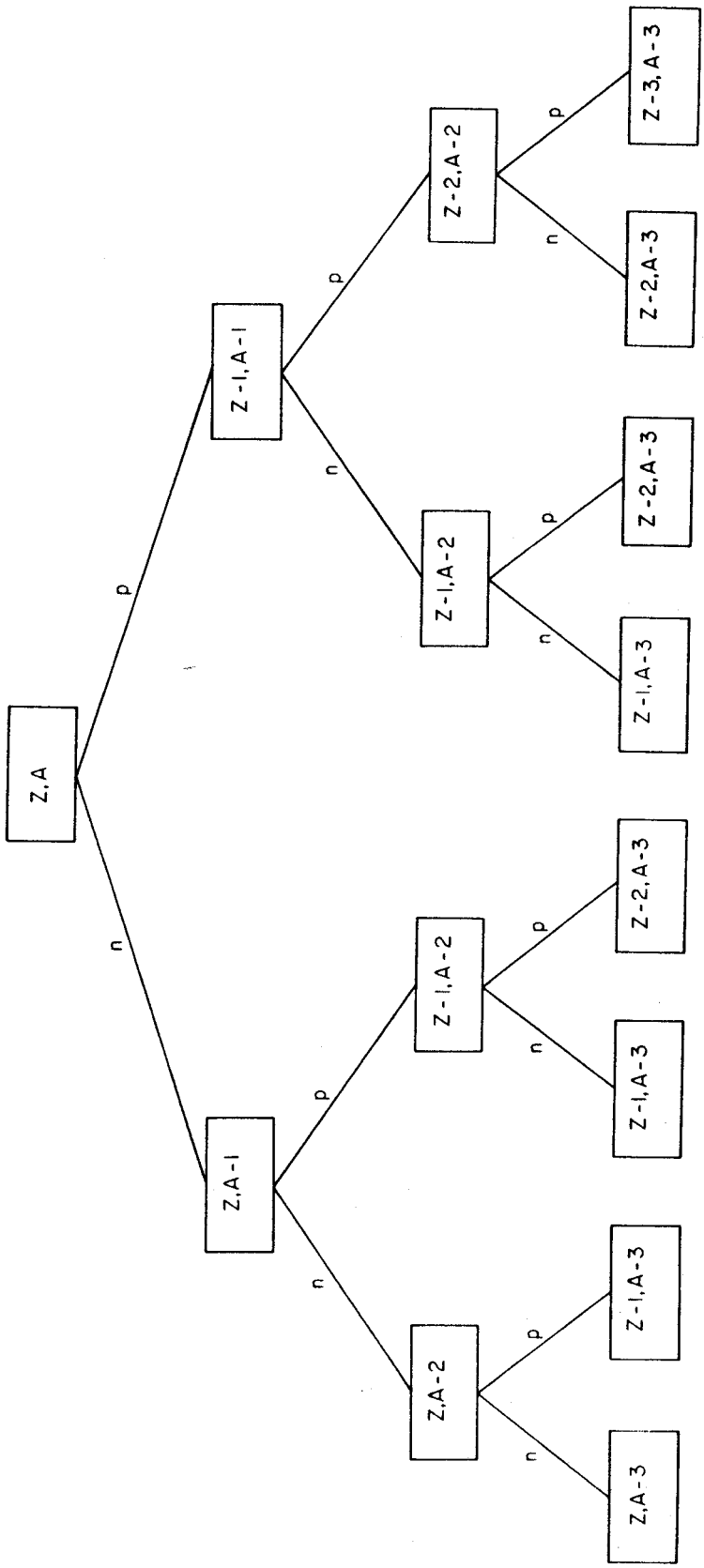

Figure 1. Neutron Evaporation Decay Chain

was the number used in the calculation.

The absolute total neutron yield, and its energy spectrum, are presented at the end of the calculation for comparison with the experimental results. A listing of the computer program DECAY, which calculated the thick target yields is given in the Appendix.

IV. THE EXPERIMENT

A. Measurement Of Neutron Energy Spectra By The Time-Of-Flight Technique

1. General Comments On The Time-Of-Flight Technique

The time-of-flight (TOF) method measures the times taken by neutrons to traverse a known fixed distance, and so determines their velocities; from these velocities, the energies of the neutrons can be calculated. This method is well suited for use with the MSU cyclotron, which produces proton beams of narrow (<0.5 nsec) bursts separated by a much longer constant interval (~50 nsec).

With such a beam, the flight time of a neutron is an interval determined by the occurrence of two signals: one signal occurs at time t when a neutron is detected; the other signal fixes the time at which the burst that produced the neutron was on target. This second signal need not occur at exactly the same instant as the neutron was produced, but may happen at some known time t_o after (or before) the neutron was produced; the main requirement is that this signal be displaced by a constant interval relative to each beam burst.

If prompt gamma rays produced by nuclear reactions in the target are detected at time t_o, this establishes the time at which a given beam burst was on target; gammas are convenient for this purpose since they have the same speed no matter what their energies are. The flight time of a neutron is then given by

$$t_n = L/c + (t-t_o) \qquad \text{(IV-1a)}$$

where c is the speed of light, and L is the distance traversed by both neutrons and gammas, or "flight path"; the quantity L/c is the time interval between the production of a gamma ray or neutron by a beam burst, and the arrival of that gamma ray at the detector.

Both t and t_o are measured relative to a fixed standard "clock" signal, t_c, and time intervals are the experimentally measured quantities; i.e., the second term on the right-hand side (IV-1a) can be rewritten as

$$t-t_o = (t-t_c) - (t_o-t_c) \qquad \text{(IV-1b)}$$

If an isochronous cyclotron produces the incident beam, the t_c signal can be derived from the rf accelerating voltage on the dees.

The relativistic expression for the kinetic energy of a neutron is

$$T_n = M_n c^2(\gamma-1) \qquad \text{(IV-1c)}$$

where $v_n = L/t_n$ and $\gamma = (1-v_n^2/c^2)^{-\frac{1}{2}}$; for low energy neutrons, this reduces to the classical expression

$$T_n = \tfrac{1}{2}M_n L^2/t_n^2 \qquad \text{(IV-1d)}$$

The detector for a neutron TOF system usually consists of a fast-rise-time organic scintillator optically coupled to a fast photo-multiplier (PM) tube; a typical system is shown in exploded view in Figure 2. Although neutrons are detected by means of the charged particle recoils which they induce in the scintillator, it is only important that the detector give a signal which accurately fixes the time at which a recoil occurred; no attempt need be made to relate the recoil energy directly to the energy of the incident neutrons.

An approximate expression which shows the factors contributing to the percentage resolution of a time of flight system can be obtained by taking the derivative of the logarithm of both sides of (IV-1d):

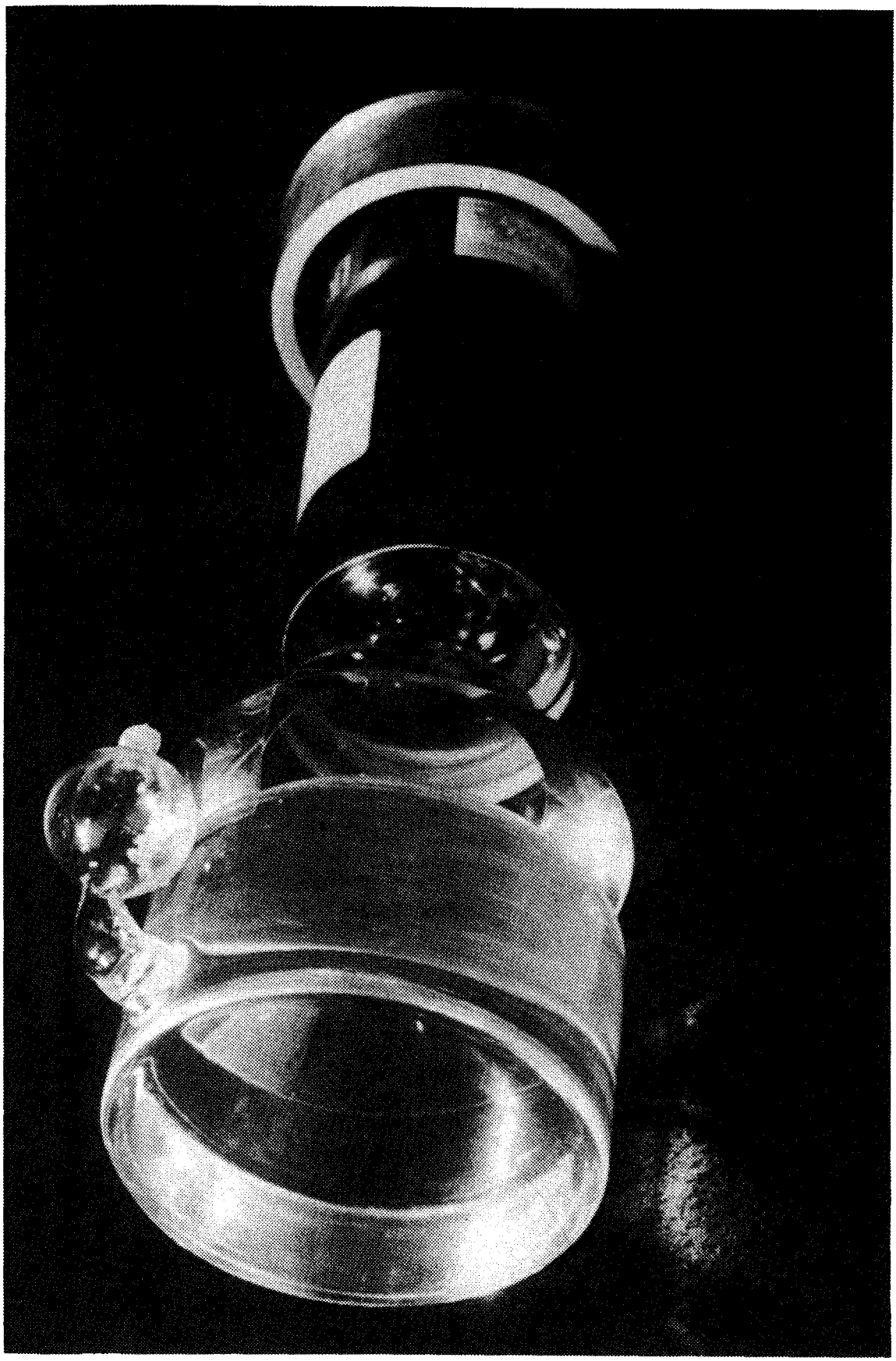

Figure 2. Exploded View of Detector

$$\frac{\Delta T_n}{T_n} = 2\,\frac{\Delta t_n}{t_n} + \frac{2\Delta L}{L} \qquad \text{(IV-2a)}$$

where t_n is the flight time of a neutron of kinetic energy T_n on flight path L; Δt_n is the overall time resolution of the system including contributions from both finite beam pulse width and electronics effects. ΔL is the uncertainty in the flight path due primarily to the finite thickness of the scintillator; it actually makes its contribution to the resolution of the system through the finite transit times of neutrons and photons between the front and rear edges of the scintillator. The contribution to the percentage resolution of the system is given by

$$\frac{2\Delta t_n'}{t_n} = (1-n\beta)\left(\frac{2\Delta L}{L}\right) \qquad \text{(IV-2b)}$$

where $\beta = v_n/c$, and n is the index of refraction of the scintillator; this time difference is clearly less than the second term of (IV-2a) for all $\beta>0$, reflecting the fact that (IV-2a) overestimates the resolution of the system. Adding these contributions in quadrature gives the overall resolution of the system:

$$\frac{\Delta T_n}{T_n} = 2\left[\left(\frac{\Delta t_n}{t_n}\right)^2 + (1-n\beta)^2\left(\frac{\Delta L}{L}\right)^2\right]^{1/2} \qquad \text{(IV-2c)}$$

The first term of (IV-2c) is most important for high energy neutrons, i.e., small t; the second term is most important for low energy neutrons, since their transit time across the scintillator thickness is long, and they may interact at any point along their path. A

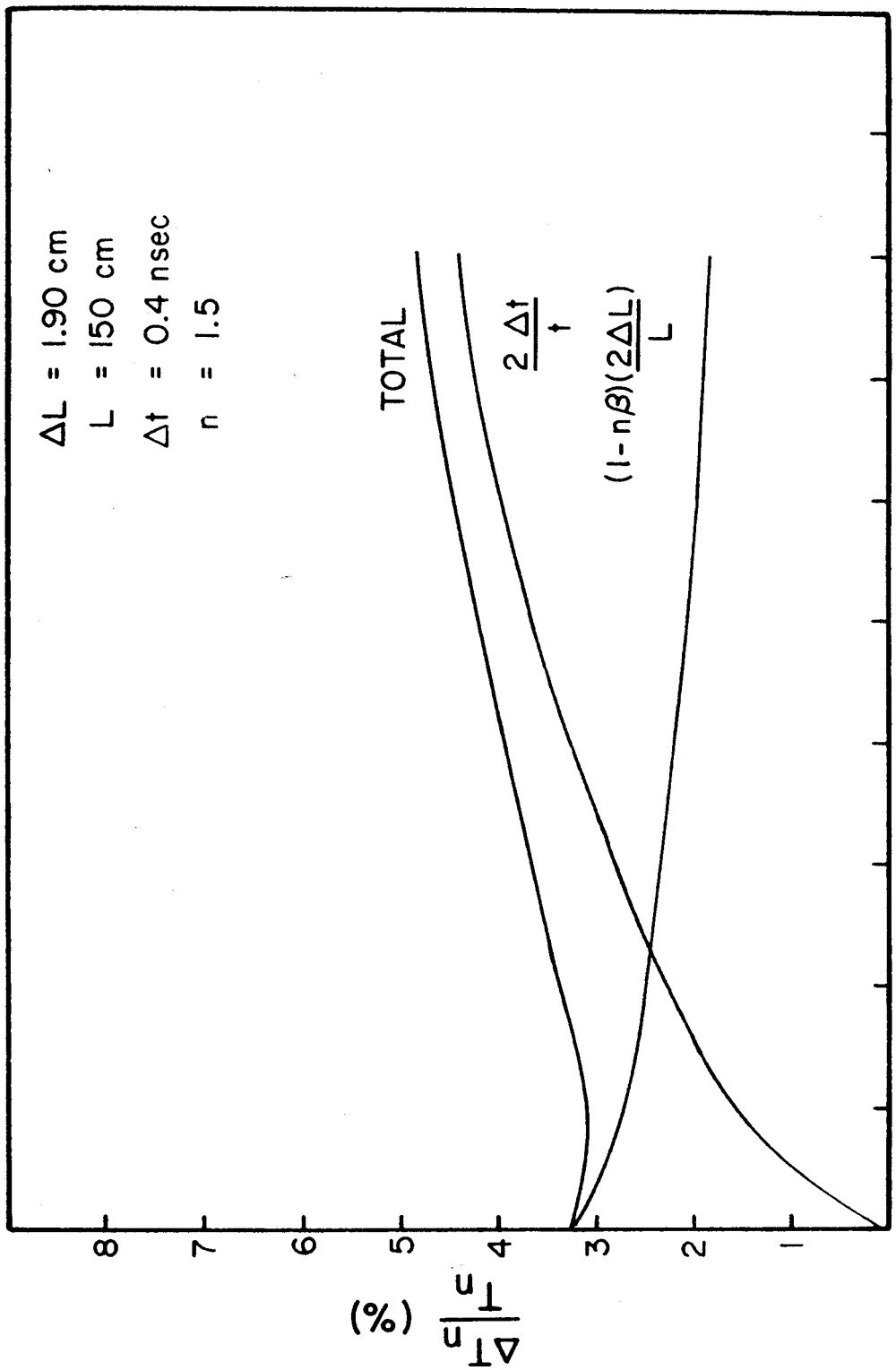

Figure 3. Overall Resolution as a Function of Neutron Energy

graph illustrating this effect is shown in Figure 3.

For a given flight path, the range of neutron energies which can be measured is limited by the pulse repetition rate of the accelerator, since at some point faster neutrons will arrive at the detector at the same time as do slower neutrons produced by the preceeding beam burst. This is called "overlap", and it causes the time spectrum to become confused, because one time then corresponds to two or more energies. For instance, the MSU cyclotron produces a beam of 40 MeV protons, in which bursts are spaced 54 nsec apart. With a flight path of 1.5 meter, flight times of neutrons in the energy range 3.5 -40 MeV may be measured uniquely. If the flight path were shortened to 0.5 meter, the minimum energy detectable without overlap is 0.5 MeV, but the resolution would be worse by a factor of three. The overlap effect is illustrated by Figure 4.

The relative importance of energy range and resolution in a given experiment is determined by the type of information desired and other experimental limitations which will be discussed in the following section.

2. Experimental Design And Procedure

The measurement of neutron yields undertaken in this experiment was intended to include, as far as possible, all neutrons produced, whatever their energies; preliminary theoretical calculations indicated that if the minimum neutron energy measured were 0.5 MeV, the essential features of the energy spectrum would be adequately determined. As noted in the previous section, the repetition rate of the

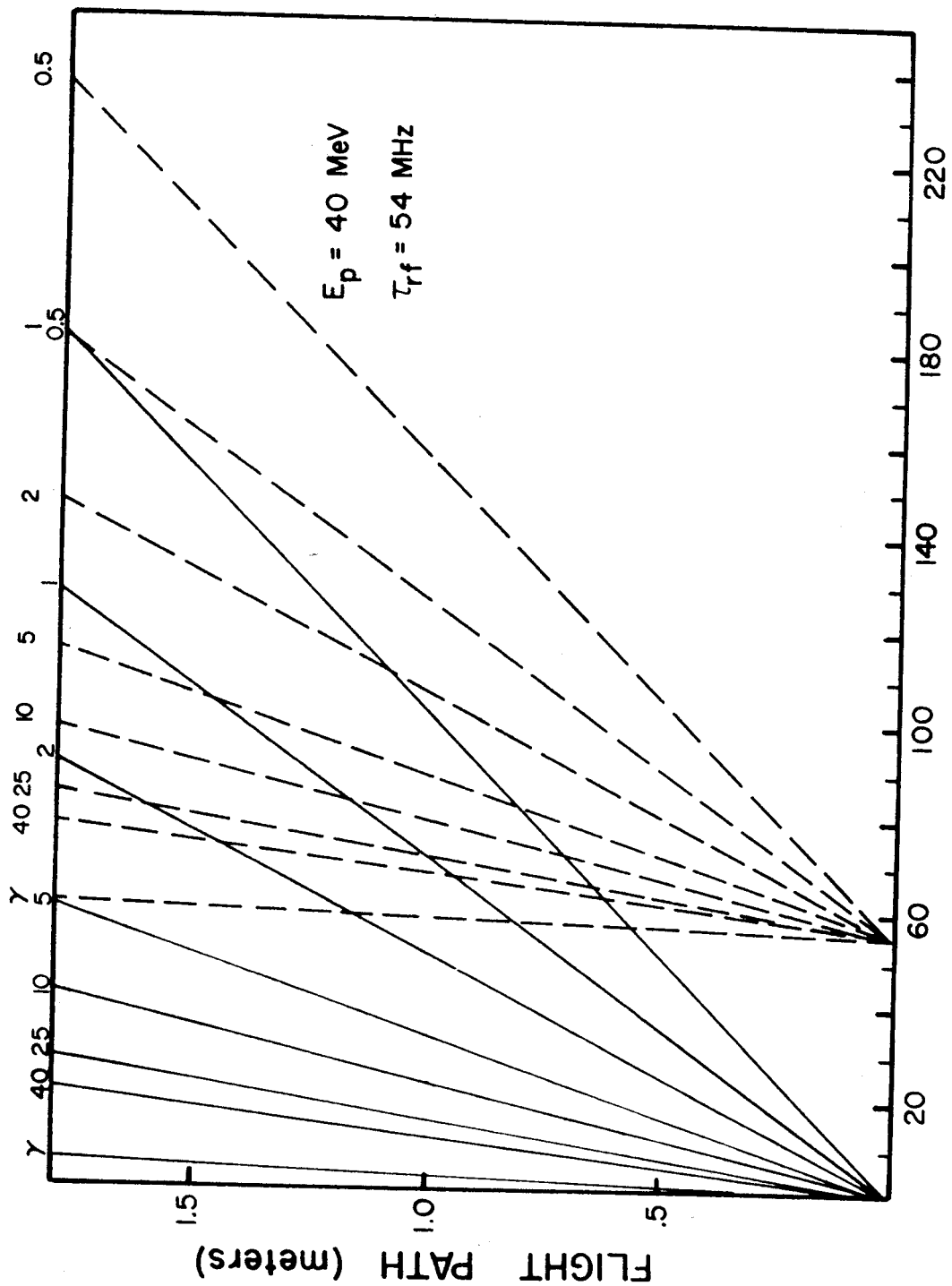

Figure 4. Overlap Effect

accelerator, and the effects of overlap, place a practical limit upon the flight path which can be used, and so effectively determine the energy resolution and range of energies measured.

Another limitation is placed upon the experimental apparatus by the response of the detector to the recoiling protons. The response of plastic scintillator to protons has been investigated for a wide range of energies (Go 60, Ve 68) and found to be highly non-linear over the recoil energy range covered by this experiment. For instance, with the detector and electronics available, 40 MeV neutrons, under typical operating conditions, give output pulses up to 8 volts and 0.5 MeV neutrons give pulses of <0.020 volts. The NIM standard electronics used in the experiment are not able to process pulses over such a wide voltage range, so an energy spectrum could not be measured completely in a single experimental run. Each energy spectrum was measured in two sections which were later joined together to give the complete energy spectrum for neutrons above 0.5 MeV. The detector gain was raised so that the output pulses for 0.5 to 3.5 MeV neutrons were in the optimum operating range of the electronics; the energy spectrum of these neutrons was then measured with a flight path of 0.5 meter to eliminate overlap, with energy resolution of about 8% for 3.5 MeV neutrons. Large pulses due to higher energy neutrons were rejected. For measurement of energies greater than 3.5 MeV, the detector gain was lowered, the flight path was lengthened to 1.5 meter, and pulses due to low energy neutrons were rejected; the TOF spectra were measured with energy resolution of 4.7% for 40 MeV neutrons.

3. The Detector

The detector used in this experiment was a chamber of scintillating liquid mounted on an RCA 8575 PM tube; this PM was chosen for the experiment because it is a high-gain, high-resolution tube whose output is suitable for use with fast timing circuitry.

The scintillator was glass-encapsulated NE213, a liquid plastic; it was chosen because its hydrogen content is high, because its characteristics allow discrimination between neutron- and gamma-ray-initiated events, and because its light output is suitable for fast timing applications. Encapsulation in glass ensures, to the maximum degree possible, that the scintillator cannot become contaminated by any inpurity which might degrade its performance. The glass container was a cylinder with inside dimensions 4.44 cm diameter by 1.90 cm thick; a small chamber was provided by the manufacturer on the curved surface of the cylinder to allow for thermal expansion of the scintillating liquid. The walls and faces of the chamber were 0.16 cm thick.

The scintillator and PM tube were coupled mechanically and optically with Dow-Corning Sylgard encapsulating resin. This rubbery substance provides both mechanical support and excellent optical contact between the surface of the chamber and the outer photocathode surface. Before the resin set, the whole assembly was placed under roughing vacuum to eliminate any bubbles from the region between the scintillator and the PM surface.

After the PM-scintillator combination had been firmly joined, the outside of the scintillator was coated with Eastman-Kodak high reflectance white paint. This paint helps ensure that the light collection

of the detector will be optimized and is superior to aluminum foil in this regard.

When the paint had dried, the whole assembly was wrapped with black electrical tape to prevent leakage of light into the assembly. Such light leakage could create a severe noise problem in the detector, possibly even destroying the PM tube by inducing very heavy currents in the dynode chain.

The detector was then mounted upon an ORTEC Model 271 PM base, which contained, in addition to a resistor bleeder chain specially designed for an RCA 8575, a fast timing discriminator at the anode, and a linear preamplifier at the ninth dynode. The whole phototube-scintillator was then surrounded by a cylindrical shield of Netic, a material of high magnetic permeability, to prevent stray magnetic fields from interfering with PM operation. A diagram of this assembly is shown in Figure 5.

The detector was then mounted on a wooden cart which could be moved on an arc about the target position, so that neutrons from the target always struck normal to the face of the detector. Wooden holders were provided to enable placement of shadow bars between the target and the detector for background measurements. No extra shielding was placed around or about the detector, and nearby material was minimized, to reduce any possible background due to neutron scattering or capture.

The gain of the PM tube was adjusted by altering the high voltage supplied to its dynode resistor chain. When neutron energies between 0.5 and 3.5 MeV were being measured, the high voltage was -1700 volts;

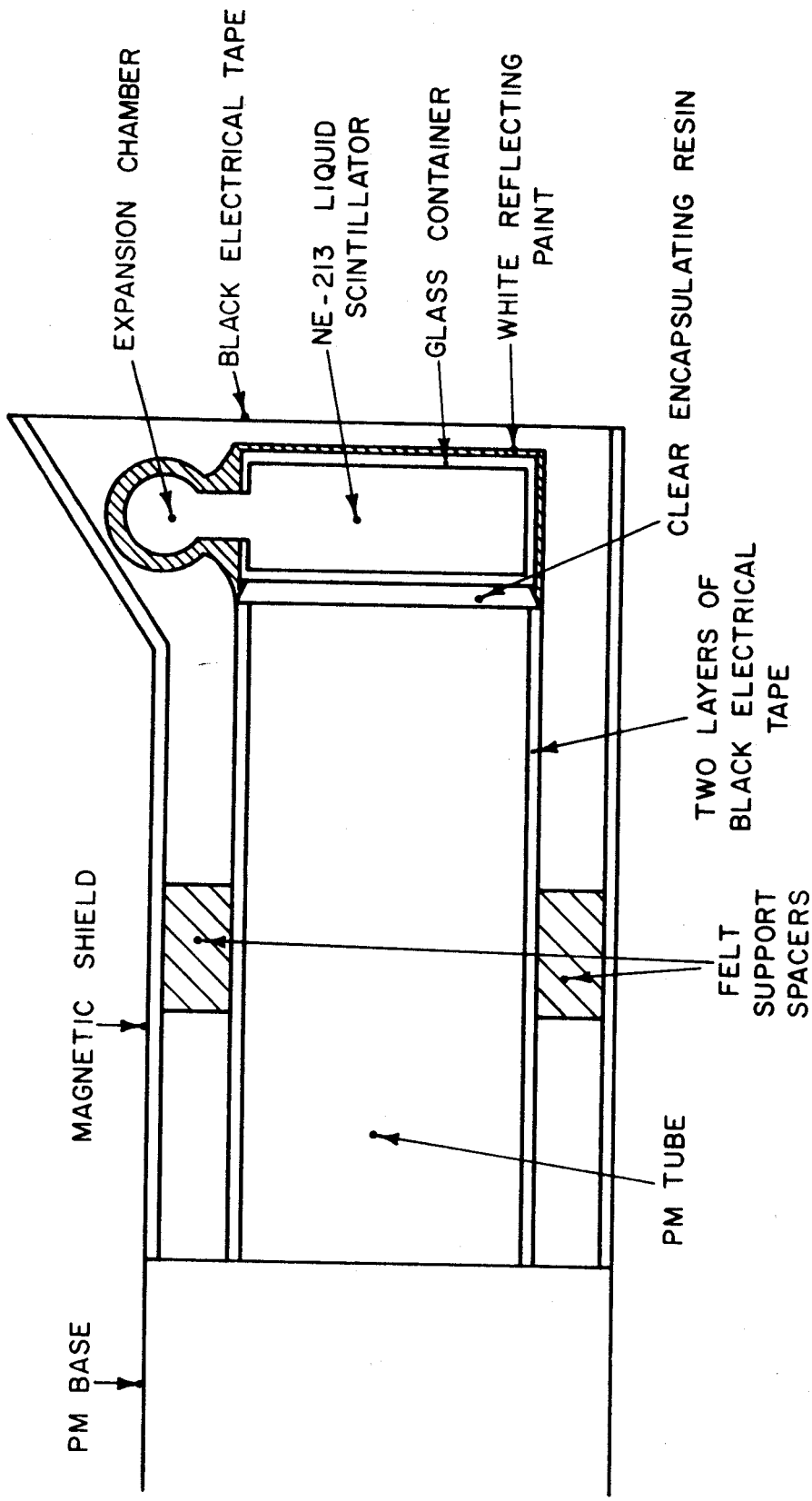

Figure 5. Schematic of Detector

when neutron energies above 3.5 MeV were being measured the high voltage was -1500 volts. These voltages were chosen to place the PM output pulses in the optimum operating range of the rest of the electronics.

4. The Time-Of-Flight Electronics

When a neutron interacts in the scintillator, a light flash may be produced which can cause the ejection of a number of electrons from the photocathode of the PM tube. These electrons cascade down the dynode structure of the PM tube, knocking out more electrons as they go, which join the avalanche. By the time that the anode is reached a sizeable current pulse has built up. If many neutrons interact in the scintillator per second, there will be many such pulses at the anode per second, the height of each pulse being proportional to the light produced in the scintillator by the charged-particle recoils.

The anode pulses were processed by a constant-fraction-of-pulse-height trigger (CFPHT), shown in Figure 6, which generates a fast negative NIM standard logic signal when each pulse reaches a certain fraction of its maximum height (Ge 68); since each anode pulse has the same shape, differing only in height from the others, this significantly reduces the "walk" of the system. Walk is an apparent time difference caused by these different pulses crossing the discriminator threshold at different times, and so generating logic signals at different times relative to the actual arrival of neutrons in the scintillator. Since even a group of monoenergetic neutrons would generate a wide range of pulse heights in the detector, walk can make a large contribution to the experimental resolution; it is essential that this

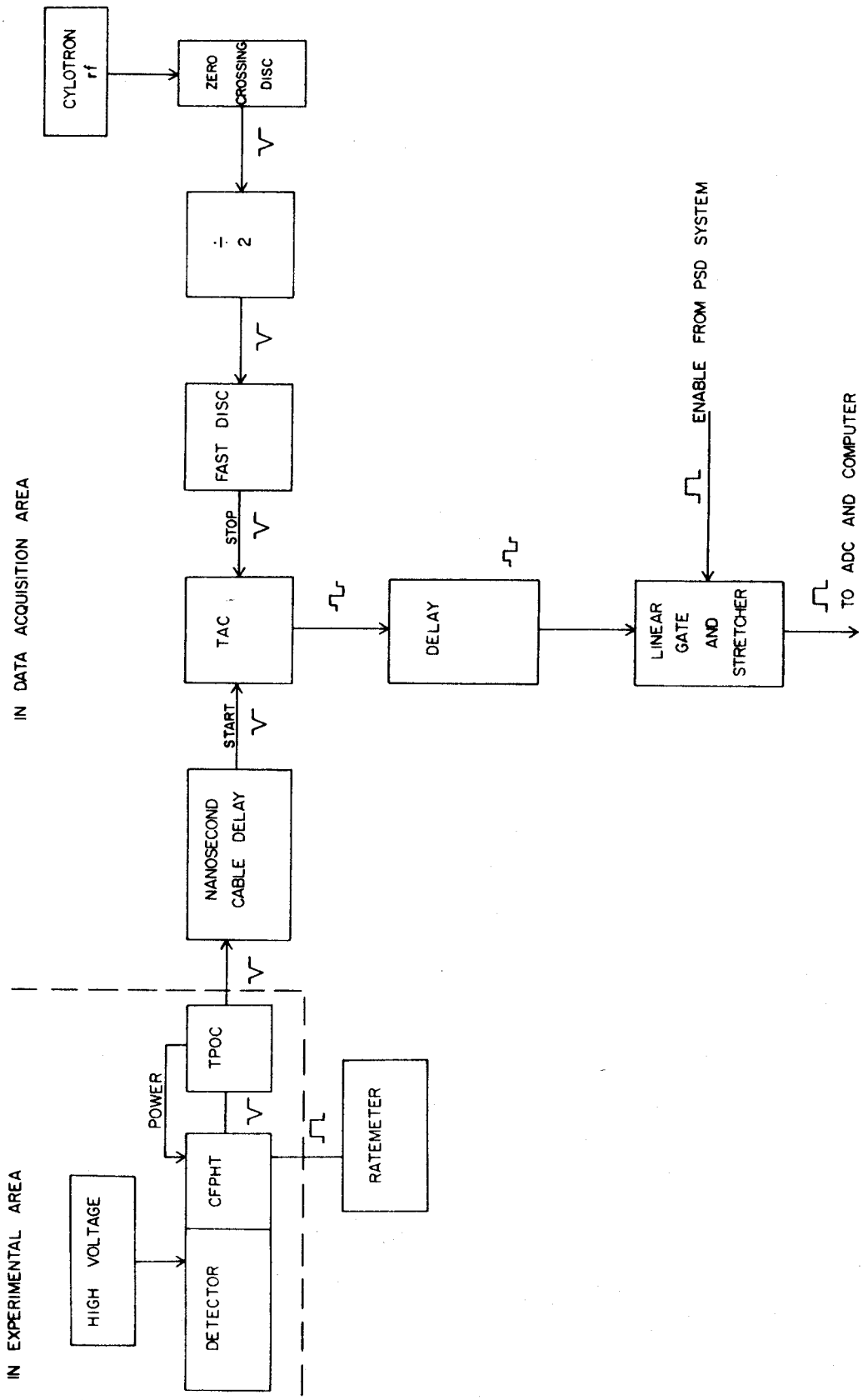

Figure 6. Time-of-Flight Electronics

effect be minimized if a wide range of neutron energies is to be measured at the same time with optimum resolution. The CFPHT is excellent for this purpose; it is located in the PM base to reduce possible cable losses and pickup of electronic noise from nearby equipment. The occurence of the event is marked by the output of the CFPHT.

Power and bias are supplied to the CFPHT by a time-pickoff control (TPOC), which also provides additional logic shaping of the CFPHT output. Since all the pulses generated by lower energy neutrons are small at both PM operating voltages, and the CFPHT involves a zero-crossing discriminator, much care was taken to insure that the discriminator threshold was set above the discriminator noise level, that it was set well below the minimum pulse-height level which governed the rest of the electronics, and that it remained there throughout the course of the experiment. To guard against bias drifts, a ratemeter was used to monitor the count rate of the CFPHT to insure that the bias remained properly set.

The TPOC output signal passed through roughly 40 meters of RG-8 cable to the data acquisition area of the laboratory, through a nanoseconds cable delay, and was finally presented to the "start" input of a time-to-amplitude converter (TAC), an instrument which produces an output signal proportional to the interval between the arrivals of a start and a stop signal.

The TAC stop signal was derived from the cyclotron rf system in the following manner. A probe adjacent to a dee of the accelerator picked up the sinusoidal rf acceleration signal on the dees; this signal was subsequently attenuated and presented to a zero crossing

discriminator, which puts out a fast logic signal each time the input goes through zero, from positive to negative.

This "clock" signal was then fed into a fast scale-of-two, which produces one output signal for every two input signals. Use of this scale-of-two to eliminate every other rf clock pulse causes two separate but identical spectra to be accumulated, and automatically calibrates the TAC; this effect is called "doubling". The output of the scale of two is not quite suitable for use by the TAC, so it was fed into a fast discriminator for logic shaping. The fast logic pulse produced then went into the "stop" input of the TAC, which was used in its linear region of operation (~85% of full scale).

The TOF spectrum produced by the TAC was fed through a linear microsecond delay amplifier to satisfy gating and coincidence requirement and then to a linear gate and pulse stretcher, which fed into an analog-to-digital converter (ADC) interfaced to an on-line digital computer.

5. Pulse Shape Discrimination

a. Application To Neutron Time-Of-Flight

In the measurement of neutron TOF spectra, difficulty may be encountered if a large flux of gamma rays is present. Gamma rays can interact with the scintillator by Compton scattering with the electrons in the scintillator, and if the flux is very high, may cause severe background and count rate problems and degrade the quality of the neutron measurement.

The gamma rays have four principle sources: (1) prompt cascades

following nuclear reactions in the target; (2) proton bremsstrahlung in the target; (3) neutron capture by nuclei in the walls, floor, ceiling, etc. of the experimental area; (4) and induced radioactivity in the target. Gammas from (1) and (2) above are directly correlated in time with the beam bursts which produce them, and in fact fix the time, relative to the rf clock signal, at which a beam burst was on target; however, in certain experimental situations they may mask an important feature of the neutron spectrum. Gammas from (3) and (4) are time-uncorrelated with the beam and will provide a smooth, flat background under the whole TOF spectrum.

Thus, to avoid loss of information and uncertainty due to background subtraction, it is desirable to eliminate the gammas from the neutron spectrum. Unfortunately it is generally not possible to reject gammas by simple pulse height selection since, as in the case of the neutron energies measured in this experiment, pulse heights from neutrons- and gamma-induced recoils may cover almost the same range. Gamma rejection may be accomplished, however, by a method which depends on a difference between the shapes of pulses induced by the two different particles.

b. Basis Of The Pulse Shape Effect

At energies below 100 MeV neutrons react with plastic scintillators via n-p elastic scattering, and by (n,p), (n,α) and (n,n'3α) reactions with carbon; the energy of the recoiling charged particles from these reactions is deposited in the scintillator and some of this energy is eventually converted by molecular de-excitation into a light

flash. Gamma rays, as previously noted, undergo Compton collisions with electrons in the scintillator, which recoil and deposit their energy in the scintillator.

In passing thru the scintillator a recoiling charged particle produces an ionized track whose specific ionization density depends upon the energy, charge, and mass of the particle. The light output per unit energy loss in an organic scintillator is less when the ionization density is high (Go 60), resulting in a non-linear scintillator response as a function of recoil energy (Wr 53, Bi 51). Furthermore, the molecules of the scintillator are excited to different modes of excitation depending upon the specific ionization of the recoil (Ow 58), and their subsequent decay by scintillation has been observed to consist of at least two exponential decays whose relative intensities and time constants also depended upon the incident particle (Sj 65).

With proper care, this dependence of scintillator response upon the conditions of its initial excitation may be exploited to identify the incident particle. This technique is called pulse shape discrimination (PSD). The PSD electronics are described in the next section.

c. Electronics

A number of PSD techniques have been published (Al 61, Da 61, Ro 64), all of which vary widely in resolution, complexity, and acceptable range of pulse heights. This experiment required the ability to distinguish easily between neutron- and gamma-ray-initiated events over a wide range of pulse heights. An adaptation of this technique first proposed by Roush et al. (Ro 64) was chosen as

best fulfilling the requirements of the experiment.

If the current pulse arriving at a given PM dynode (in this case the ninth) is initiated by scintillator light with two principal decay constants, the pulse may be expressed as a function of time as

$$i(t) = A(E)\exp(-at) + B(E)\exp(-bt) \qquad \text{(IV-3)}$$

where A(E) and B(E) depend upon the energy E deposited in the scintillator, and a>b, and all four constants depend upon the exciting particle (i.e., the recoiling particle). If the resulting voltage pulse is differentiated twice, the time at which the resultant crosses zero with respect to the beginning of the original signal depends sensitively on the relative amount of slow component present in the initial pulse (Ro 64).

The time at which a detector pulse began was marked by the output of the CFPHT, which, as shown in Figure 7, fed into the TPOC. A second available fast logic output of the TPOC (the other was used for the TOF signal) was then amplified by a fast logic amplifier and fed through 152 meters (500') of RG-8 cable. Amplification was necessary since the TPOC pulses were severely attenuated by cable losses; RG-8 cable was employed to minimize such losses. After a second amplification and another 152 m length of RG-8, followed by a switch-selectable nanosecond cable delay, the pulses were fed into the stop input of a TAC.

The linear pulse height signal from the ninth dynode of the PM was amplified by a linear pre-amplifier and sent to a double-delay-line amplifier (DDL), where it was double-delay-line differentiated in order to extract the pulse shape information as described at the

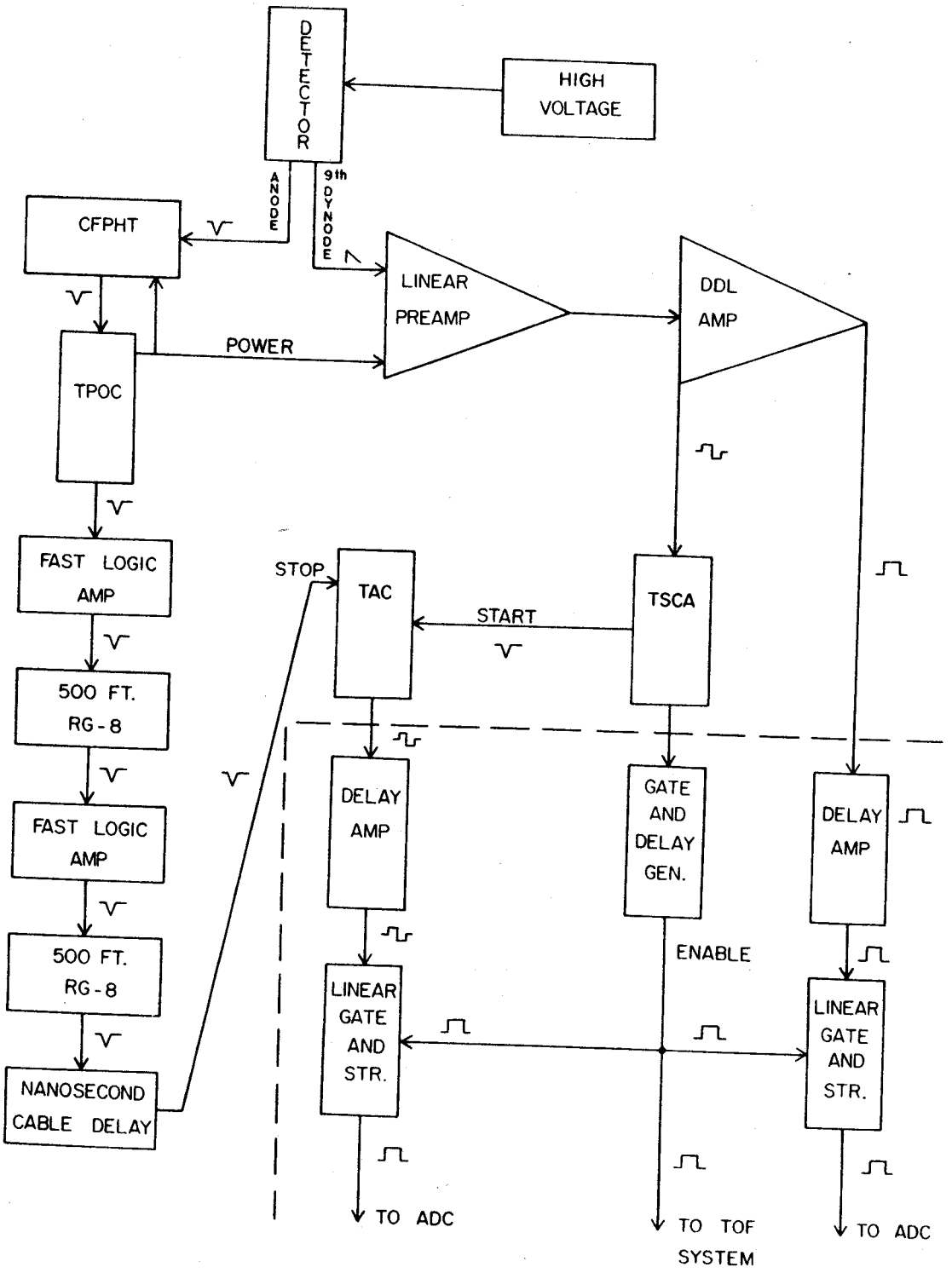

Figure 7. Pulse Shape Discrimination Electronics

beginning of this section. Double delay line differentiation was employed because it does not cause baseline shift problems to the extent that double RC differentiation might, and because the resultant output pulse crosses through zero faster than in the case of double RC differentiation (Mi 65).

The DDL has two outputs, bipolar and unipolar. The unipolar output was sent directly to the data acquisition area where it was fed into a delay amplifier, to satisfy gating and coincidence requirements, and then into a linear gate and pulse stretcher. The bipolar pulse, which was used to extract the pulse shape information was fed into a timing single-channel analyzer (TSCA).

If a pulse fell within a range determined by two discriminators, the TSCA put out two pulses: a positive, slow logic signal which indicated that the pulse was within the range, and a fast negative logic signal which marked the time at which the bipolar signal crossed zero. The positive logic pulse was sent to the data acquisition room, where it was used to enable the linear gates; thus the TSCA discriminator levels determined which signals would be presented to the ADCs.

The negative pulse from the TSCA was fed into the start input of the TAC. This pulse was used as a start, and the CFPHT signal was delayed about 2 microseconds because the CFPHT, as noted previously, was set below the TSCA lower level and so had a higher count rate; the dead time of a TAC is significantly reduced if the start rate is lower than the stop rate.

Separate DDL-TSCA combinations were used for the measurement of low-energy and high-energy neutron spectra. The gains of the DDL's

were different, and each combination was calibrated with a series of gamma-ray sources as described in section IV.F.2b.

The TAC output was fed into a delay amplifier, then into a linear gate stretcher whence it was fed into an ADC. The TAC output pulses consist mainly of two groups: one corresponding to the zero-crossing time of the neutron pulses, the other corresponding to the gammas. Such a TAC spectrum is shown in Figure 8. The separation of the two groups, apart from the detector response to neutrons, is influenced by the walk of both the CFPHT and the TSCA; the walk of the TSCA dominates, particularly at low pulse heights, and for small pulses the groups tend to merge. The ability of the electronics to discriminate between neutron and gamma-ray induced pulses may suffer as a result (Ro 64).

This effect may be largely eliminated by a two-parameter analysis of the linear pulse height (PH) and TAC (PSD) signals, using either a two-dimensional multi-channel pulse-height analyzer or dual ADCs interfaced to an on-line digital computer; a computer-ADC combination was used in this experiment because it provided greater flexibility (the details of the computer software and data acquisition will be discussed in a later section). If the two signals are plotted versus each other and displayed on a storage oscilloscope, a display such as Figure 9 will be obtained. Figure 10 is a three-dimensional plot of a similar display; note the large number of gammas at small pulse heights which may contribute, through TSCA walk, to γ background in the neutron TOF spectrum. The PSD signal is displayed along the vertical axis, the PH signal, along the horizontal axis. The upper group corresponds to γ-events, the lower group, to neutron events.

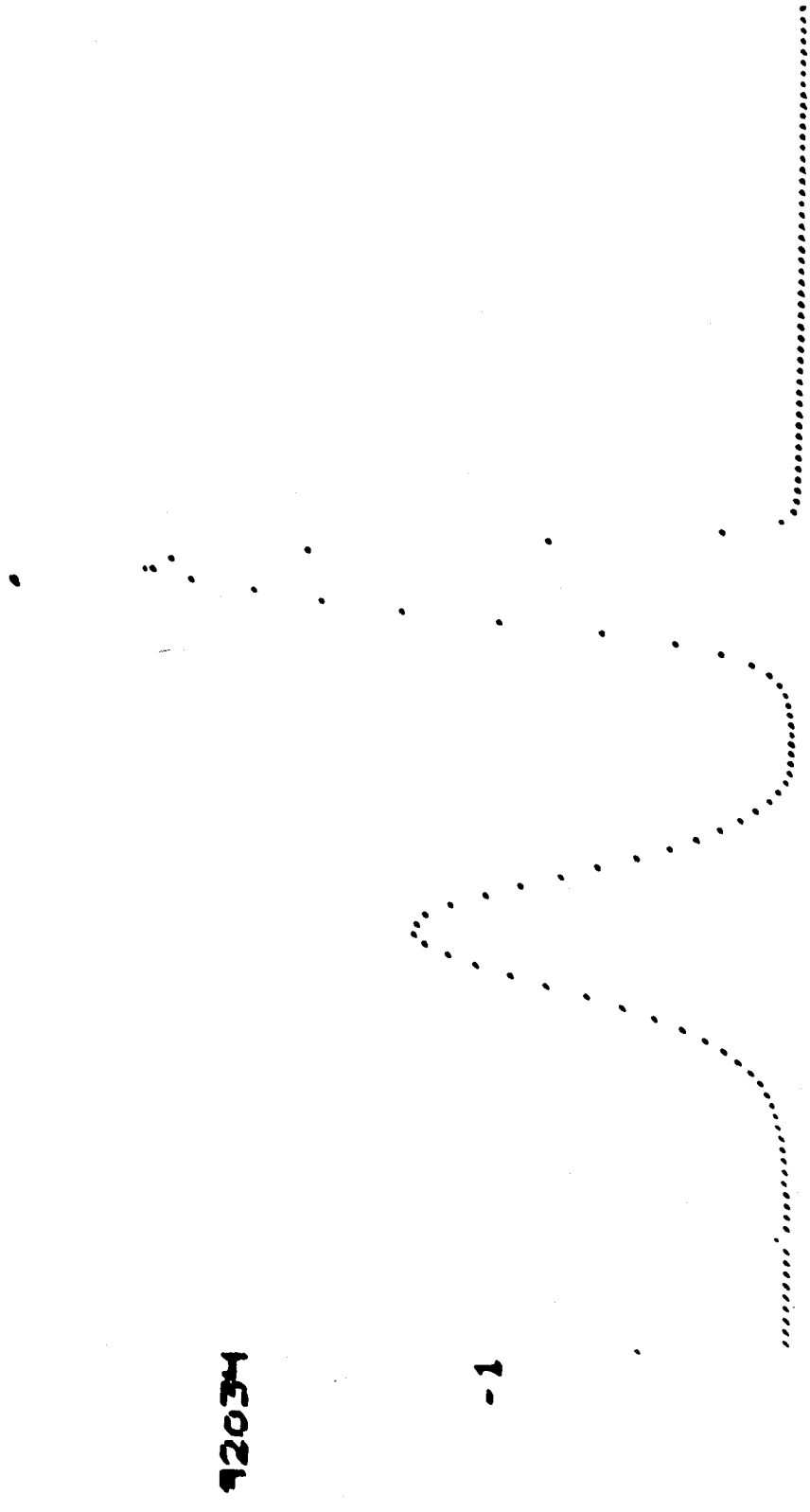

Figure 8. Pulse Shape Discriminator Cross-Over Time Spectrum

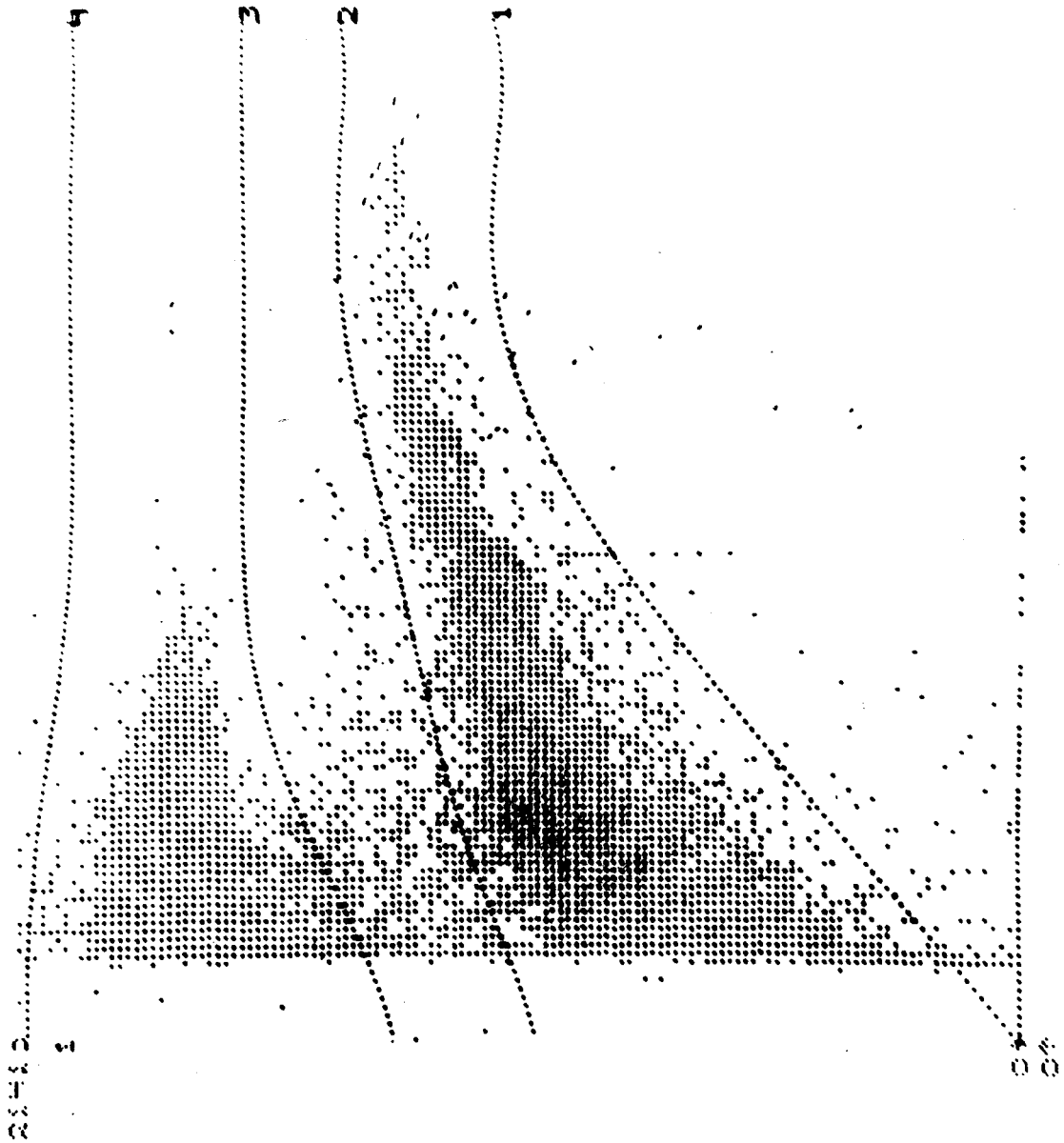

Figure 9. Two-Dimensional Pulse Shape Discrimination Display

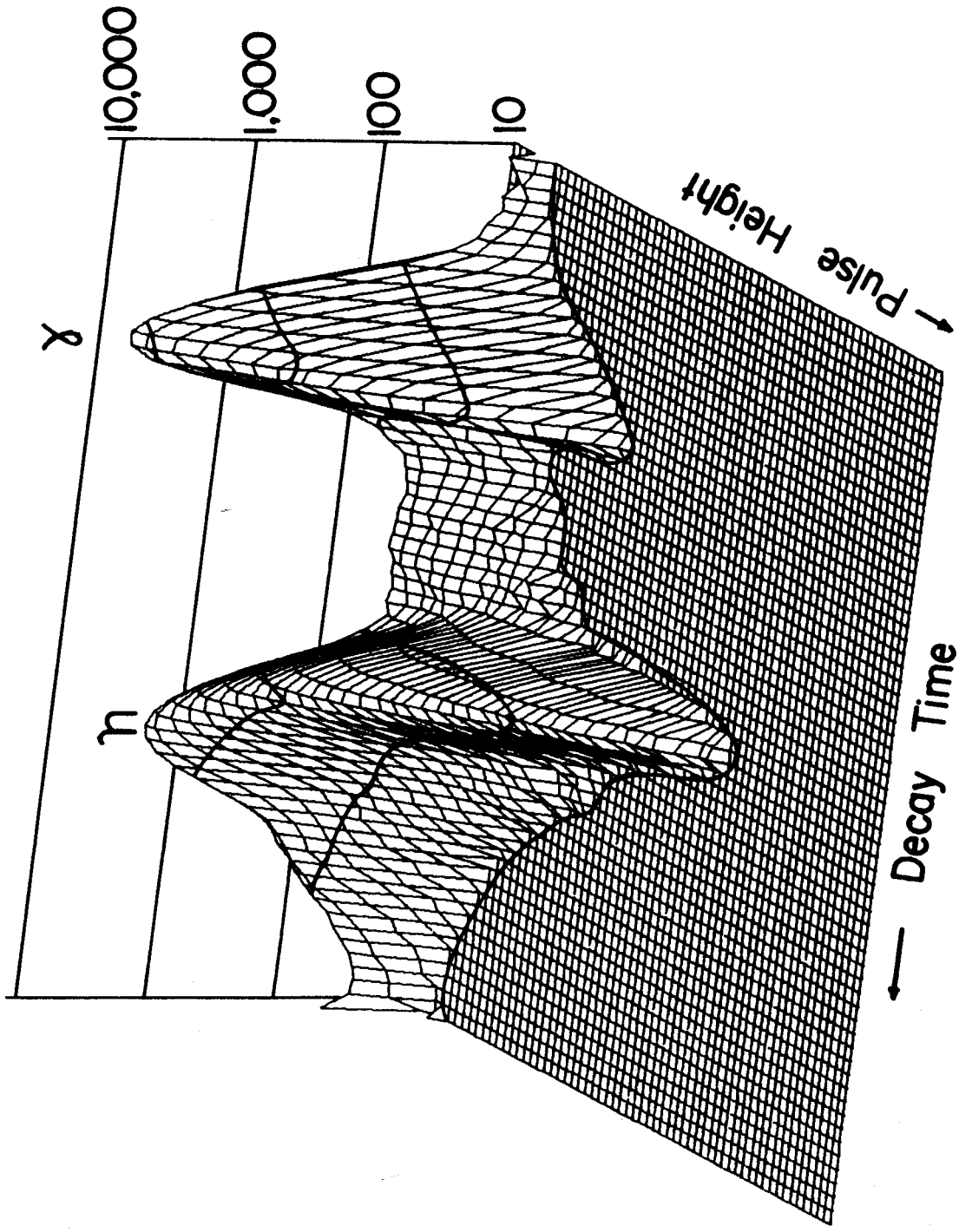

Figure 10. Three-Dimensional Pulse Shape Discrimination Display

The "bands" shown in Figure 9 are digital gates which set limits for determining which events will be accepted by the computer for further on-line analysis; they are determined empirically at experimental run time. Events which fall outside the bands are not considered further; these rejected events were an insignificant fraction of total number of events. Events which fall inside the bands may be used in two principal ways: (1) they may be accumulated as separate neutron and gamma-ray pulse height spectra; (2) they may be used to determine whether a given TOF pulse should be stored in a γ-TOF spectrum or a neutron TOF spectrum. Option (2) was taken for this experiment.

A figure of merit for the PSD system used in this work, the gamma-rejection ratio, is given by

$$R = \frac{\#\gamma\text{'s in a peak in } \gamma \text{ TOF spectrum}}{\#\gamma\text{'s at same point in n TOF spectrum}} \qquad \text{(IV-4)}$$

Gamma-rejection ratios typically on the order of 200:1 were easily achieved in most experimental situations, as illustrated by Figure 11, which shows typical TOF spectra for both neutrons and gammas.

B. Beam Line

The MSU Cyclotron was used to provide beams of protons at energies of 22, 30, and 40 MeV. The details of the beam transport system have been discussed in reference Ma 67. The beams were defined spatially by slits 1, 3, and 4, shown in Figure 12. After being focussed at slit 3 by quadrupole magnets Q1 and Q2, (Q3 and Q4 were turned off except at 40 MeV where a little additional strength was required to

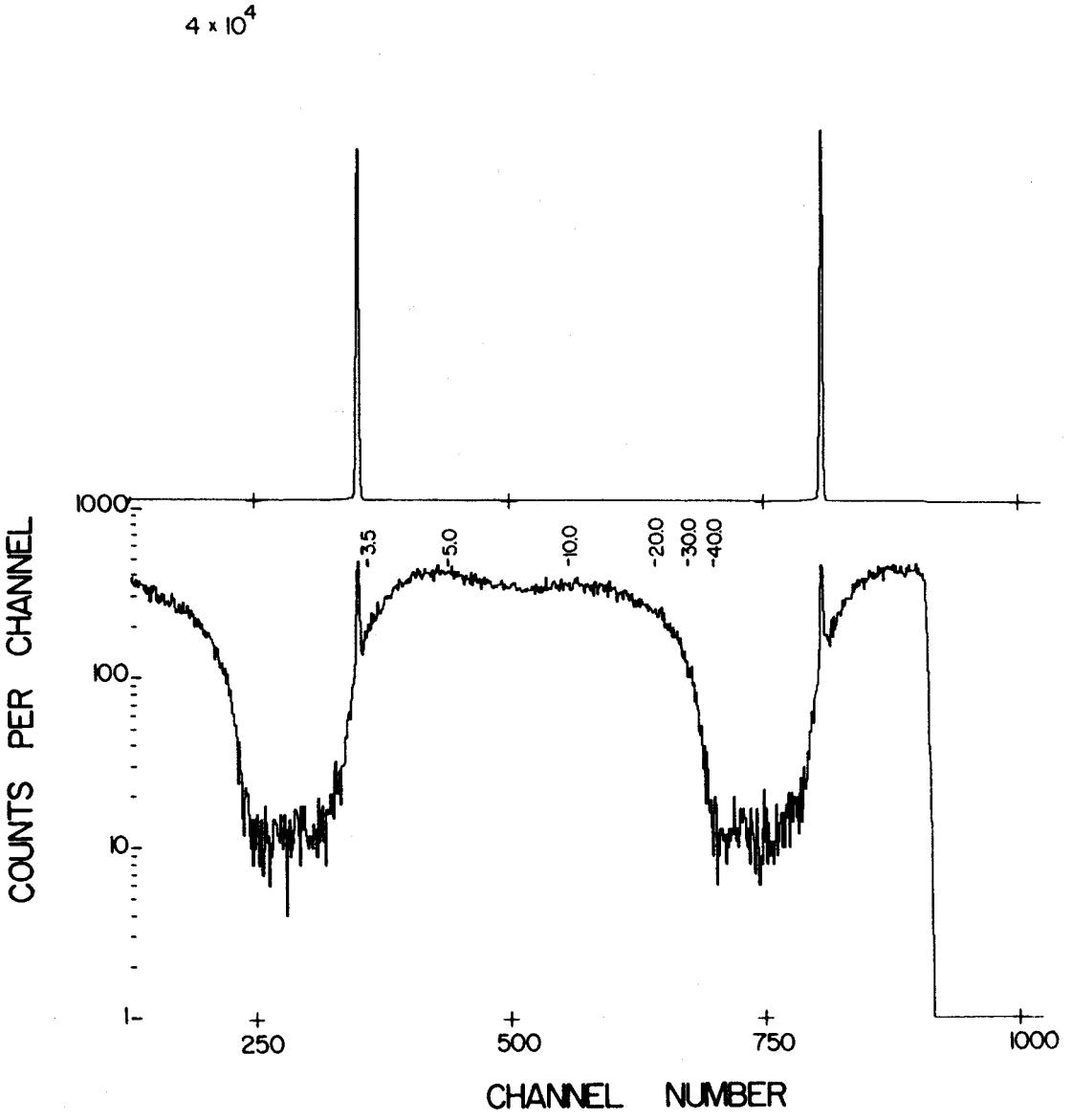

Figure 11. Time-of-Flight Spectrum Measured with Pulse Shape Discrimination

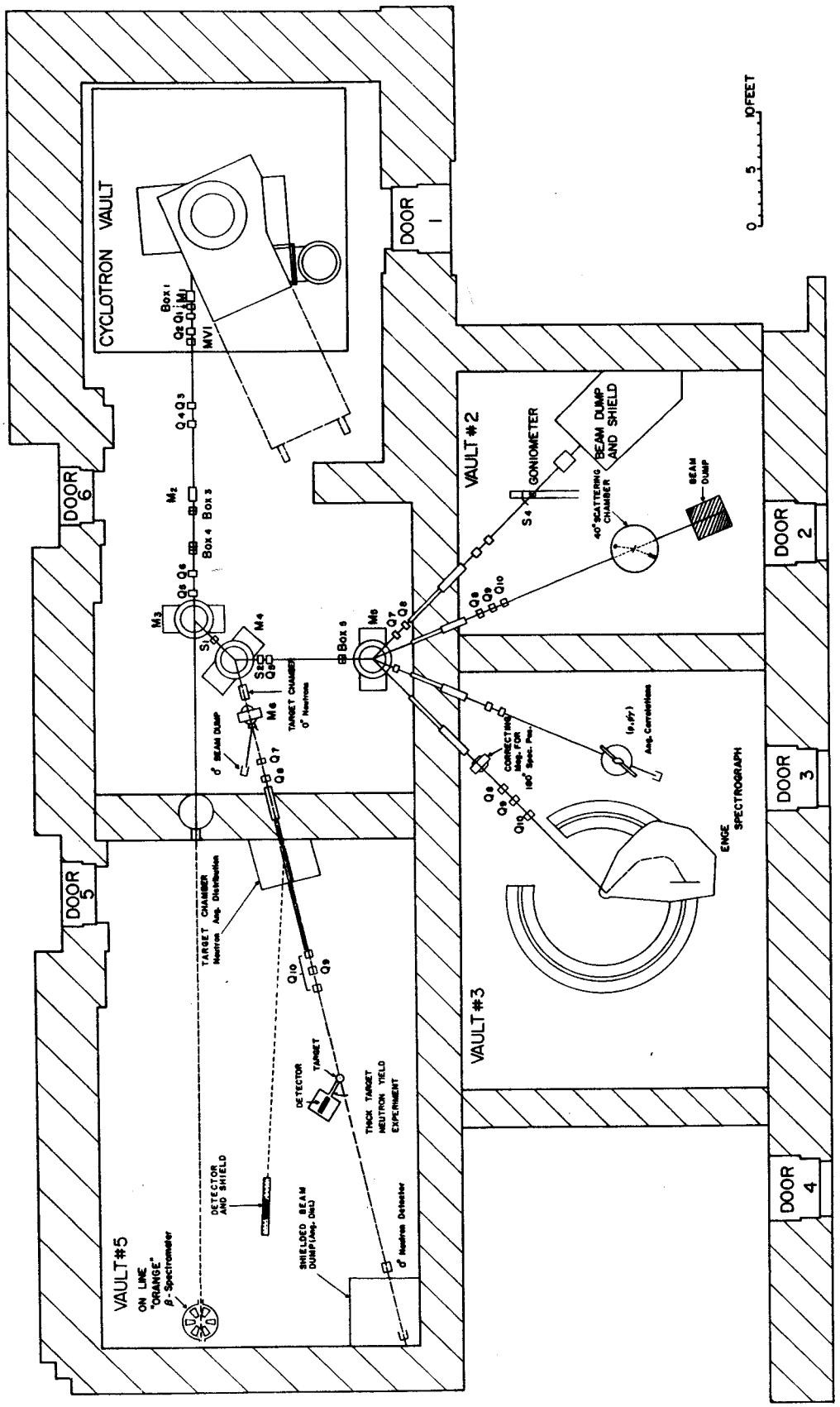

Figure 12. Beam Line Layout

focus the beam), the beam passed through slit 4 and was bent through +45° by steering magnet M3, then bent through -31.5° by magnet M4 into the neutron TOF beam line. After going through an intermediate focus produced by Q7 and Q8, the beam was focussed on target by quadrupole triplet Q9-Q10.

No energy analysis was performed upon the beam; experience with the cyclotron beam has shown that the energy resolution of the unanalyzed beam is ~0.1%, or 40 keV at 40 MeV. Slits 1, 3, and 4, in conjunction with the ion source of the cyclotron, were used principally to limit the beam current so that the count rate in the detector was kept at an acceptable level.

The magnetic field strengths of all magnets were calculated for the beam energies used; fine adjustments were made empirically, based on remote visual observation of the beam spot on remotely controlled quartz and plastic scintillators in the beam line. Particular attention was devoted to the size and placement of the beam spot at the target position.

C. Targets and Target Chamber

The targets used at a given energy in the experiment were discs 2.54 cm in diameter, with thickness equal to the range plus range straggling of the incident protons, as given by range-energy tables (Ja 66). The only exceptions were for carbon at 22 and 30 MeV, where targets made for 30 and 35 MeV respectively, were used; this should in no way affect the experimental results, or conclusions drawn from them.

The targets were fabricated from natural C, Al, Cu, Ag, Ta, and Pb. These elements were chosen because they span a wide range of nuclear masses. The target discs were press-fitted into thin rectangular aluminum frames 5.08 cm wide by .16 cm thick by 2.86 cm high, for mounting on a target ladder; the frames were made as thin as possible to minimize any extraneous material around the targets. The target ladder was long enough to mount 6 targets plus a 2.54 cm by 2.54 cm Pilot B scintillator.

A diagram of the target chamber assembly is shown in Figure 13. The chamber walls were .32 cm thick, and the entrance to the chamber was through a narrow opening 3.6 cm in diameter and 11 cm long to minimize the possibility of incorrect charge collection due to escape of electrons from the chamber.

A 2.54 cm viewport was drilled into the side of the chamber to allow for visual observation of target height, target angle, and beam spot size and location on the scintillator; to provide vacuum integrity of the chamber, a piece of mylar .0125 cm thick by 25 cm^2 was fastened over the viewport with epoxy resin. To allow convenient illumination of the chamber interior, a clear lucite blanking port was used to blank off the lower end of the chamber.

Target position and target angle were changed by a drive unit mounted at the top of the chamber; the drive unit was actuated remotely from a control panel in the data room.

The targets and target holder were isolated electrically from the drive unit by a DELRIN insulator, and electrically connected to the chamber walls by a long flexible spring. The chamber itself was

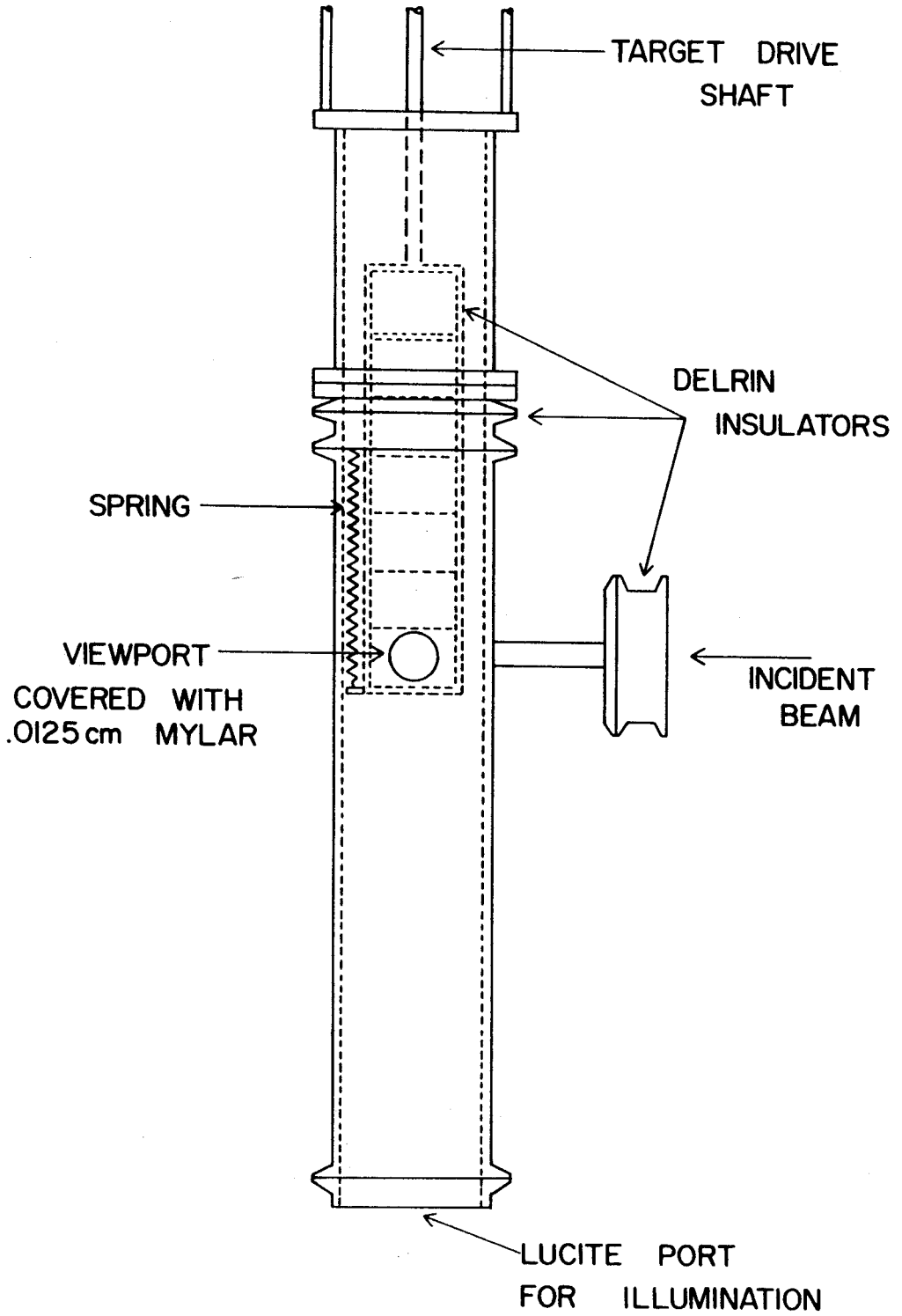

Figure 13. Target Chamber Assembly

insulated from both the drive unit and adjoining beam pipe by DELRIN insulators. Thus, the targets and target chamber performed as a Faraday cup for charge collection purposes.

D. Charge Collection and Integration

The beam incident upon the targets was collected and integrated by an Elcor Model A310B Current Indicator and Integrator. This current integrator has been calibrated using an internal source and external sources and found to be accurate to within 1% for each current scale (Ku 67). Before each experimental run, the integrator was checked with its internal source, and with a precision battery and resistor, and found to be consistent with the previous measurements.

The performance of the CFPHT and TSCA, as noted previously, were sensitive to count rate; in particular the TOF and PSD resolution were observed to deteriorate at CFPHT count rates above 10 kHz. This placed a practical limit on the incident beam intensity.

For the measurement of 0.5-3.5 MeV neutrons, where the yields were largest, the beam had to be limited to currents on the order of 10^{-10}, 10^{-9}, and 10^{-8} amp for 40, 30, and 22 MeV, respectively. For these low scales, particularly at 40 MeV, the current integrator was observed to be not very accurate at low currents and was sometimes observed, between runs, to be integrating spurious positive and negative currents; this effect was not observed to be greater than about 10%, and did not always occur. Corrections made for this effect will be discussed in the section on data reduction.

E. Data Acquisition

Data were taken under the computer code TOOTSIE (Ba 71), operated in its LIGHT mode. In this mode the PSD and pulse-height signals from the electronics are initially displayed on a Tektronix 611 storage scope as a 128 channel by 128 channel two-dimensional plot, with x-axis = pulse height, y-axis = PSD signal. The data and display may be manipulated by both teletype commands and switch actuated signals.

Digital gates, called "bands", were drawn around the groups of signals corresponding to gamma-rays and neutrons. Then the data-taking mode of the program was initiated; in this mode the TOF signals were stored in either one of two 1024 channel spectra depending upon whether the corresponding PSD-pulse height signals fell within one digital gate or the other. Thus separate neutron and gamma TOF spectra, as shown in Figure 11, were accumulated; events falling outside the bands were rejected, and, in this mode of operation, none of the two-dimensional data were stored.

The data were output from the computer on punched cards and as 1024 channel histogram plots.

F. Data Reduction

1. Conversion of Time-Of-Flight Spectra to Energy Spectra

A TOF spectrum can be converted into an energy spectrum by equations IV-1a and IV-1b if the time calibration of the system is known; the calibration of the TOF TAC is derivable from the location of the two γ-ray peaks. Figure 14 shows a typical neutron TOF spectrum with its associated gamma spectrum. If n_1 and n_2 are the channel numbers

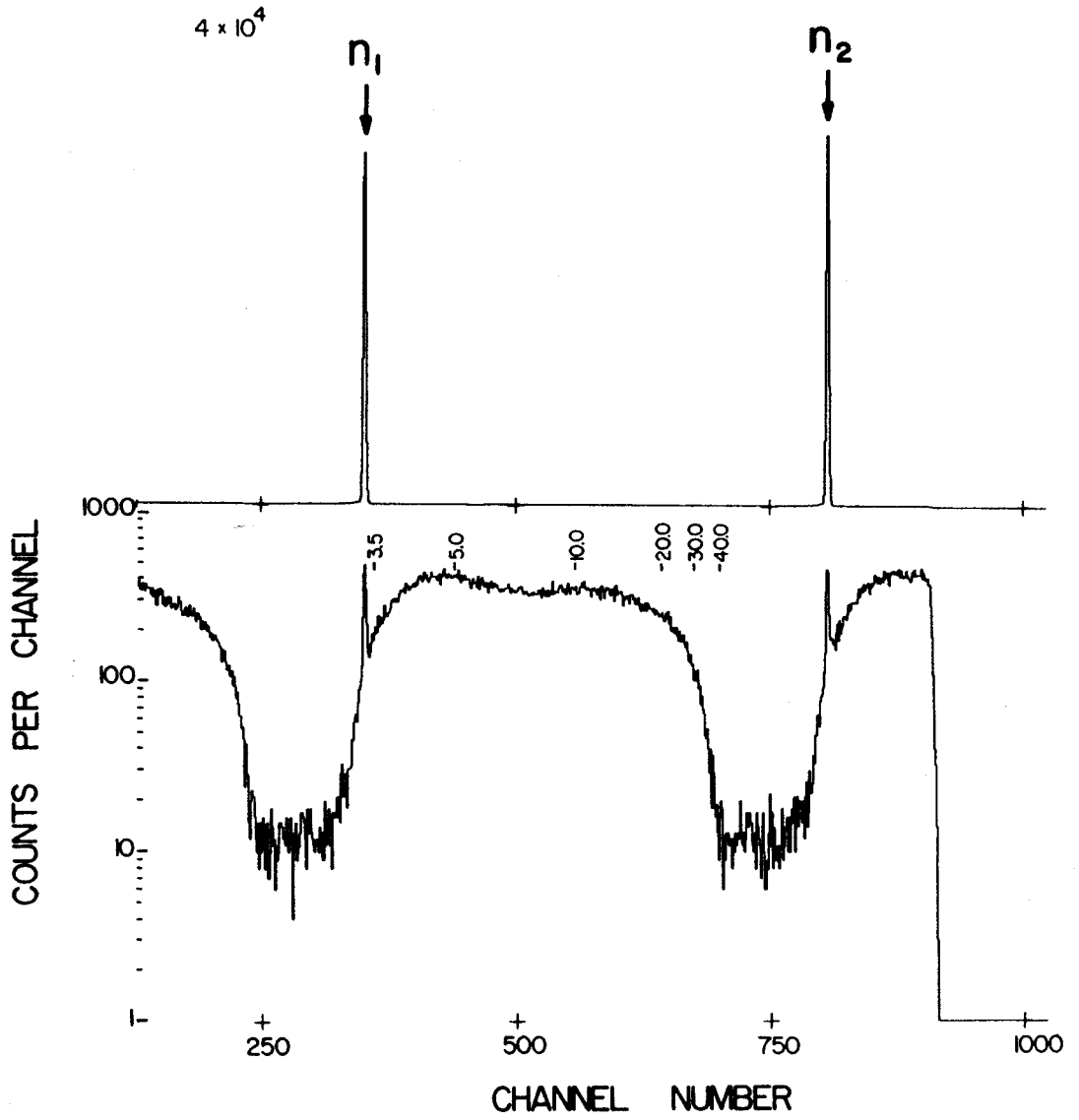

Figure 14. Typical Neutron and Gamma-Ray Time-of-Flight Spectra

of the two gamma peaks, as indicated, then the expression for the total TOF corresponding to the i^{th} channel is given by

$$t_i = \frac{L}{c} + \frac{n_2 - i}{(n_2 - n_1)f} \qquad \text{(IV-5)}$$

where L is the flight path, c is the speed of light, and f is the frequency of the rf accelerating voltage; the time difference corresponding to the channel number difference $n_2 - n_1$ is equal to the period of the accelerator. Then the neutron velocity is $v_i = L/t_i$, and the neutron energy corresponding to channel i is given by

$$T_n(i) = M_n c^2((1 - v_i^2/c^2)^{-\frac{1}{2}} - 1) \qquad \text{(IV-6)}$$

where M_n is the neutron mass; the energy width of channel i is given by

$$\Delta T(i) = T(i) - T(i-1) \qquad \text{(IV-7)}$$

If the number of counts in channel i is N(i), then the neutron yield (in units of neutrons/proton/sr/MeV) is given by

$$Y(i) = 2N(i)/\Delta T(i)\Delta\Omega q\varepsilon(T(i)) \qquad \text{(IV-8)}$$

where q is the number of incident protons, $\Delta\Omega$ is the solid angle subtended by the detector, and ε E(T(i)) is the detector efficiency for neutrons of energy T(i), and the factor of 2 appears since the TOF spectrum was doubled.

The TOF spectra were converted to energy spectra using a digital computer. The TOF data were summed over a number of channels corresponding to the experimental resolution as measured by the full-width-

at half maximum (FWHM) of the γ-ray peak; channel-by-channel conversion is not necessary since the flight times are only determined to within the FWHM. Summing in this manner also masks out unimportant statistical variations in the TOF spectra, and gives smooth energy spectra without altering any essential features of the data.

2. Calculation of Detector Efficiency

a. Statement of the Problem

The most important factor affecting the absolute normalization of the data, aside from the measured incident flux, is the efficiency of the neutron detector. This efficiency is a function of neutron energy and also depends strongly upon the following factors: (1) the detector threshold; (2) the response of the detector to recoiling charged particles of various energies; (3) the neutron cross-sections of the detector components. Cross sections (3) have been measured over the neutron energy range of interest and are tabulated in reference Ku 64. (1) and (2) depend upon the particular detector used and its associated electronics, and must be measured for each individual apparatus.

The detector efficiencies in this experiment were calculated using a modified version of the computer program TOTEFF developed by Kurz (Ku 64). The accuracy of this calculation has been investigated extensively and compared with experimental efficiency measurements (We 62, Bo 62, Hu 70) and found to be accurate within Kurz's error estimate of ±10%, even though it does not include edge- and end-effect corrections; rescattering contributions are included. The principal contributions to the uncertainty in the calculation, at neutron energies greater

than 10 MeV, arise from uncertainties in the measured cross sections for neutron-carbon reactions. In general, however, the accuracy of the calculation has been well verified. Two calculated efficiency curves used in the experiment are shown in Figure 15.

b. Measurement of Detector Threshold and Light Resolution

For a given detector size, the two most important parameters for calculation of the efficiency are the lower level pulse height threshold, and the light resolution at that threshold; they are particularly important for neutrons which cause pulses which just barely exceed the threshold.

TOTEFF requires that the detector threshold be known in terms of "equivalent electron energy", i.e., that the response of the detector to recoiling electrons of various energies be measured. The measurement was performed by using gamma-ray sources of known energies which emit only one or two well separated gamma rays; such sources yield pulse height spectra, in the detector which are characteristic of recoiling electrons with well defined compton edge energies. A typical pulse height spectrum for ^{60}Co is shown in Figure 16a, with the Compton energy for the 1.33 MeV gamma ray indicated; the Compton spectrum of ^{57}Co with the 41 keV compton edge and 123.5 keV full energy peak indicated is shown in Figure 16b. The maximum energy E of the recoiling electrons is related to the gamma-ray energy by (Ev 55)

$$E = E_\gamma R/(1 + R) \qquad \text{(IV-9a)}$$

where

$$R = 2E_\gamma/M_e c^2 \qquad \text{(IV-9b)}$$

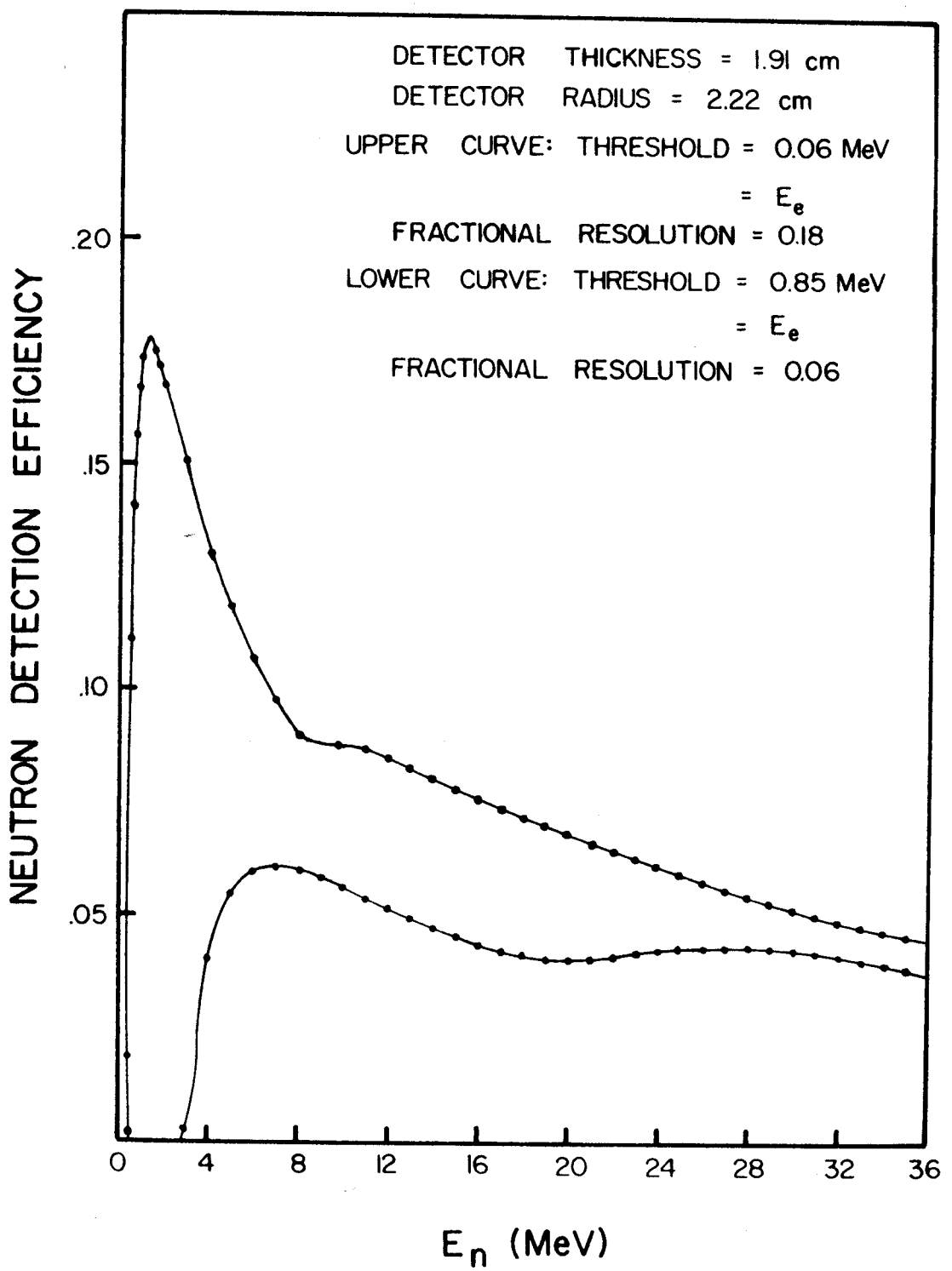

Figure 15. Calculated Neutron Detection Efficiencies

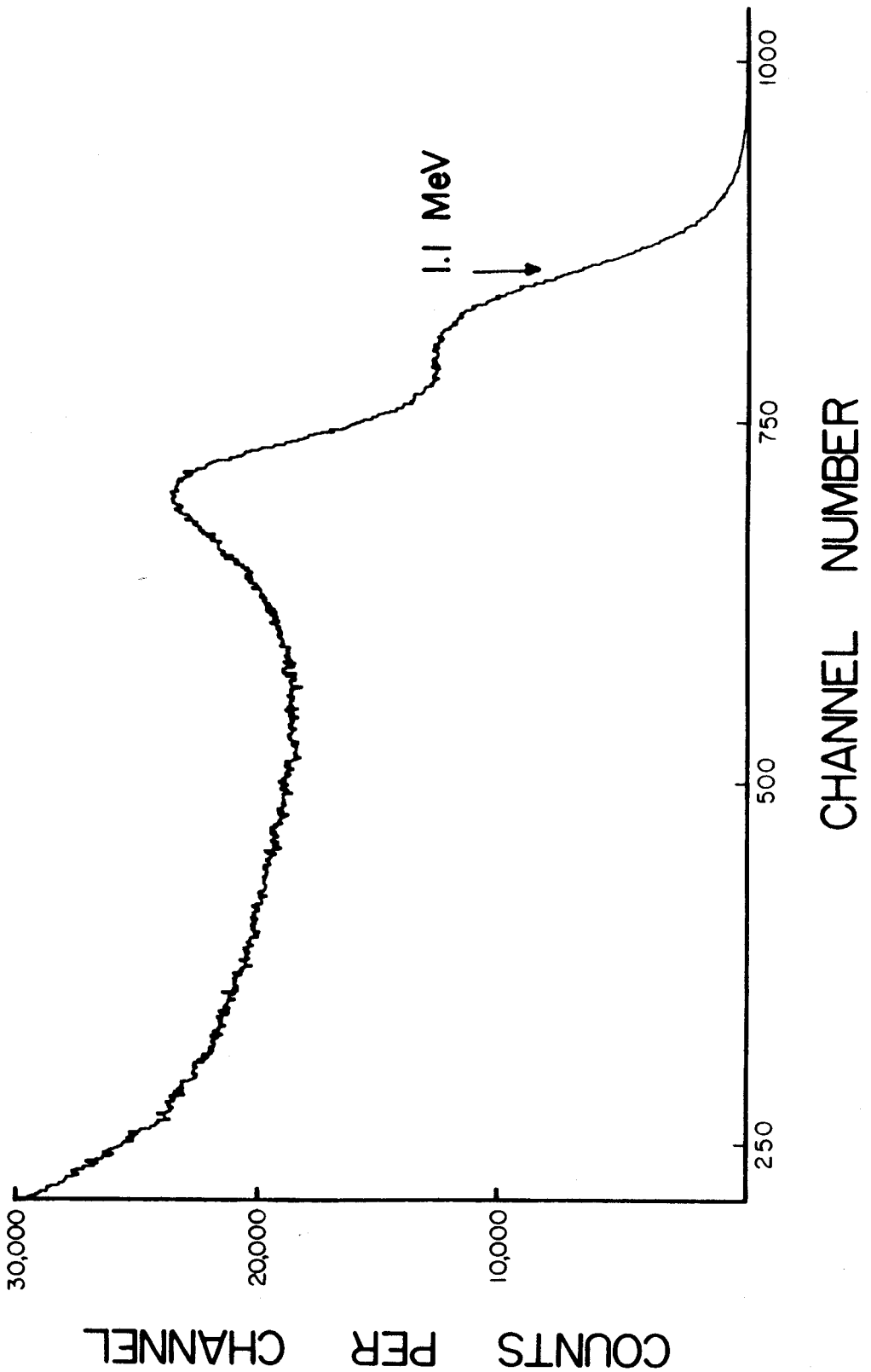

Figure 16a. ^{60}Co and ^{57}Co Compton Recoil Spectra

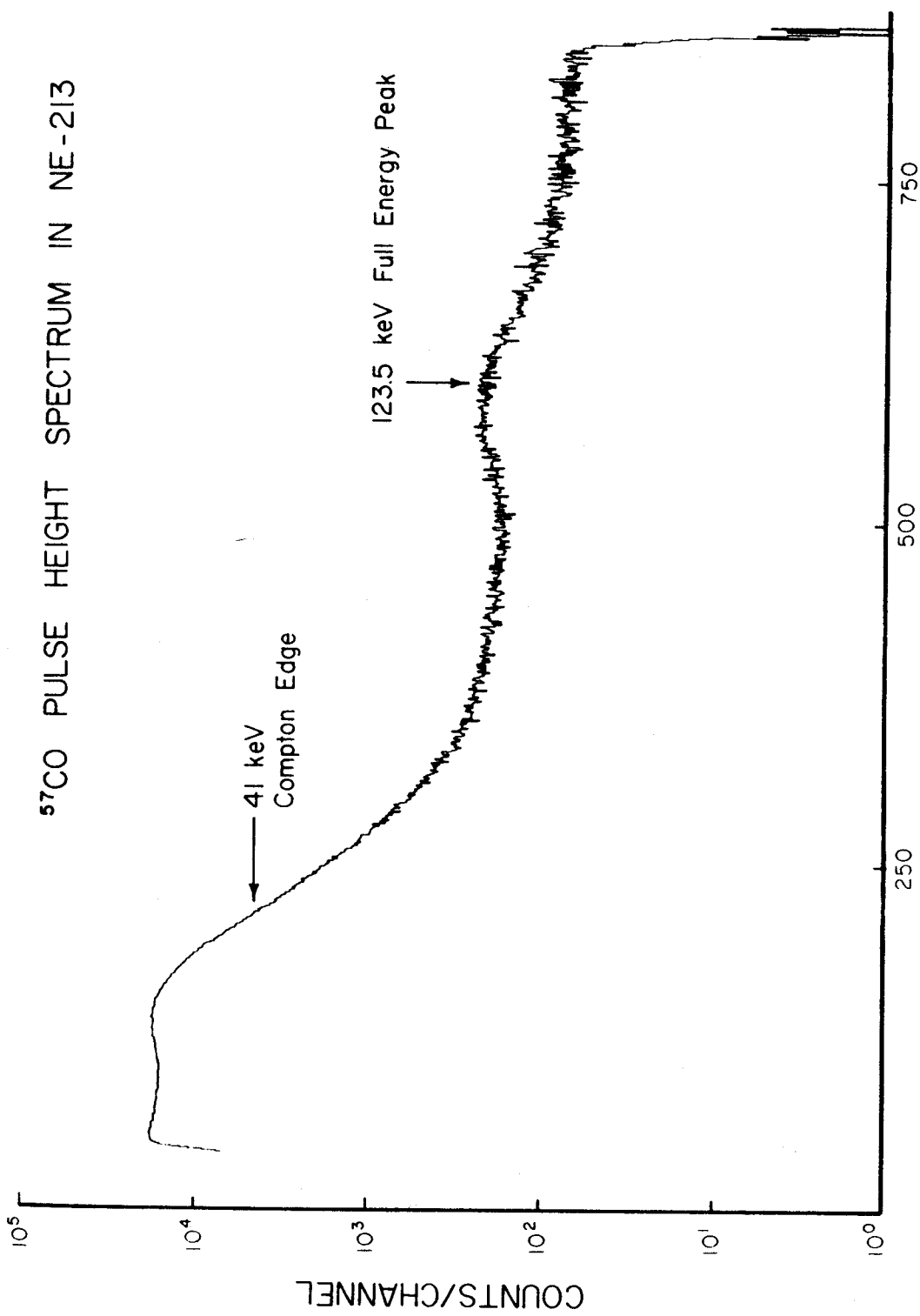

Figure 16b. ^{60}Co and ^{57}Co Compton Recoil Spectra

M_e being the electron mass and c the speed of light. The two TSCA-DDL amplifier combinations used in the experiment were calibrated as follows. The Compton recoil spectra were accumulated using a Nuclear Data ND160 multi-channel analyzer; the zero level of the analyzer had been previously set using a precision pulser. The TSCA dial was moved until no events below the Compton edge were accepted; the resulting curves of TSCA dial setting vs electron energy are shown in Figures 17 and 18. A number of gamma sources were used to cover the widest possible range of electron energies: ^{57}Co, ^{203}Hg, ^{22}Na, ^{137}Cs, ^{60}Co, ^{208}Tl, and $^{12}C^*$ in a Pu-Be neutron source; use of the last source required PSD. These sources, their gamma ray energies and corresponding Compton edge energies are listed in Table 1.

The light resolution as a function of electron energy was measured as the energy difference between two points on the Compton edge spectrum; as illustrated in Figure 19, these points were taken to be the energies at which the Compton curve passed through 75% and 25% of its maximum value. Measured in such a way, the light resolution corresponds closely to the full width at $e^{-1/2}$ of a Gaussian resolution function centered at the Compton energy. It is proportional to $E_e^{\frac{1}{2}}$ and its magnitude depends on the light collection efficiency of the scintillator, the efficiency of the PM photocathode, and the design characteristics of the PM; the fractional (percentage) resolution of the system is then proportional to $E_e^{-\frac{1}{2}}$. The fractional light resolution measured for the experimental system is shown in Figure 20 as a function of recoil electron energy.

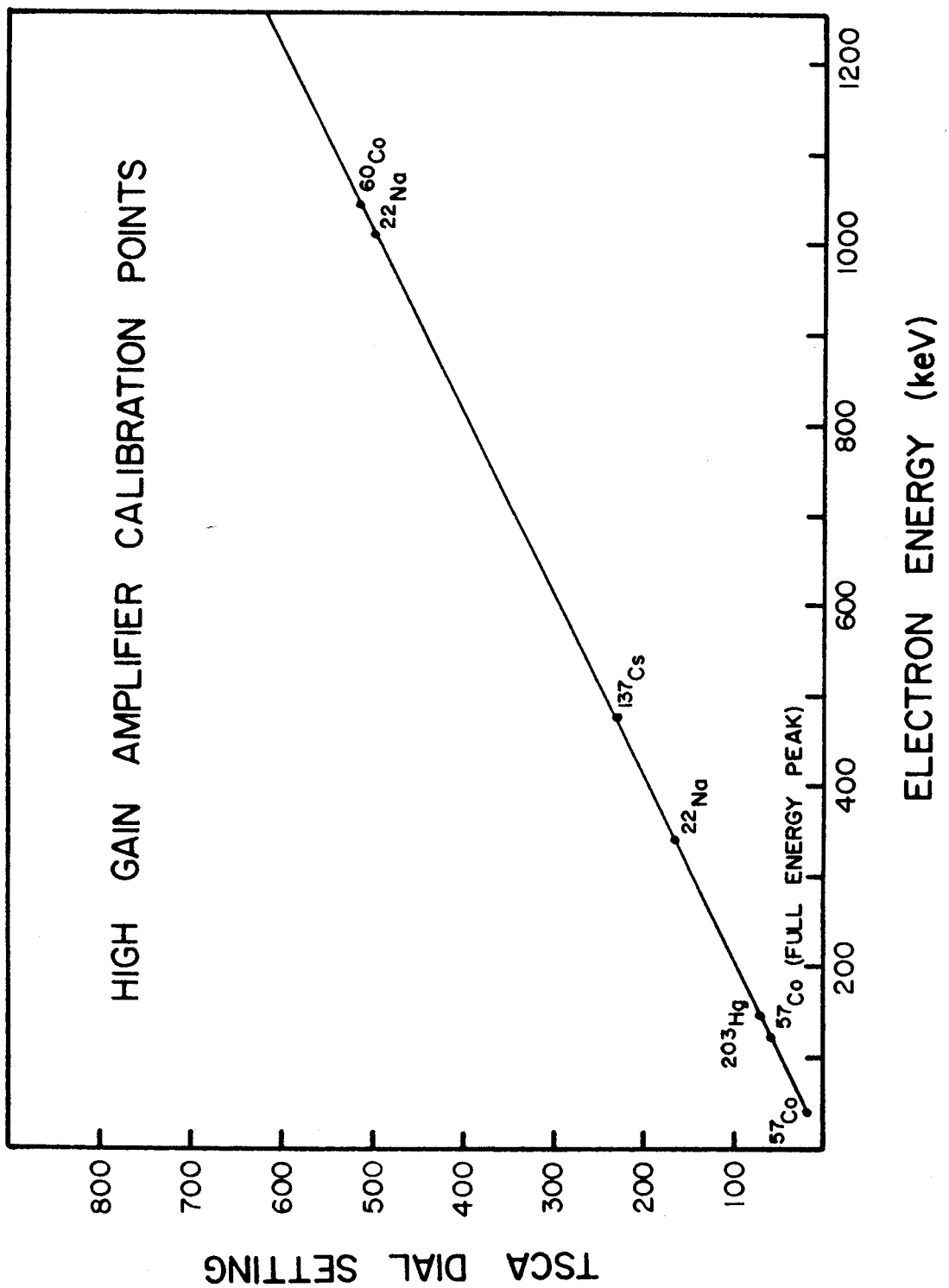

Figure 17. Single Channel Analyzer Calibration Curve

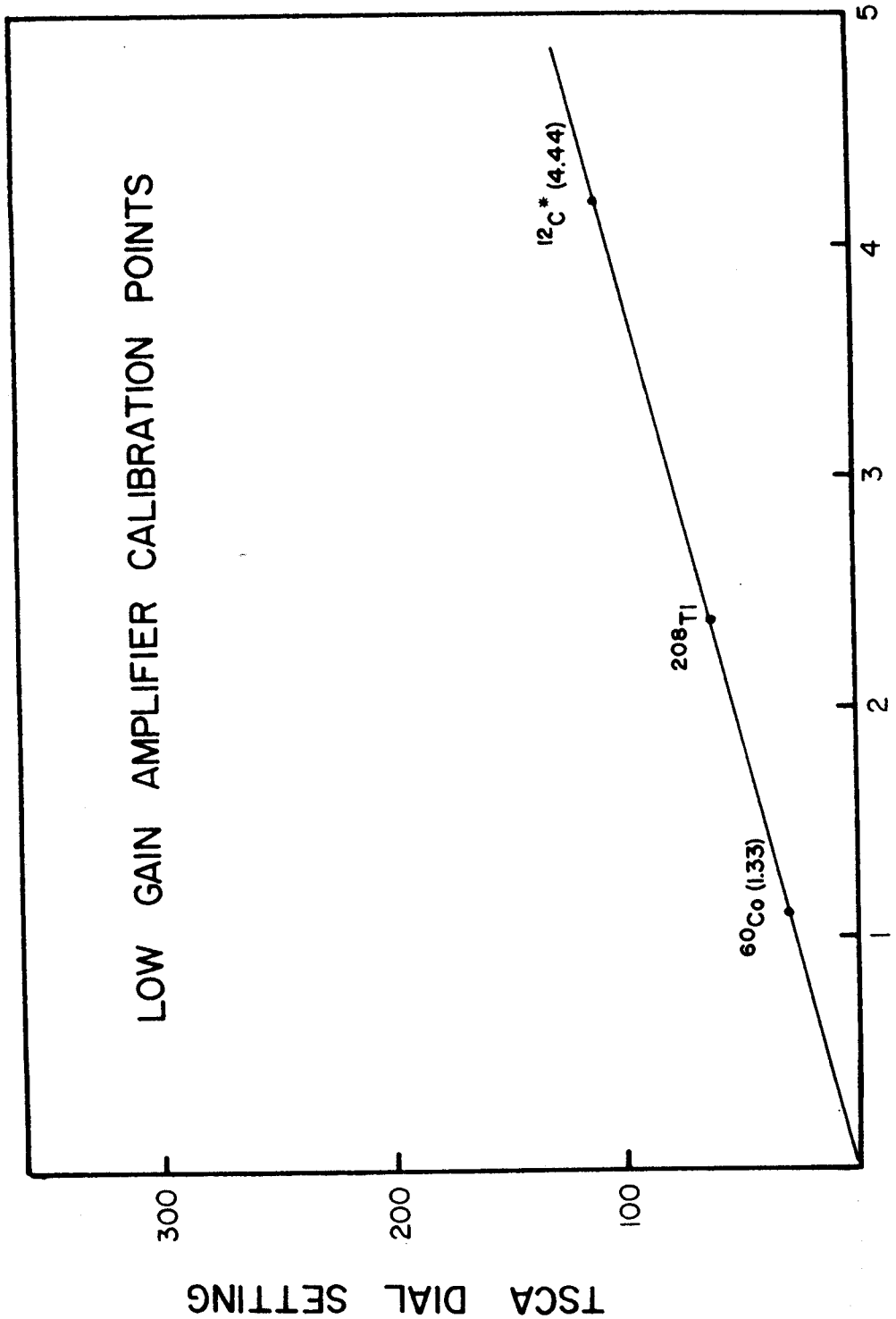

Figure 18. Single Channel Analyzer Calibration Curve

Source	E_γ (keV)	$E_{Compton}$ (keV)
^{57}Co	123.5	41
^{203}Hg	279	146
^{22}Na	511	341
^{137}Cs	662	478
^{60}Co	1330	1116
^{22}Na	1280	1067
^{208}Tl	2640	2380
$^{12}C^*$	4440	4190

Table 1. Gamma-Ray Sources, Their Decay Energies, And Compton Edge Energies

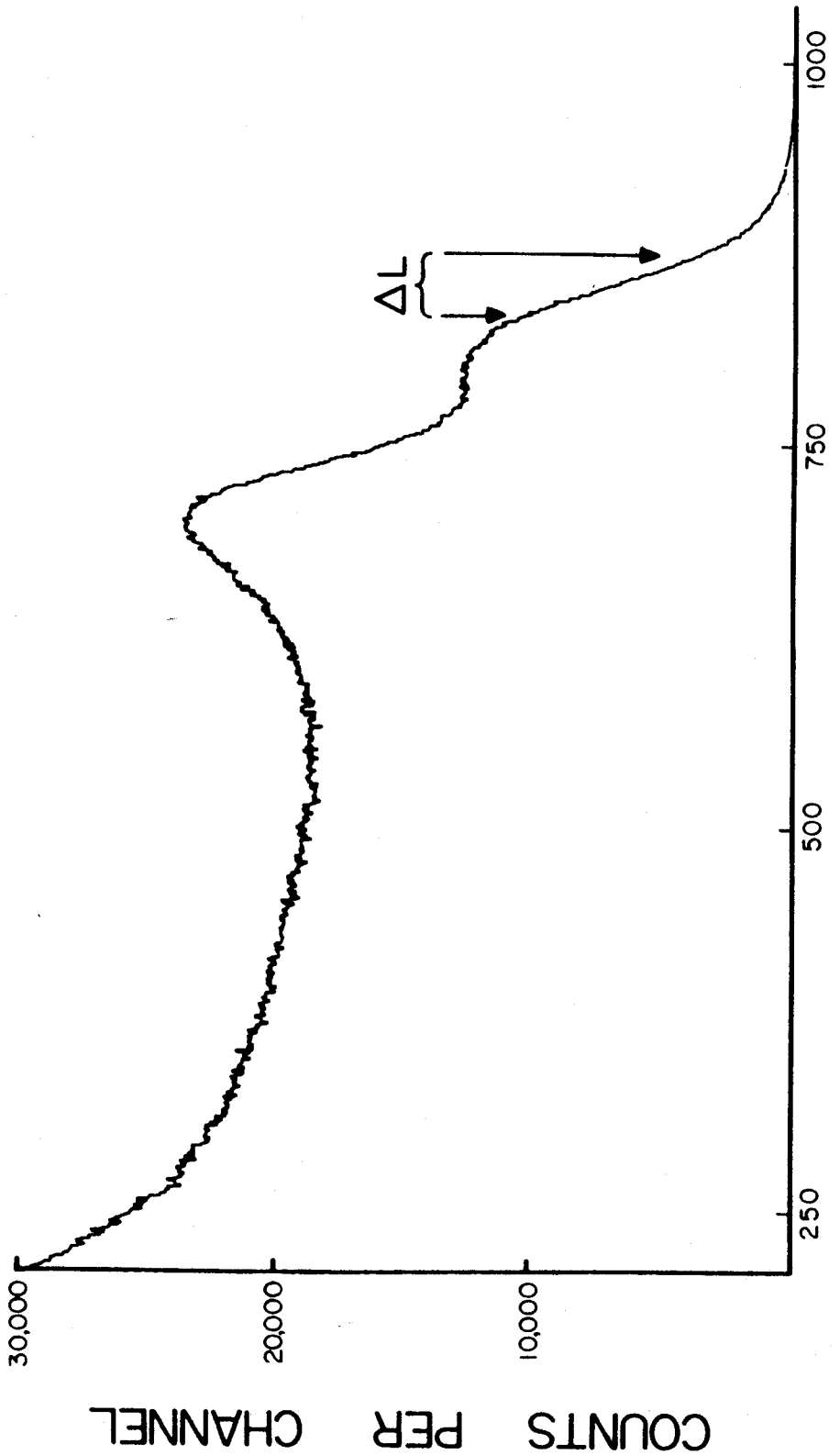

Figure 19. ^{60}Co Compton Recoil Spectrum Showing Detector Light Resolution

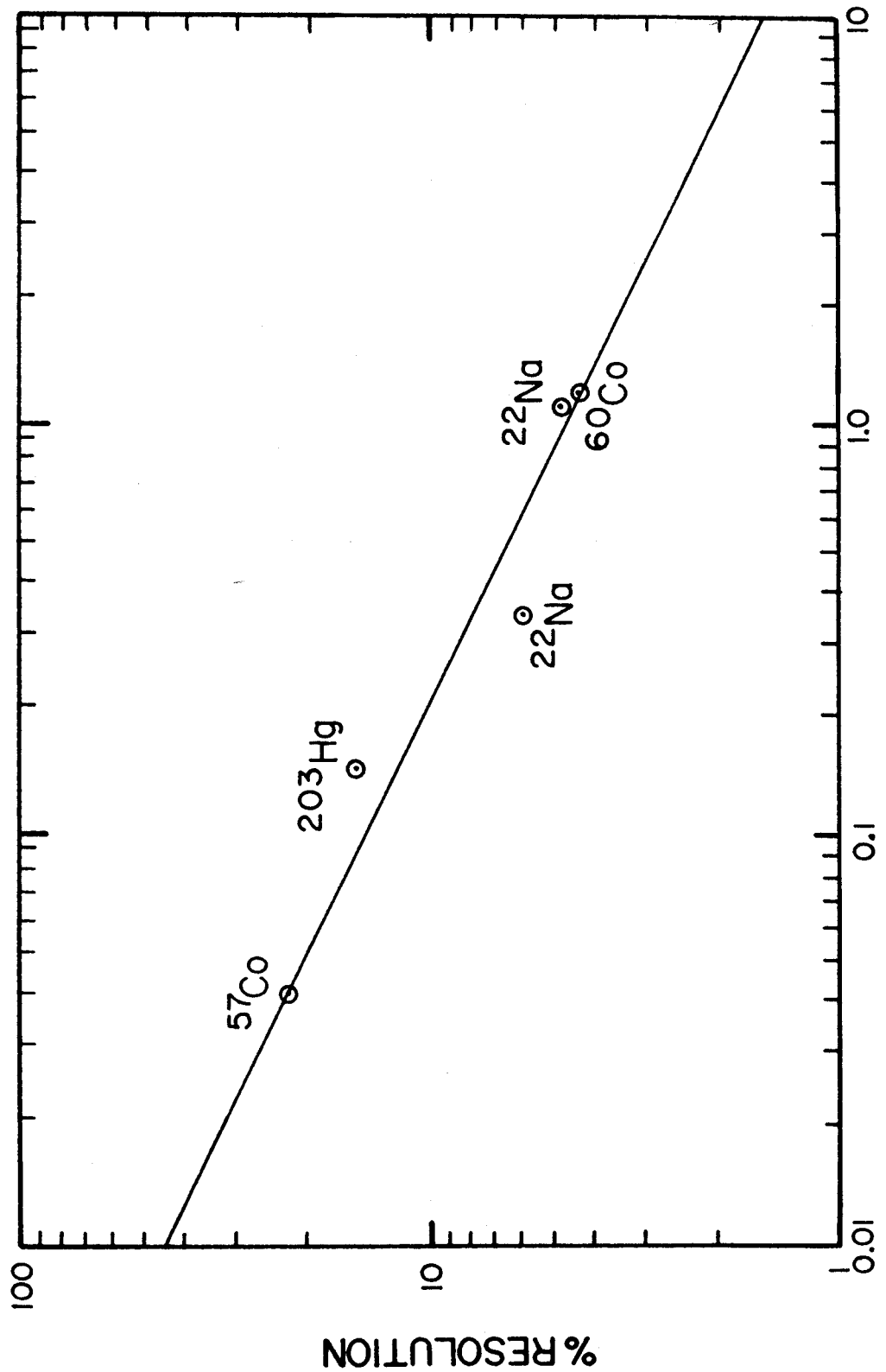

Figure 20. Detector Light Resolution Curve

c. Measurement of Detector Response Function

Apart from the threshold and light resolution the detector efficiency depends upon the response of the scintillator to charged particle recoils, especially recoiling protons. This response function, or "light curve", relates the scintillator light output for a recoiling proton of a given energy to the energy of an electron which causes the same pulse height.

The following simplified example shows how the efficiency depends upon the light curve. If monoenergetic neutrons are incident upon the detector, and their energy is below the threshold for reactions with carbon (~7 MeV), then only n-p collisions will produce detectable events. The fraction of neutrons colliding with protons in a thickness x of scintillator is

$$N = 1 - \exp(-n\sigma_{np}(E_n)x) \qquad \text{(IV-10)}$$

The energy spectrum of the recoiling protons is shown in Figure 21a. Then the number of events per pulse height interval, as shown in Figure 21b is given by

$$\frac{dN}{dL} = \frac{dN}{dE_p}\frac{dE_p}{dL} \qquad \text{(IV-11)}$$

where L is the light output in electron energy units and, as shown in Figure 21a, dN/dE_p is constant. The efficiency is then given by

$$\varepsilon = \int_{th.}^{L(E_n)} \frac{dN}{dL}\, dL = \frac{dN}{dE_p} \int_{th.}^{L(E_n)} \frac{dE_p}{dL}\, dL \qquad \text{(IV-12)}$$

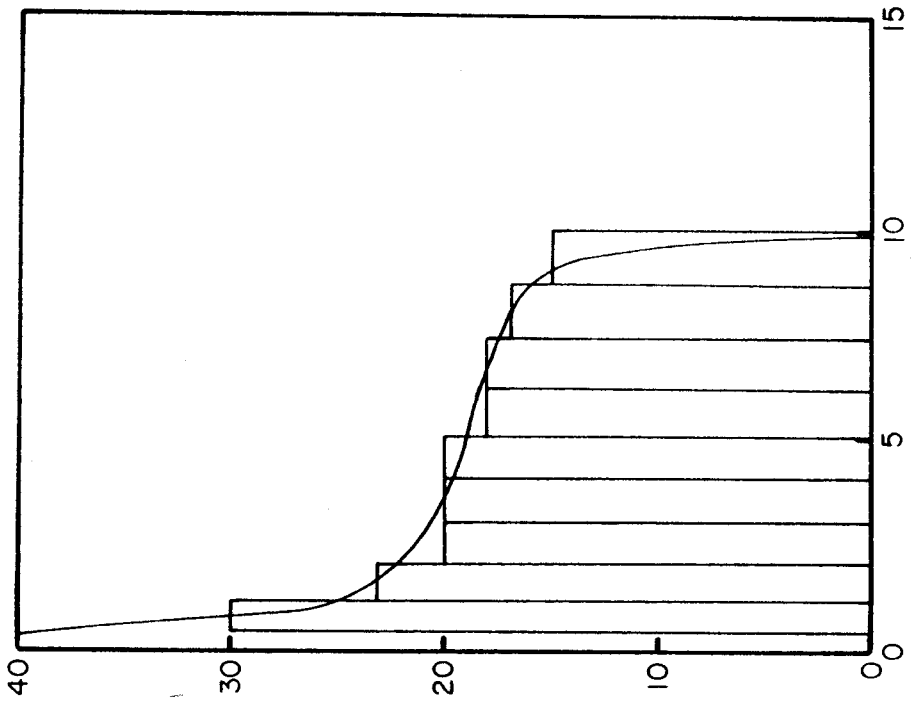

Figure 21b. Proton Recoil Energy and Pulse Height Spectra

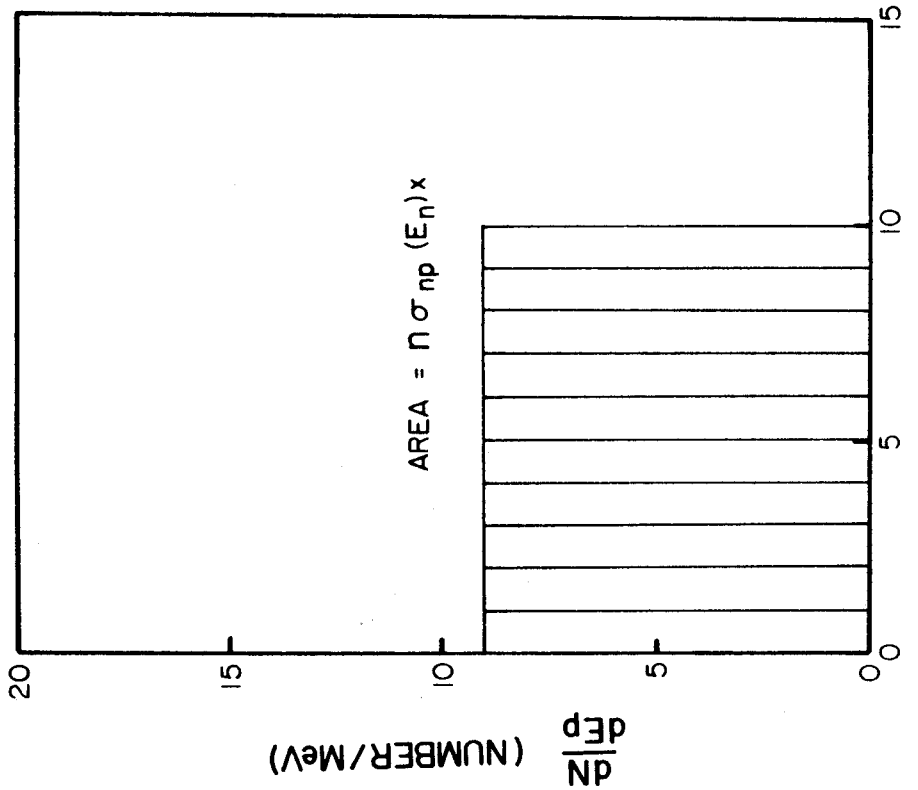

Figure 21a. Proton Recoil Energy and Pulse Height Spectra

The integral may be performed if $E_p(L)$ is known, $E_p(L)$ being the required light curve. Kurz (Ku 64) parametrizes the light curve measured by Gooding and Pugh as

$$E_p(L) = 11.5\ (1.0-\exp(-.2L^{.62})) + 1.077L \qquad \text{(IV-13)}$$

which applies to NE102 plastic scintillator. A measurement of the light curve for NE213 Verbinski et al. (Ve 65) yielded a slightly different result, one which can still be written in the above form, but with slightly different parameters. Another light curve for NE213 has been measured by Taylor and Kalyna (Ta 70) and differs from Verbinski's curve by about 10% in the neutron energy range of interest in this experiment. Because of this difference, the response of the detector used in this experiment was measured in the following fashion, and the light curve obtained was parametrized as above and used in TOTEFF.

A number of TOF spectra were taken which differed only in TSCA threshold; these spectra were converted to relative energy spectra and plotted as shown in Figure 22. The spectrum with the lowest threshold was converted with an efficiency calculation using Verbinski's light curve. Except near this lowest threshold, the shape of the spectrum should be correct. The other spectra were normalized to this one and extrapolated across their threshold regions, as shown in Figure 22. The threshold, E_{th}, is defined as the neutron energy where the measured spectrum is half the extrapolated value. This gives a relation between E_p and E_e, since the TSCA dial setting was already calibrated in units of electron energy (light output) as given by Figures 17 and 18. From these data a curve of E_p vs E_e was constructed, parametrized as

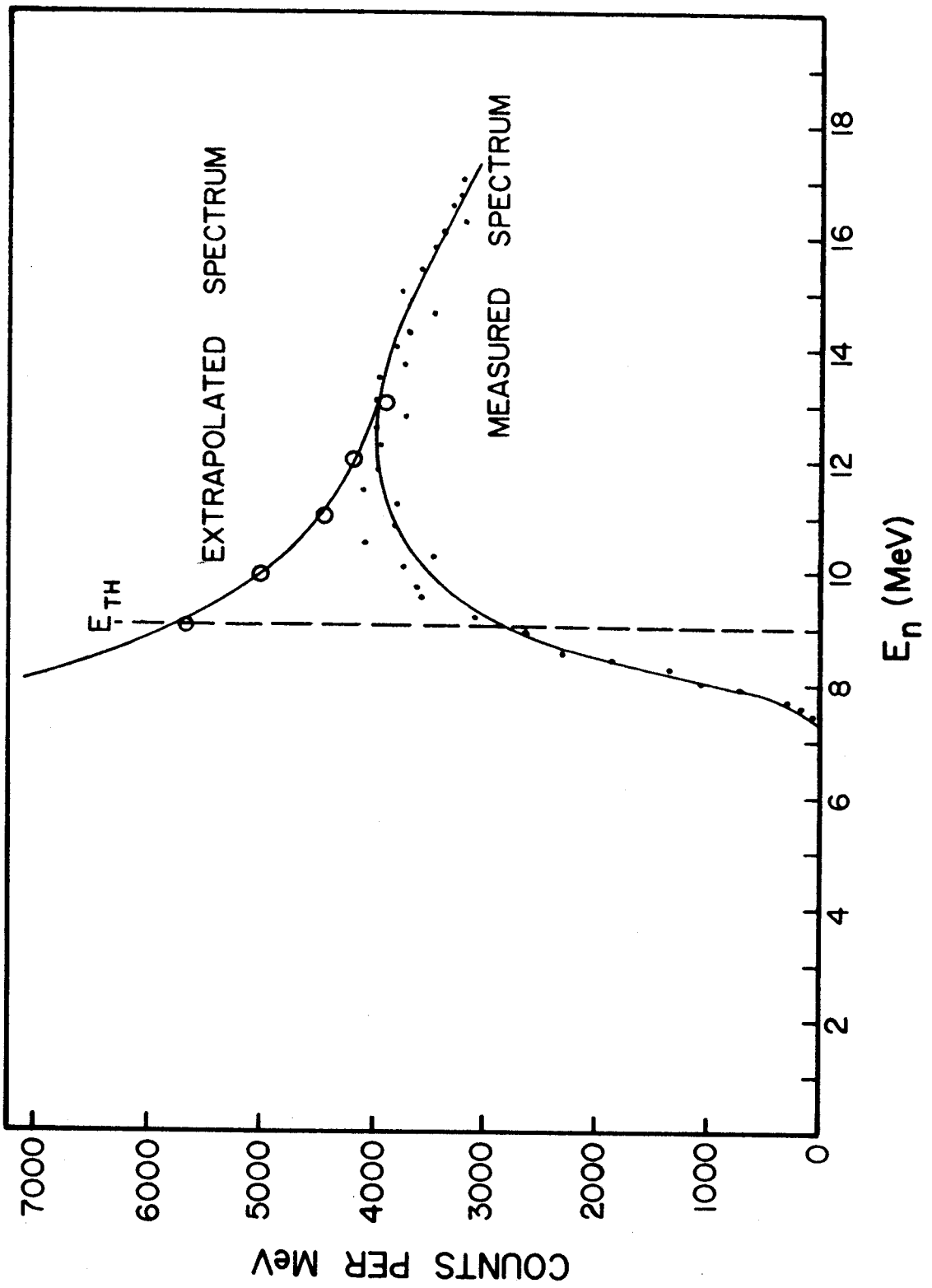

Figure 22. Relative Neutron Energy Spectrum

$$E_p(L) = 11.7(1.0-\exp(0.23L^{.62})) + 1.077L \qquad \text{(IV-14)}$$

and used in the efficiency code.

The light curve data, shown in Figure 23, agree well with the results of Verbinski. In any case the disagreement with the results of Taylor and Kalyna is probably not larger than the experimental errors of all three measurements, and seriously affects the results of TOTEFF only at neutron energies very near the threshold.

G. Corrections

1. Absorption and Inscattering

Neutrons produced inside a thick target must traverse a considerable amount of matter before escaping from the target; their possible interactions with target nuclei in their path through the target may distort the measured energy spectrum in several ways.

Neutrons may undergo either elastic or non-elastic interactions inside the target, and both of these types of interactions may cause "removal" of neutrons from the flux headed toward the detector, or may cause "inscattering", i.e., neutrons headed away from the detector may be scattered into it. Since the neutron spectra were taken in two sections each effect was calculated separately for each piece of a given spectrum.

The neutron cross sections used were taken from references Hu 58 and Ga 70. To simplify the calculations the cross sections used for the low energy neutron spectrum were taken to be those for 2 MeV neutrons; for the spectrum of neutrons above 3.5 MeV, the cross sections

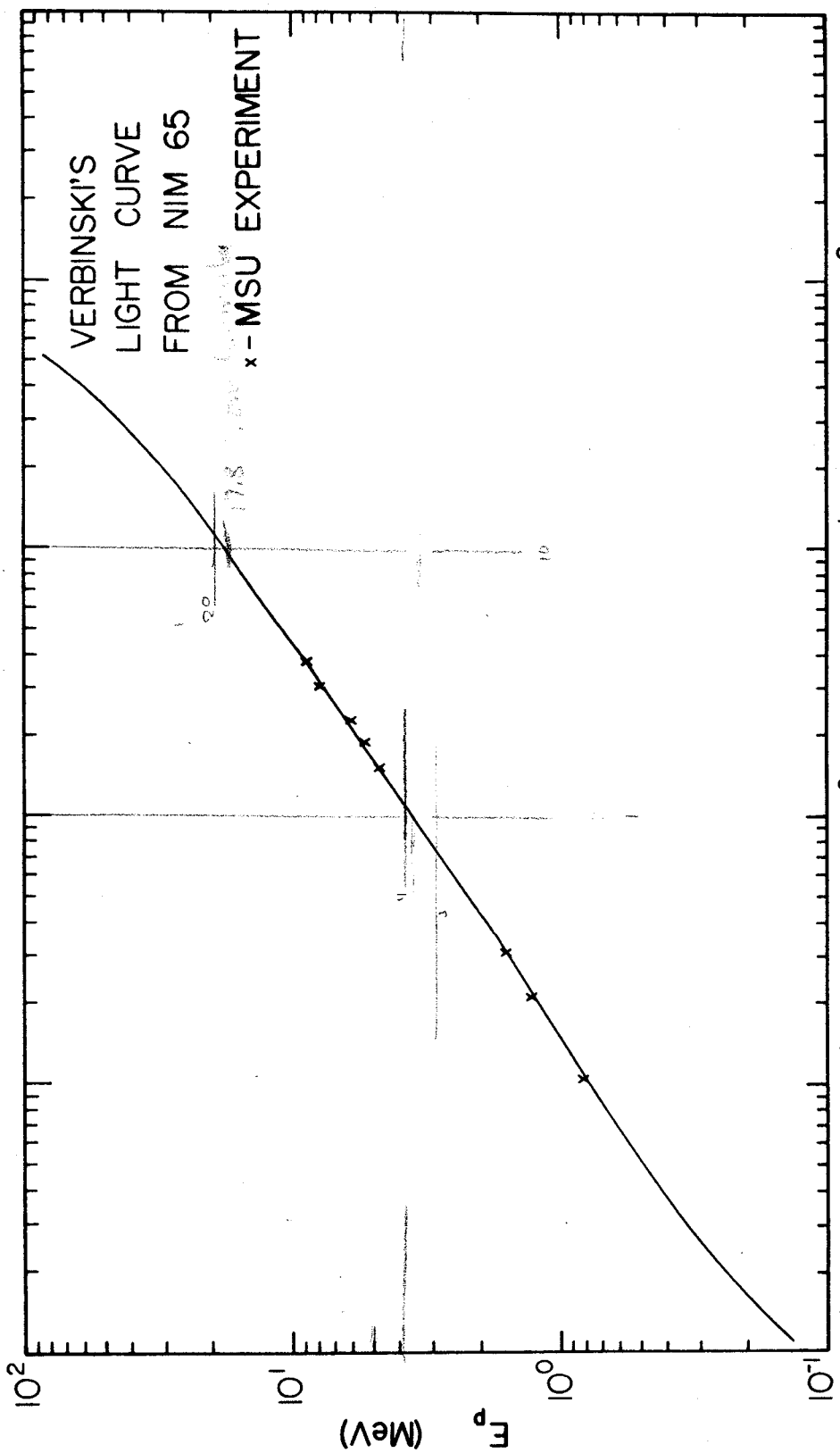

Figure 23. Detector Response Curve

used were those for 15 MeV neutrons.

For each target, the neutrons were assumed to originate at that point at which the full range inelastic collision probability of the incident protons is half of its original value (Ja 66); then, since the target thicknesses were known, the amount of material traversed by the neutrons for a given detector angle can be calculated (see Figure 24a). This quantity is vital to the calculation of the removal correction.

For the high energy neutron spectrum, the removal correction due to non-elastic reactions in the target was calculated, using the non-elastic cross sections tabulated in Hu 58. Since the elastic scattering angular distribution is strongly forward peaked at higher neutron energies (Ga 70), almost any neutron which is elastically scattered away from the detector will be compensated for by a neutron of the same energy which is scattered into the detector (the scattering angles are very small, typically less than 10°), so no correction for either removal or inscattering by this process is necessary.

Non-elastic reactions by high energy neutrons may lead to an isotropic evaporation neutron spectrum which would result in some small raising of the low energy end of the measured spectrum. It was estimated, on the basis of the measured energy spectrum, corrected only for the detector efficiency, that the number per unit solid angle of high energy neutrons was equal to 10% of the number of low energy neutrons. A given target was divided into 3 regions of scattering material as shown in Figure 24b, and the solid angles of each region were calculated; then the percentage correction for a given region is given by

$$c = n \left(\frac{d\sigma}{d\Omega}\right) \Delta\Omega \; x \qquad \text{(IV-15)}$$

where n is the number of target nuclei per cm^3, $\frac{d\sigma}{d\Omega}$ is the cross section for (n,n') reactions, assumed to be equal to the total non-elastic cross section divided by 4π, $\Delta\Omega$ is the solid angle of a given region, and x is an average distance to escape from that region.

The removal of low energy enutrons by non-elastic scattering was calculated and the correction applied to the data; this correction is small, because the non-elastic cross sections are small for low energy neutrons (Hu 58). The contribution of elastic scattering to the removal of low energy neutrons was also calculated since the elastic angular distributions are not so strongly forward peaked as at higher energies, and no "exact" compensation occurs.

The elastic inscattering correction for low energy neutrons was calculated by using equation IV-15 above, assuming the elastic scattering cross sections at low energy are isotropic and dividing the target into three regions as shown in Figure 24b.

The total correction was then applied separately to each high- and low-energy spectrum. The removal correction for the 40 MeV Pb target spectrum at 30°, is 2.2% for the high energy part of the spectrum and 4.25% for the low energy part; the total inscattering correction to the low energy Pb spectra at 40 MeV is 8.8%. A representative list of these corrections is given in Table 2.

2. Deadtime Correction

The deadtime of the ADCs was monitored during each run using the "channel zero" option of the data-taking code TOOTSIE. A logic pulse

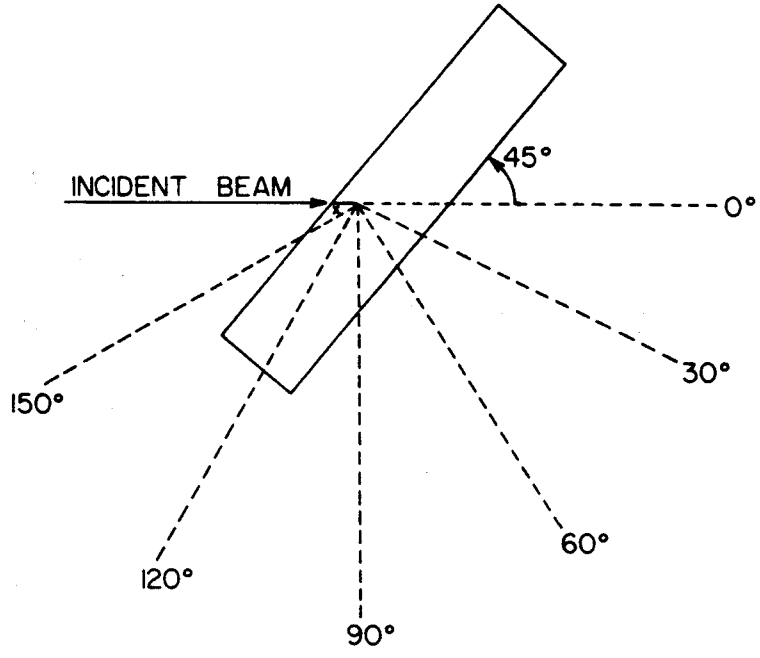

Figure 24a. Target Geometry for Corrections

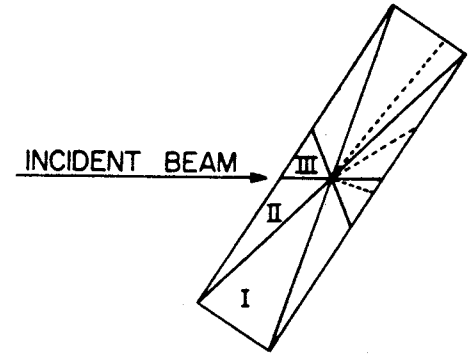

Figure 24b. Geometry for Inscatter and Outscatter Corrections

	% Inscatter	% Absorption
Pb	6.1	12.6
Ta	5.6	15.4
Ag	11.7	22.1
Cu	8.0	9.8
Al	9.8	12.5
C	19.3	22.2

Table 2. Absorption and Inscattering Corrections for 2.0 MeV Neutrons At Neutron Angle of 120° at E_p = 30 MeV

generated by a random frequency pulser and presented to the channel zero input was counted only if the ADCs are free to accept an event. So the fractional livetime of the ADCs is the ratio of the pulses counted to those presented. The beam currents used in the experiment were generally steady, so that no problem arose because of the source of channel zero pulses not being directly correlated with the beam (La 71).

The percentage deadtime corrections were included when the TOF spectra were converted to energy spectra. These corrections generally fell in the range from 5% to 15%, depending upon the beam current used and the yield from a given target.

H. Absolute Neutron Yield Spectra, Angular Distributions and Total Yields

The data converted from TOF spectra to energy spectra as previously described, with all corrections included, are presented in Figure 25 as absolute neutron yield spectra at each of six production angles. These yield spectra were then integrated over energy to obtain the angular distributions of all neutrons shown in Figure 26. The angular distributions were then integrated over angle to give, for each target and bombarding energy, the absolute total yields plotted in Figure 27.

These total neutron yields are presented in Figure 27, together with the total thick target yields obtained by Tai et al. (TA 57) at 18 and 32 MeV. The Tai experiment was performed by neutron activation of a manganese sulfate bath. When the great difference between the two techniques is considered, the agreement of the results of the two experiments is excellent, with regard to

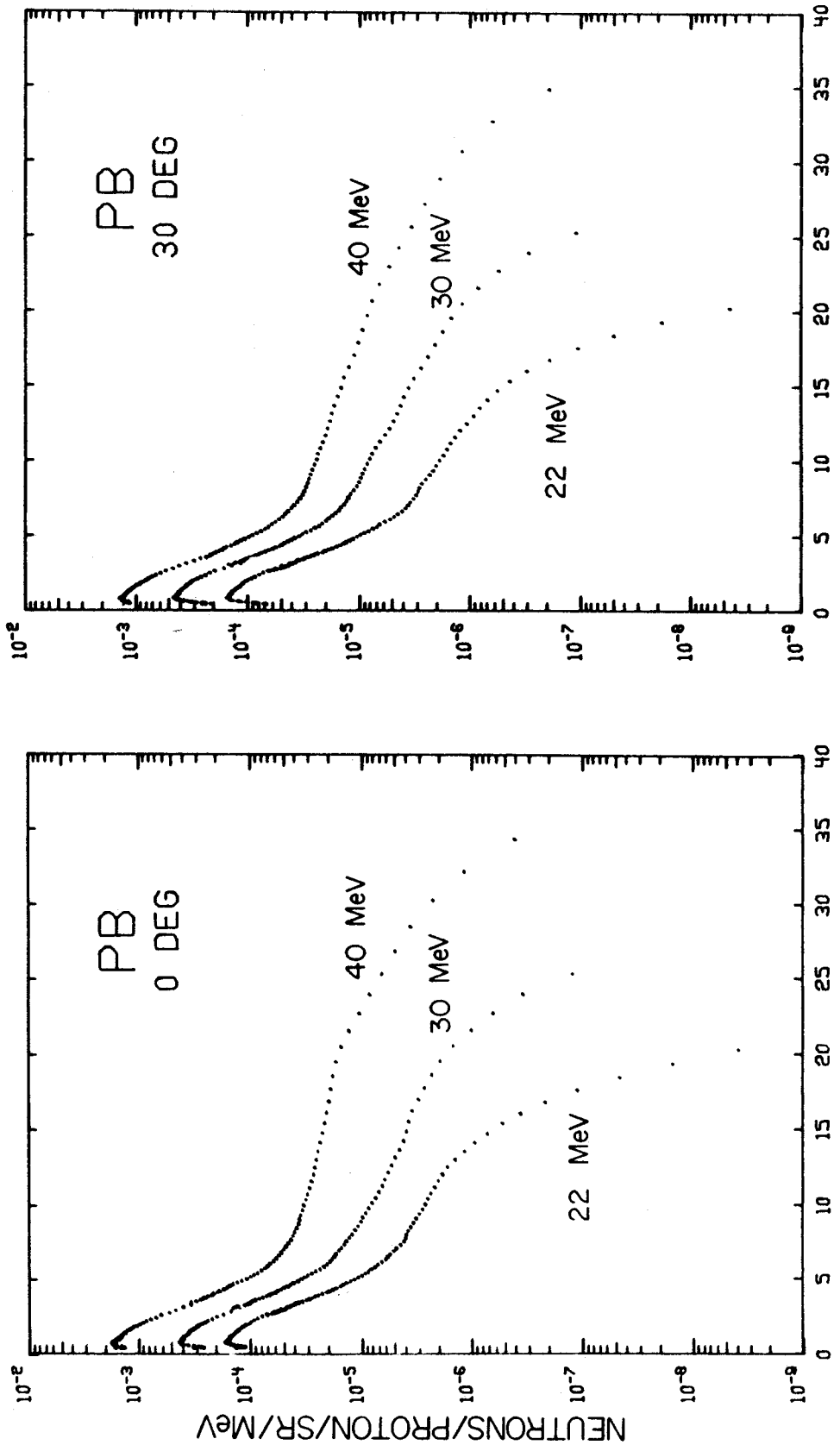

Figure 25. Neutron Yield Spectra

Figure 25. (continued)

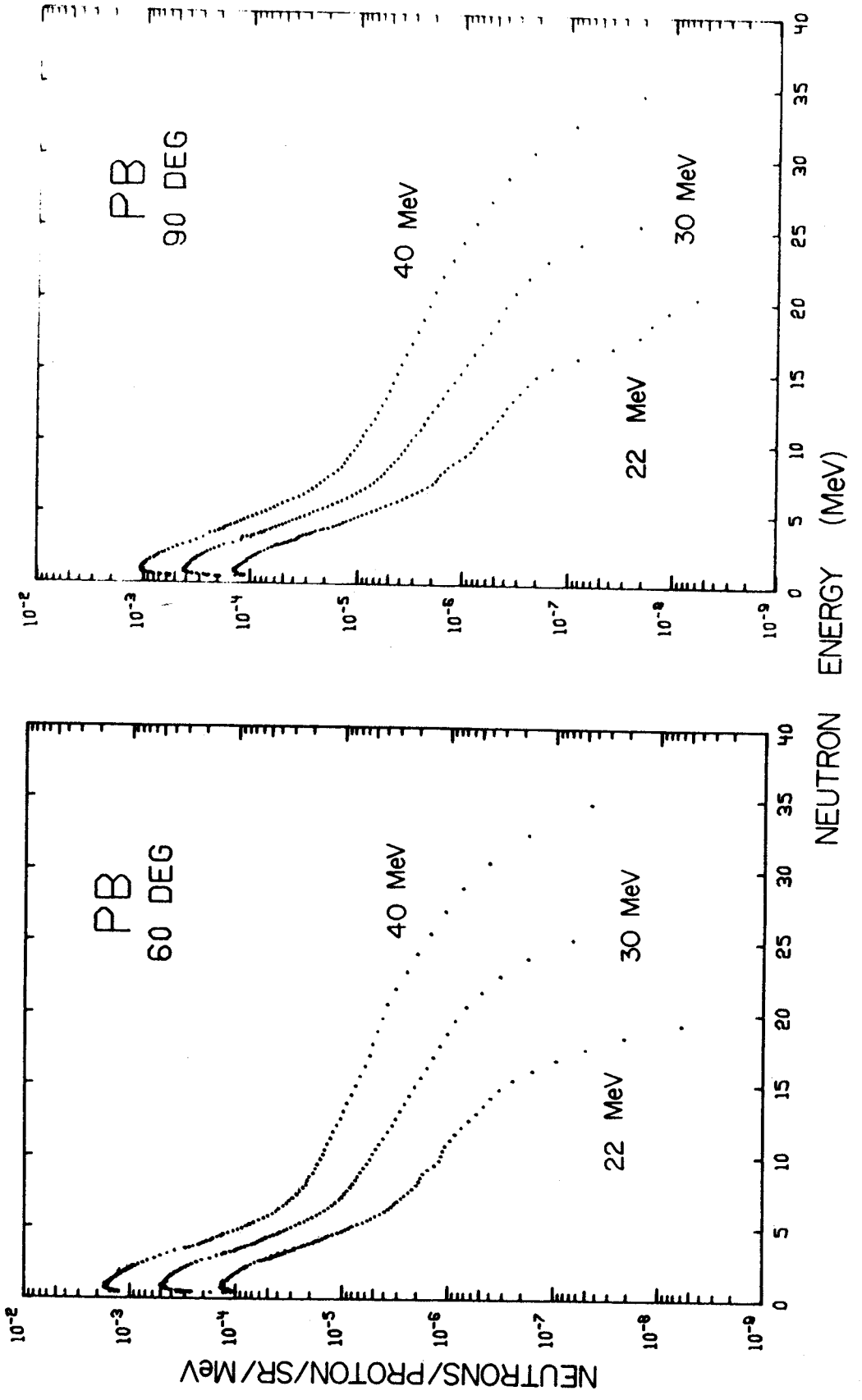

Figure 25. (continued)

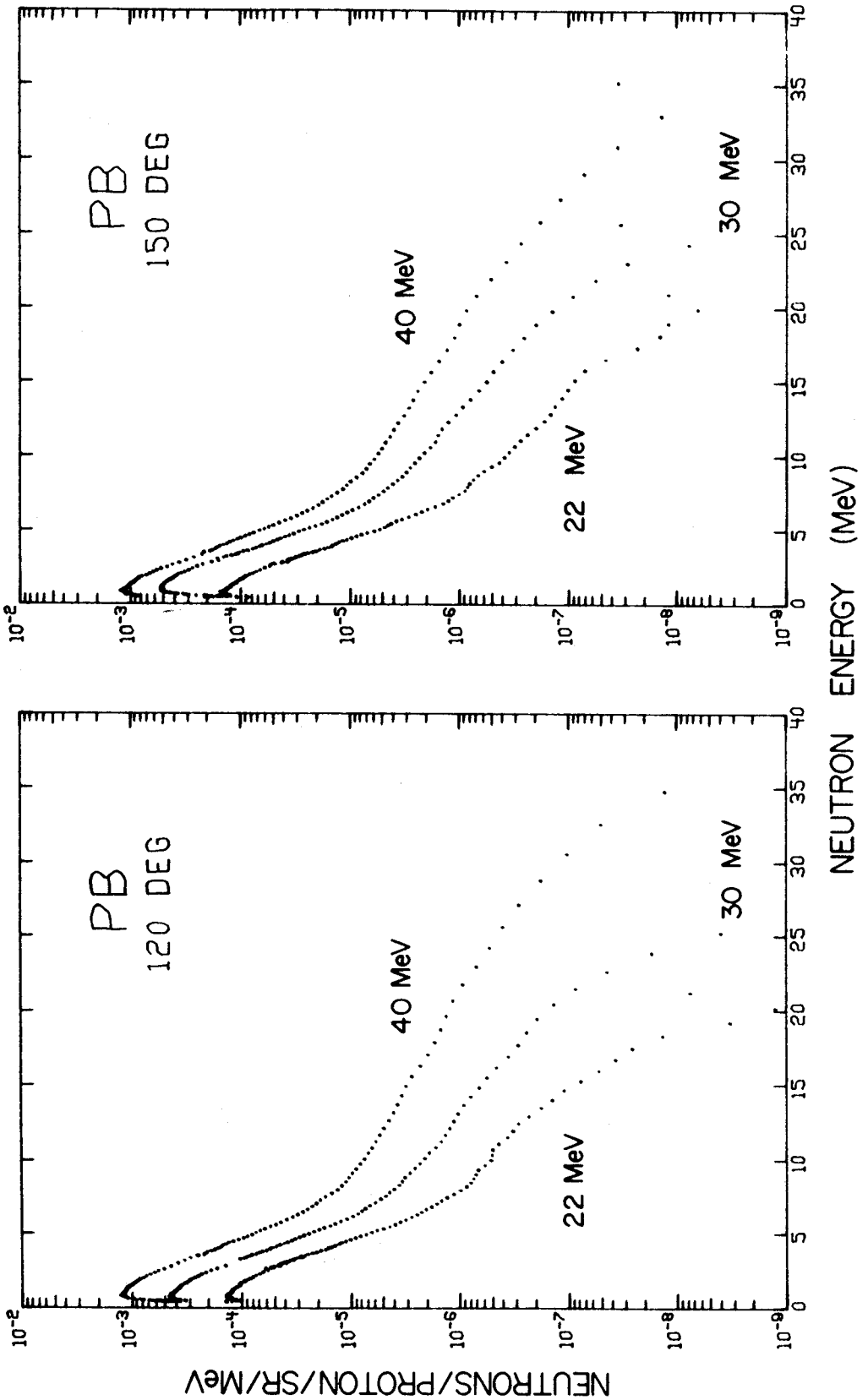

Figure 25. (continued)

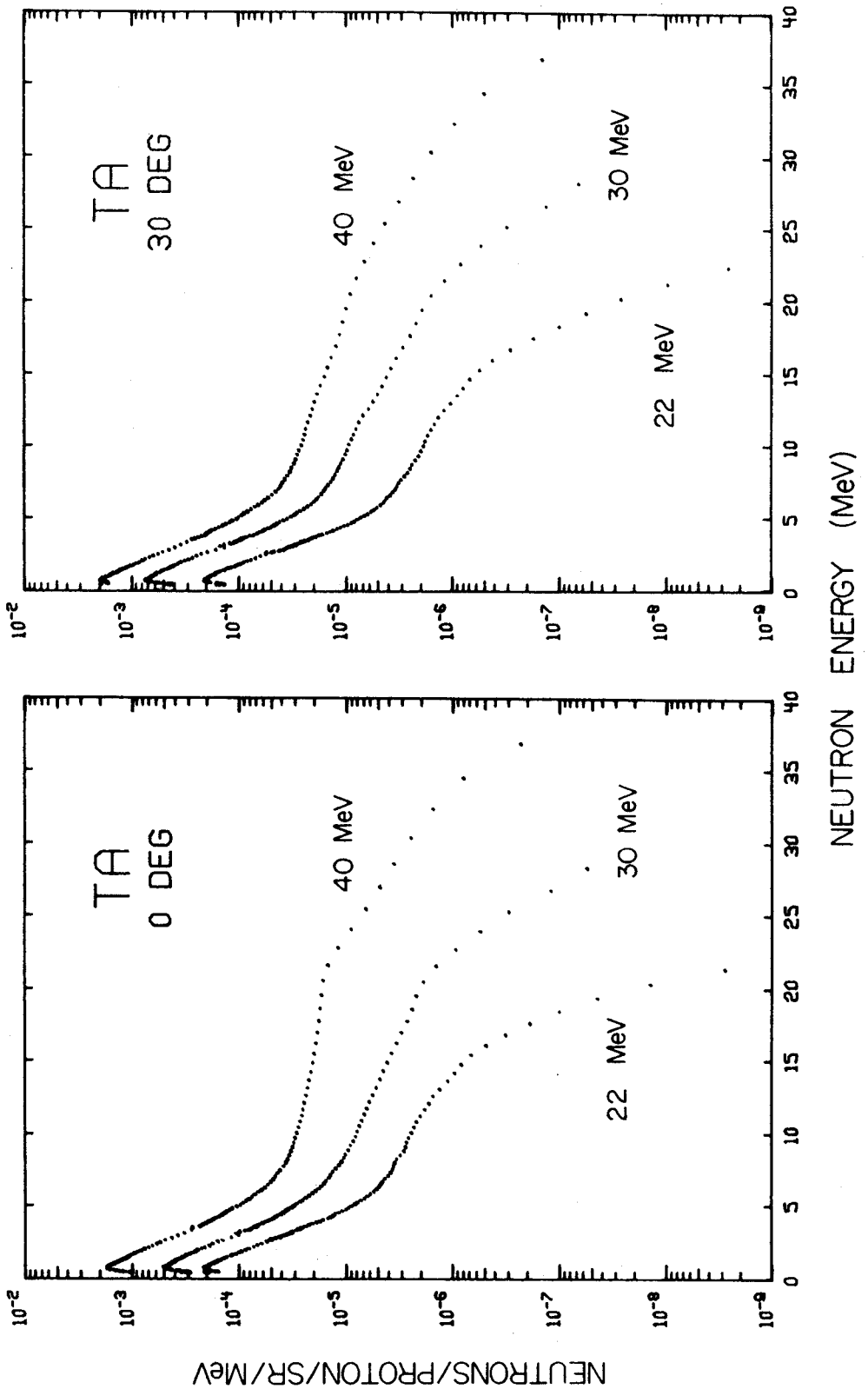

Figure 25. (continued)

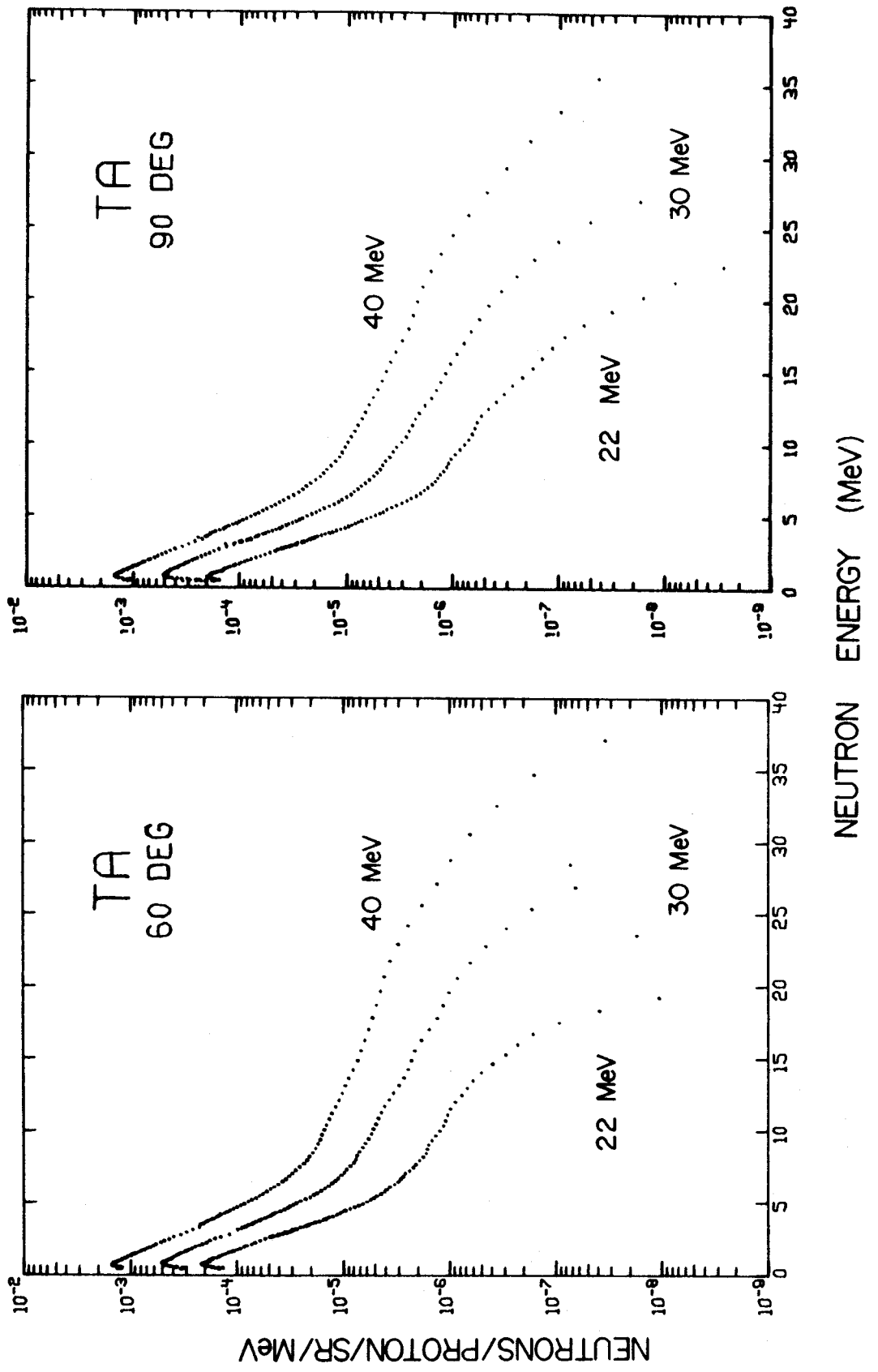

Figure 25. (continued)

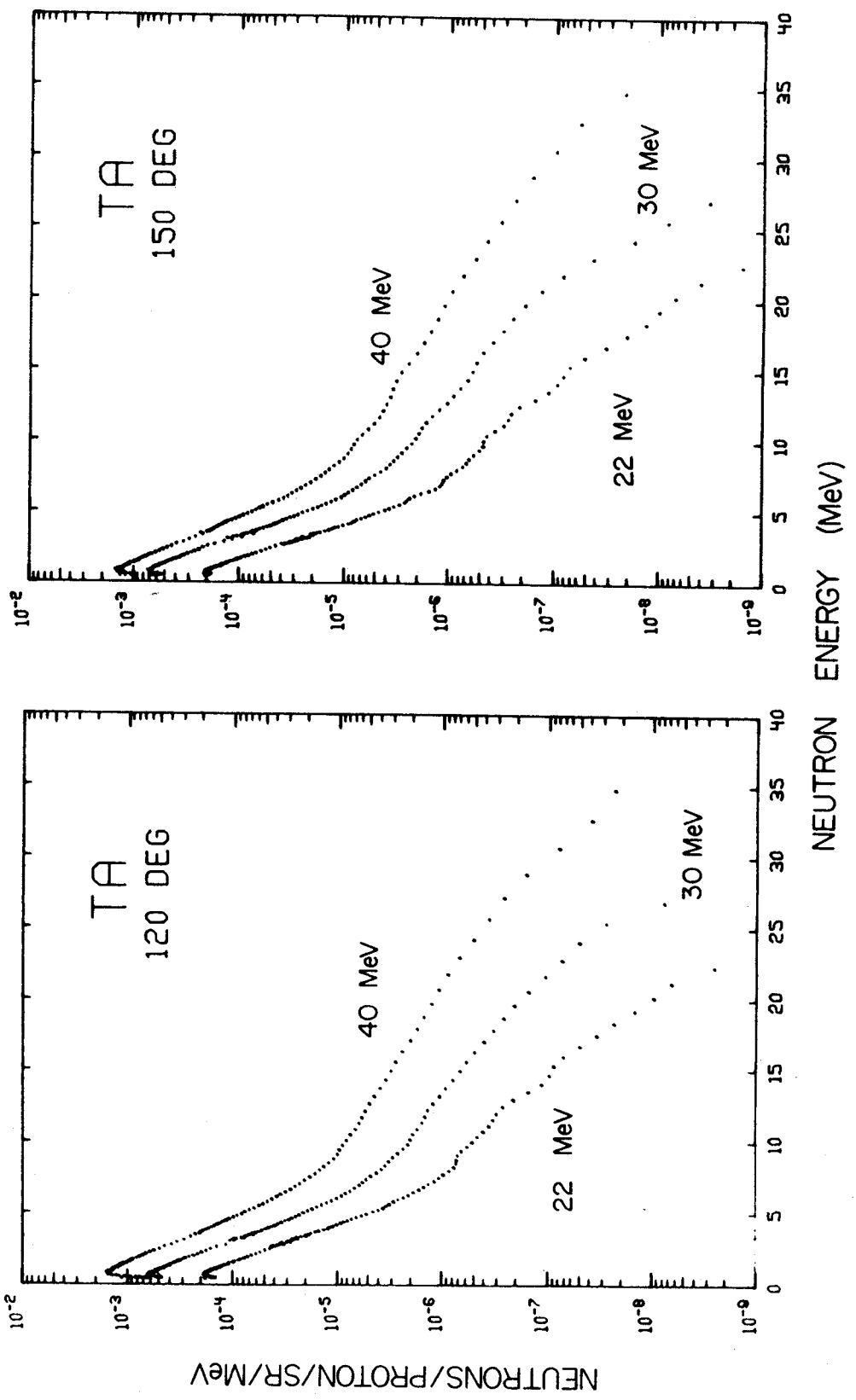

Figure 25. (continued)

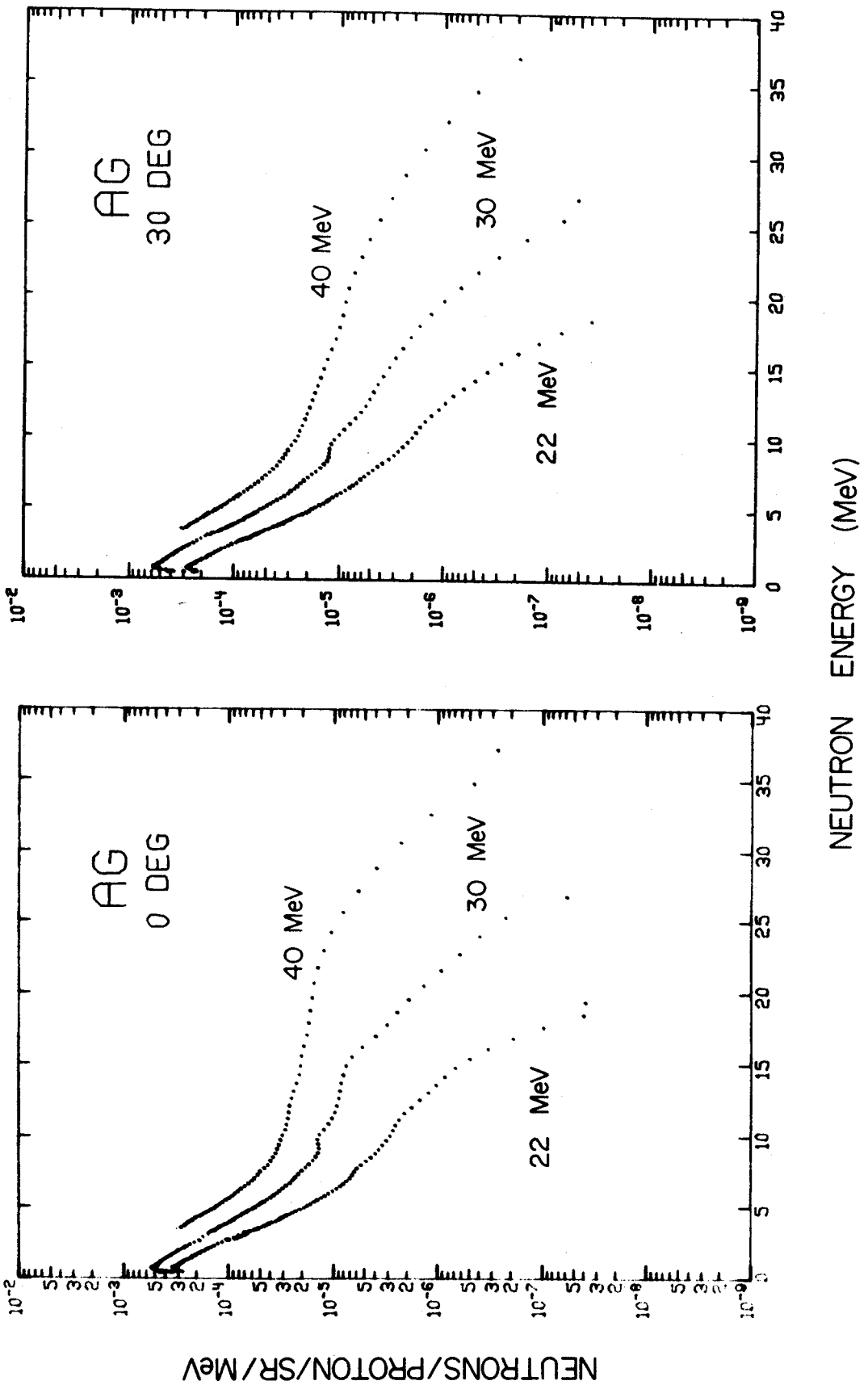

Figure 25. (continued)

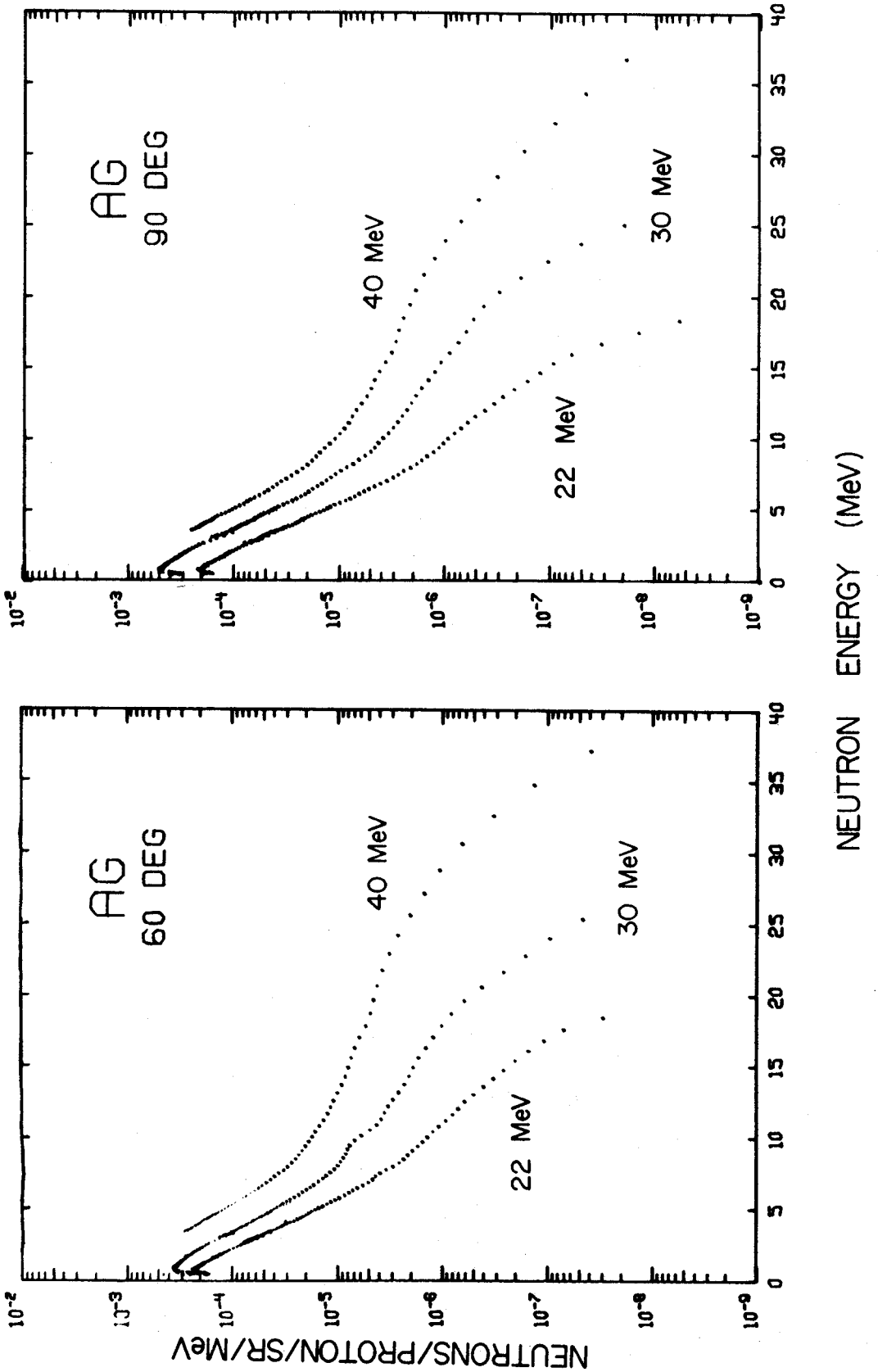

Figure 25. (continued)

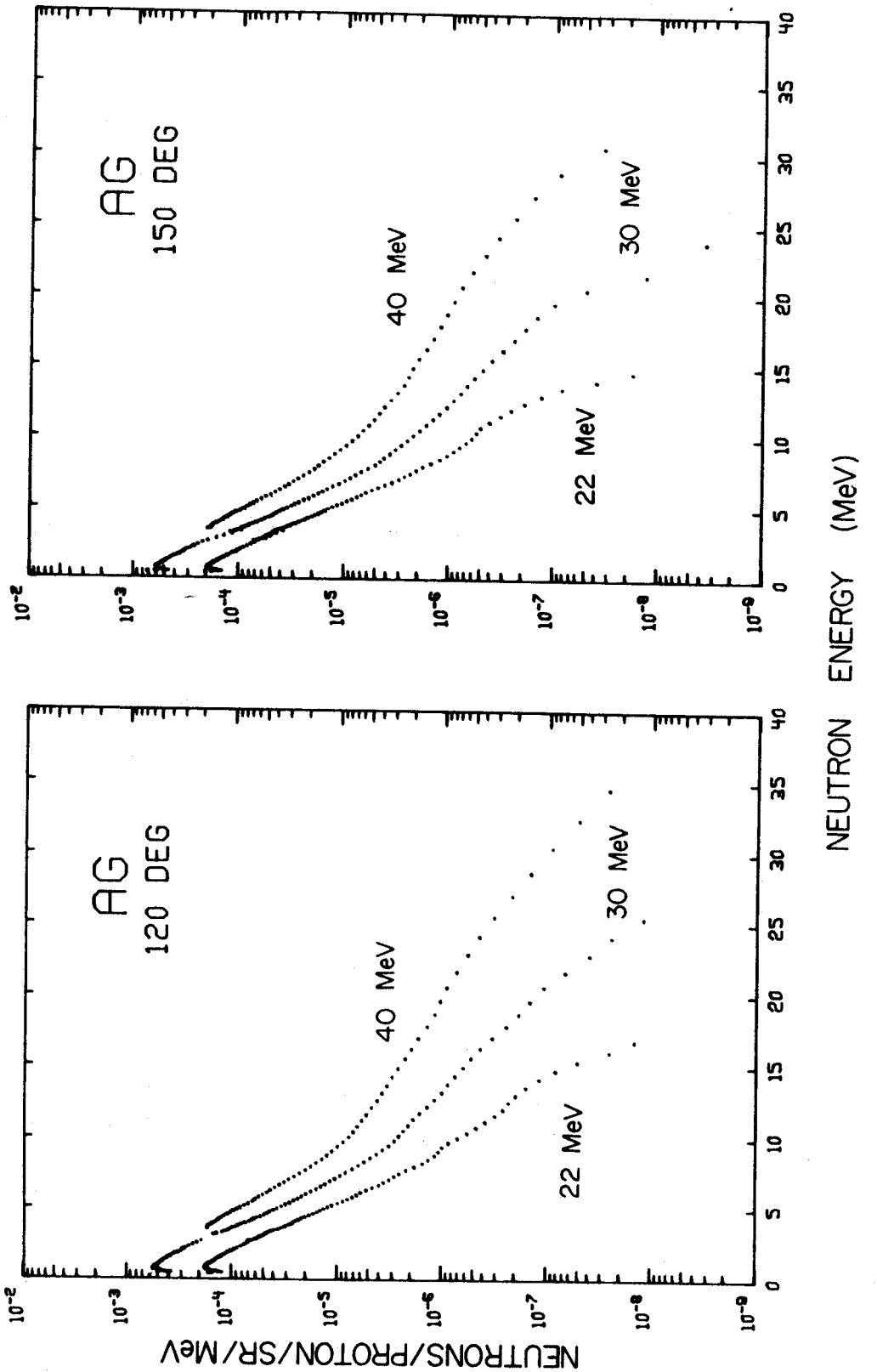

Figure 25. (continued)

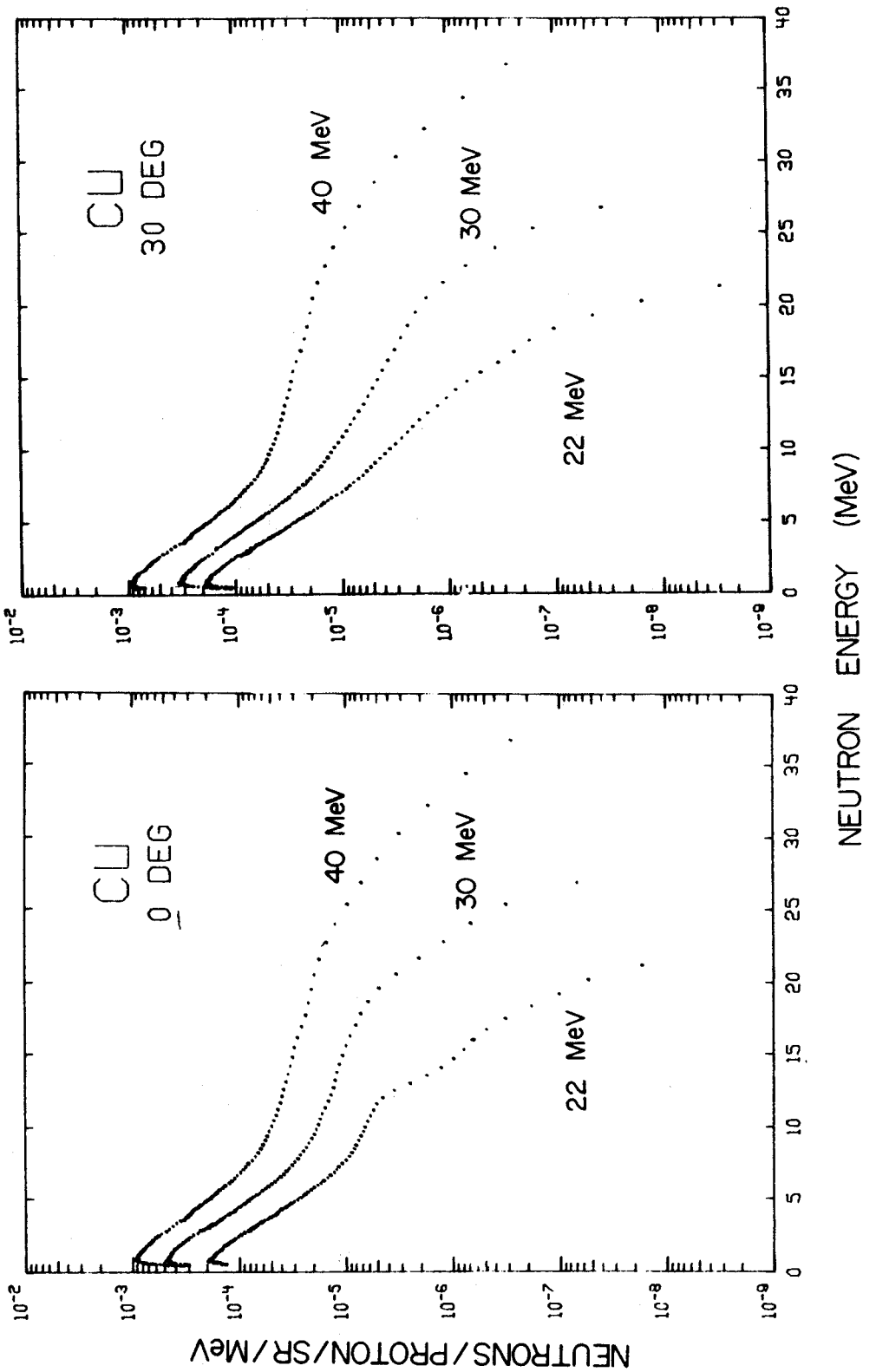

Figure 25. (continued)

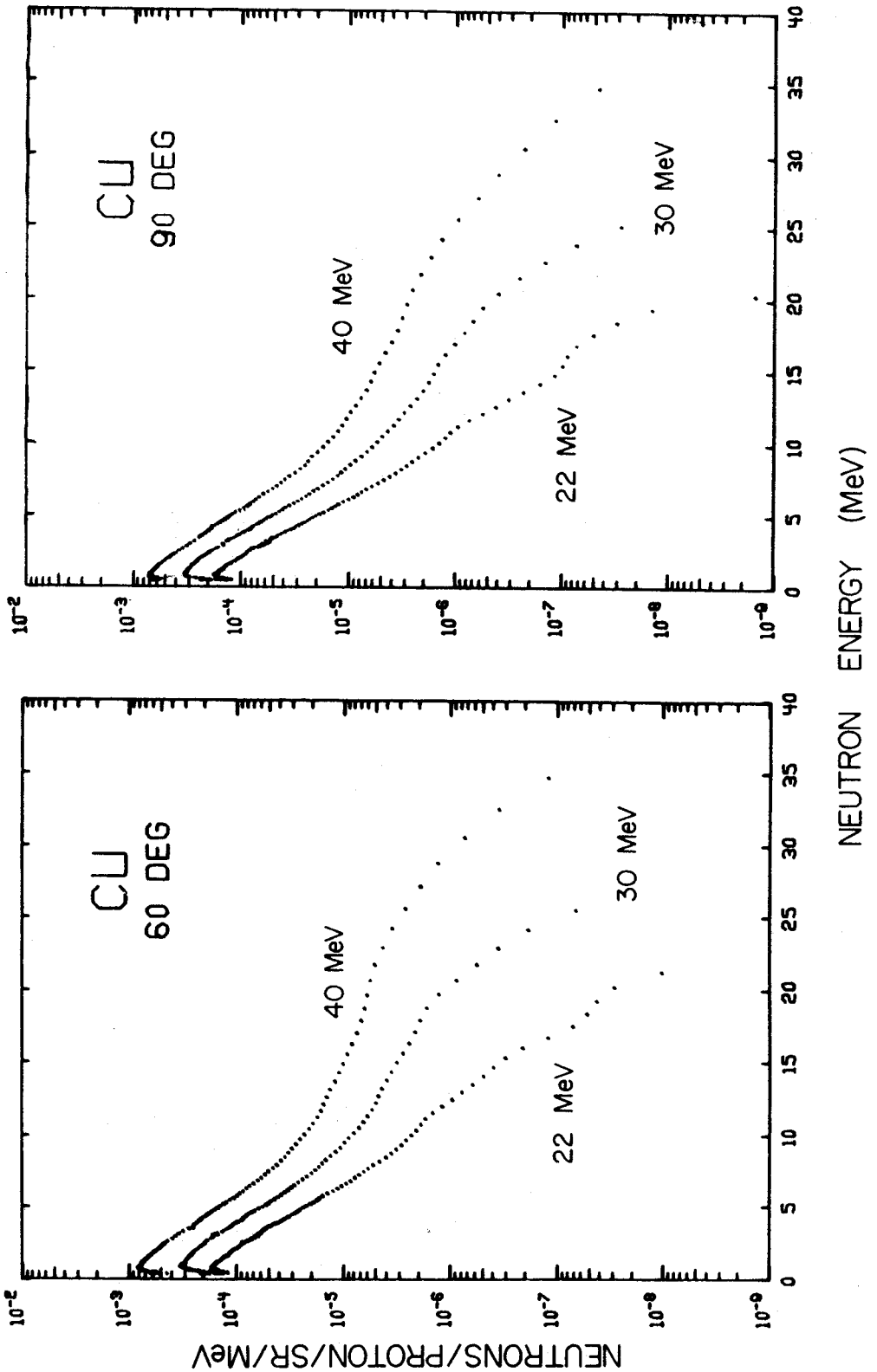

Figure 25. (continued)

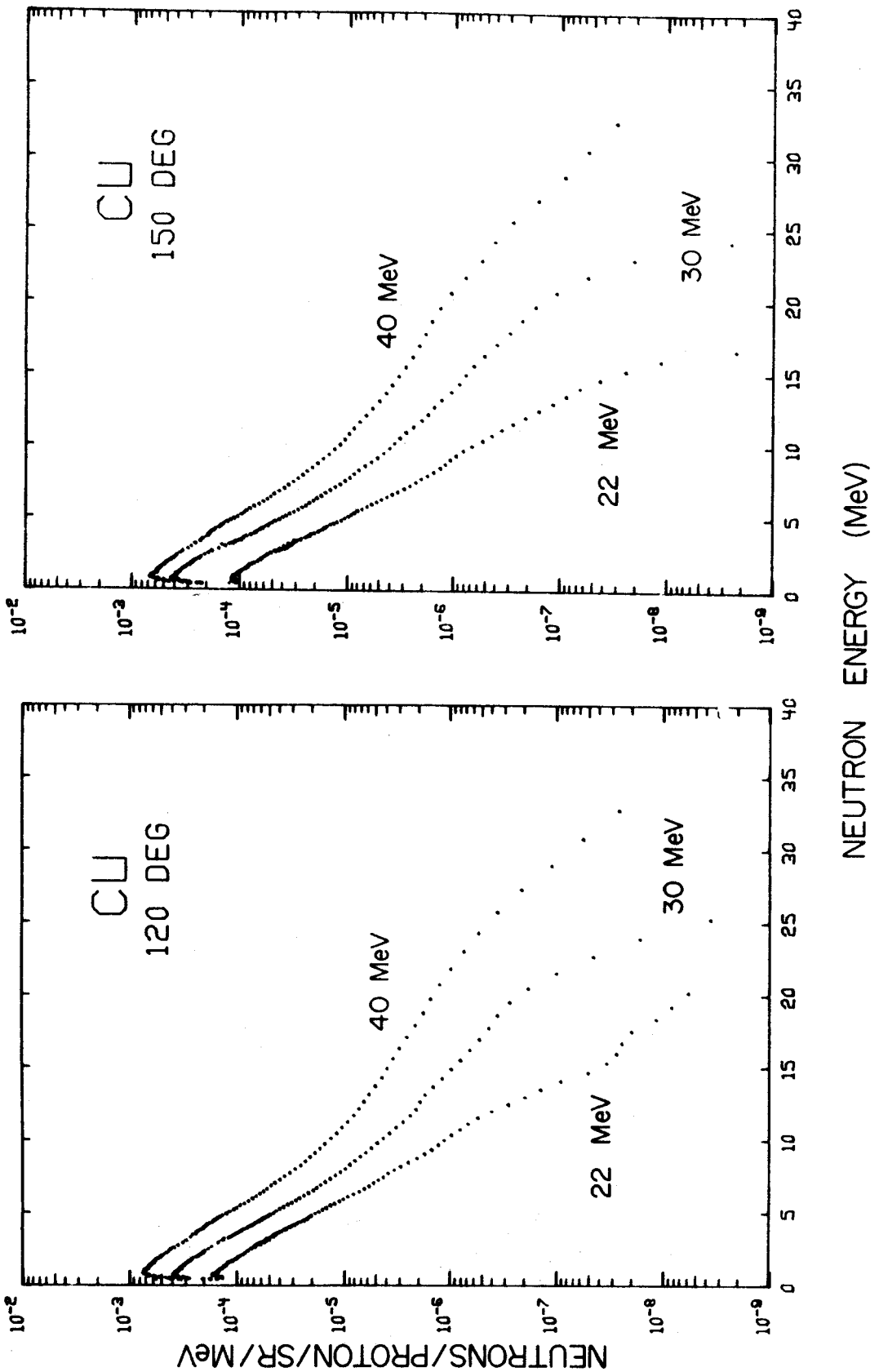

Figure 25. (continued)

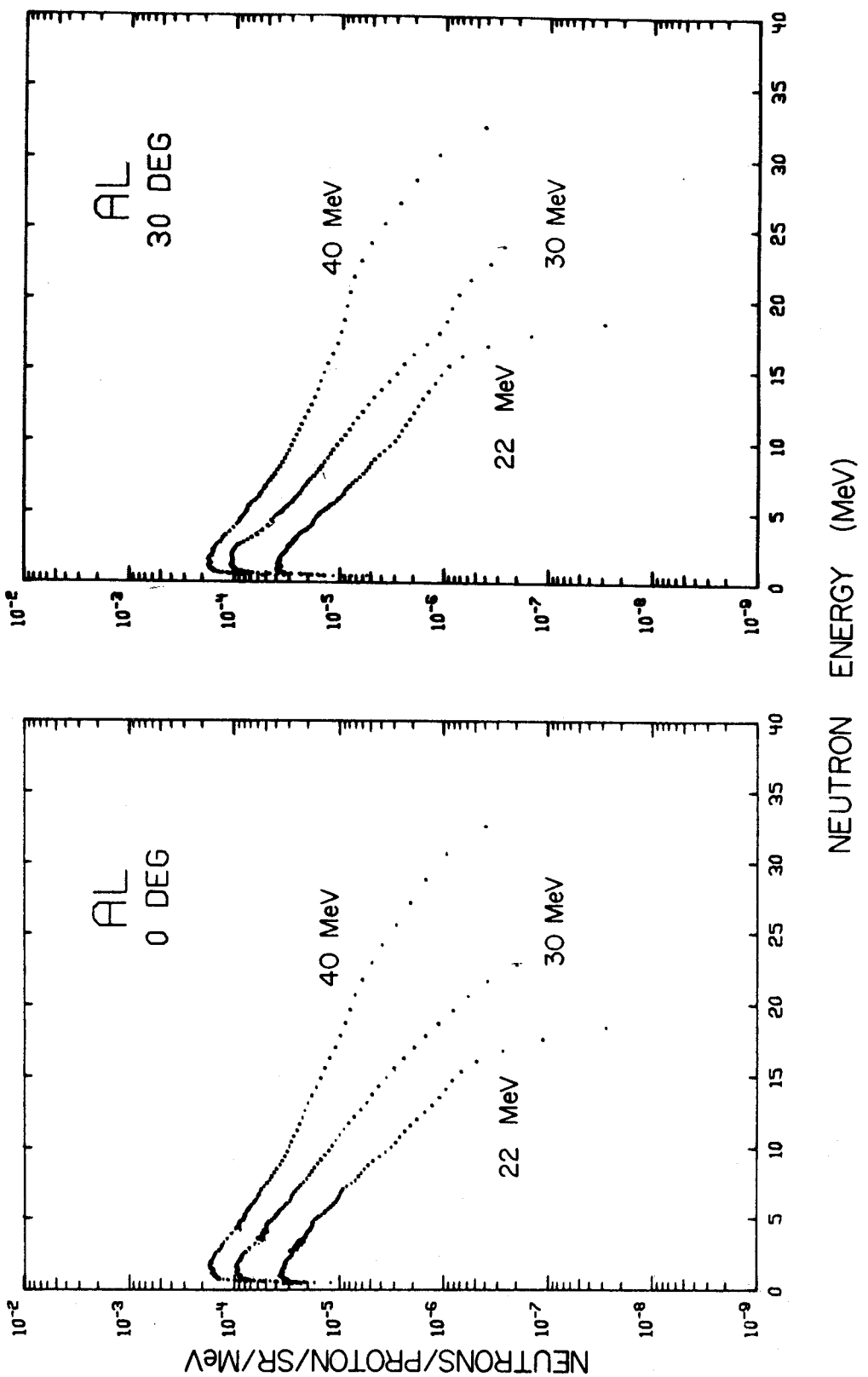

Figure 25. (continued)

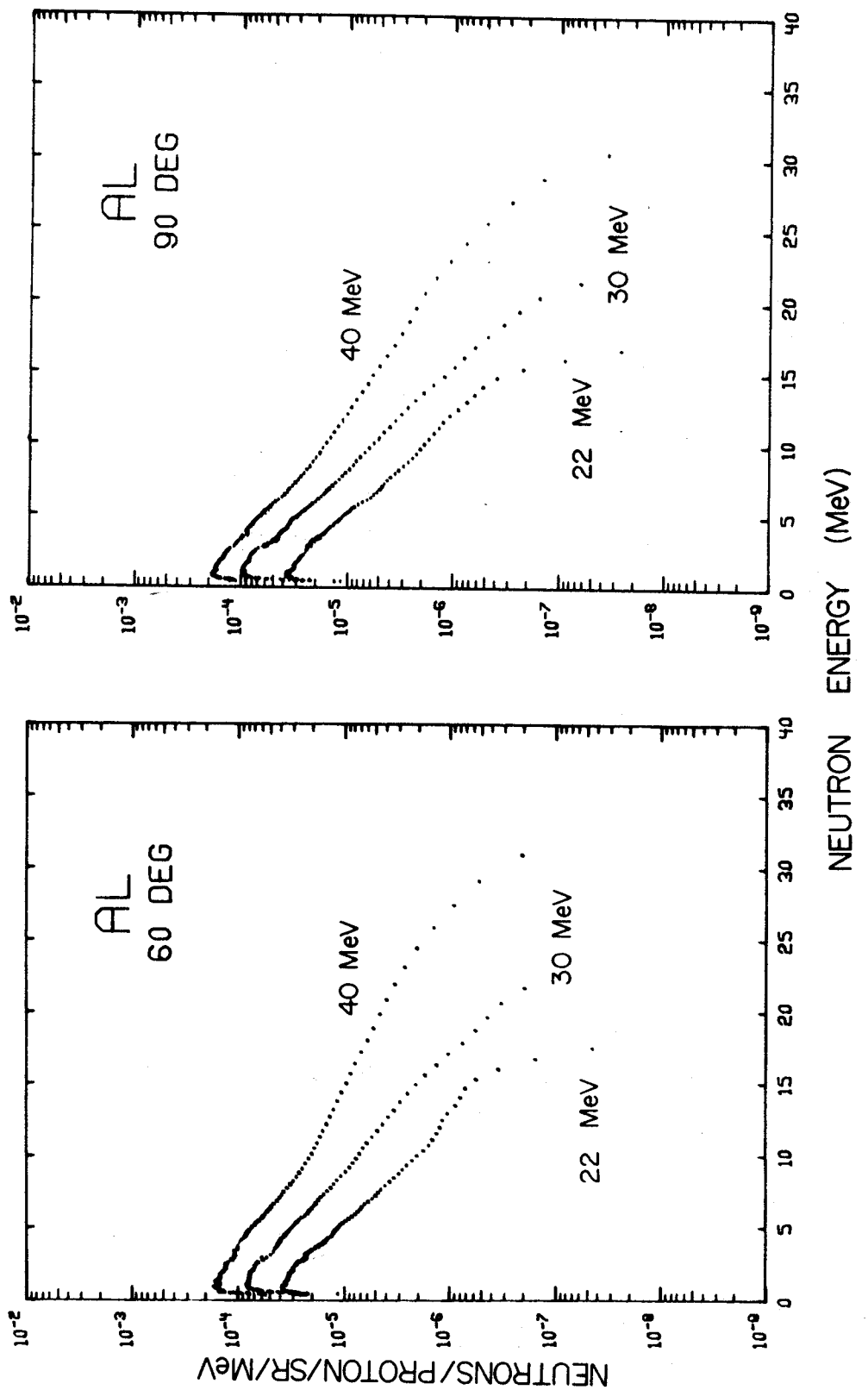

Figure 25. (continued)

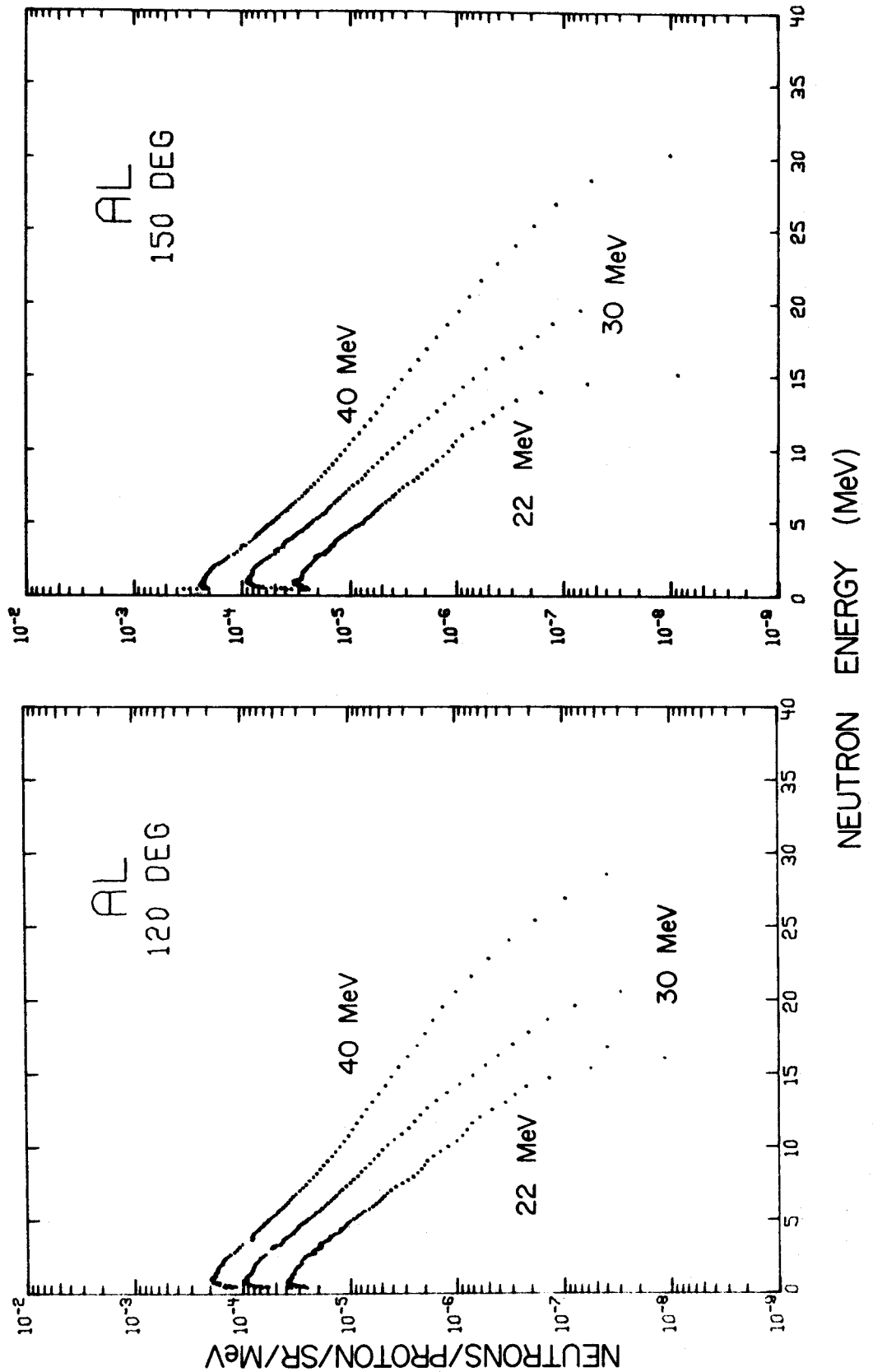

Figure 25. (continued)

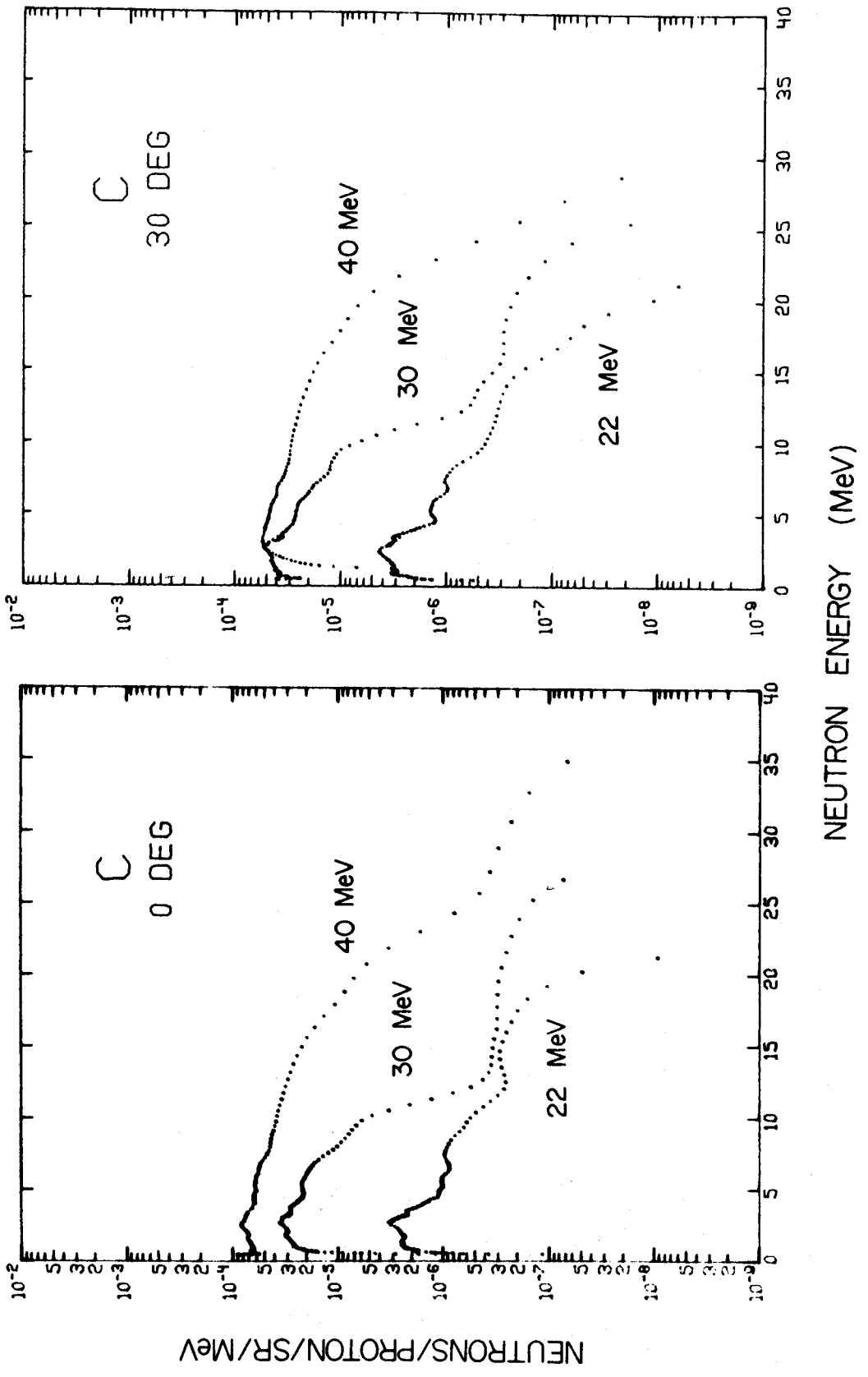

Figure 25. (continued)

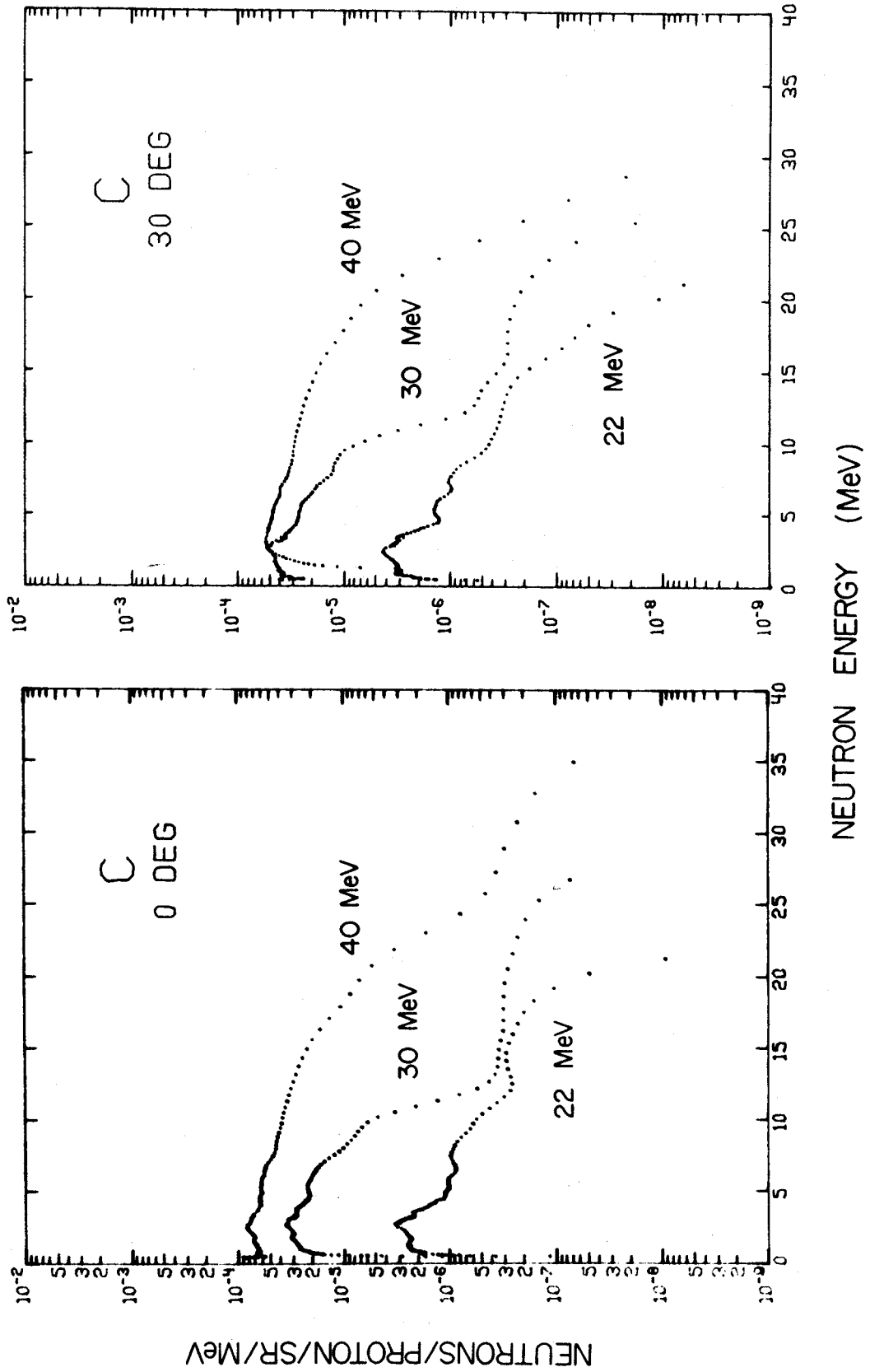

Figure 25. (continued)

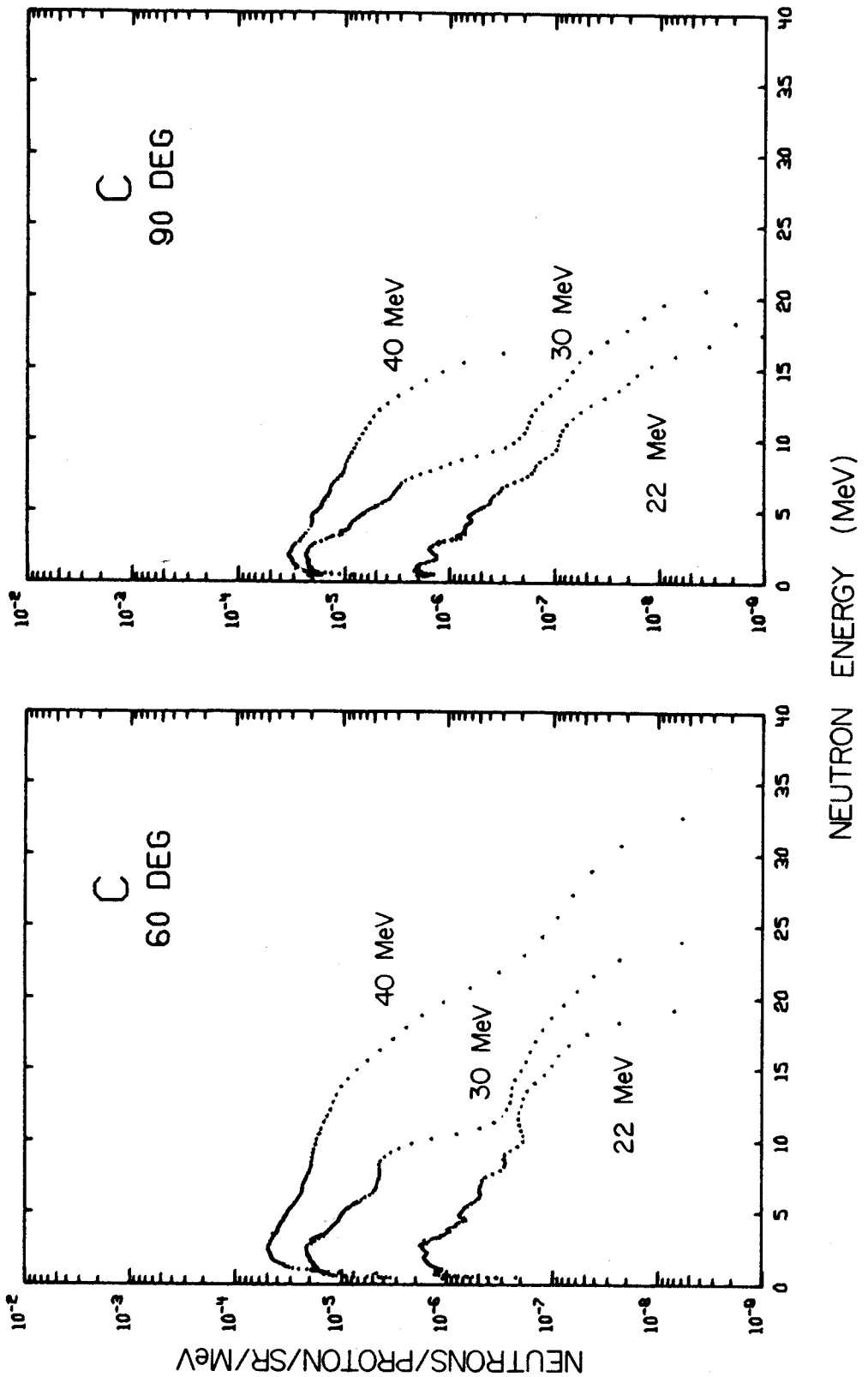

Figure 25. (continued)

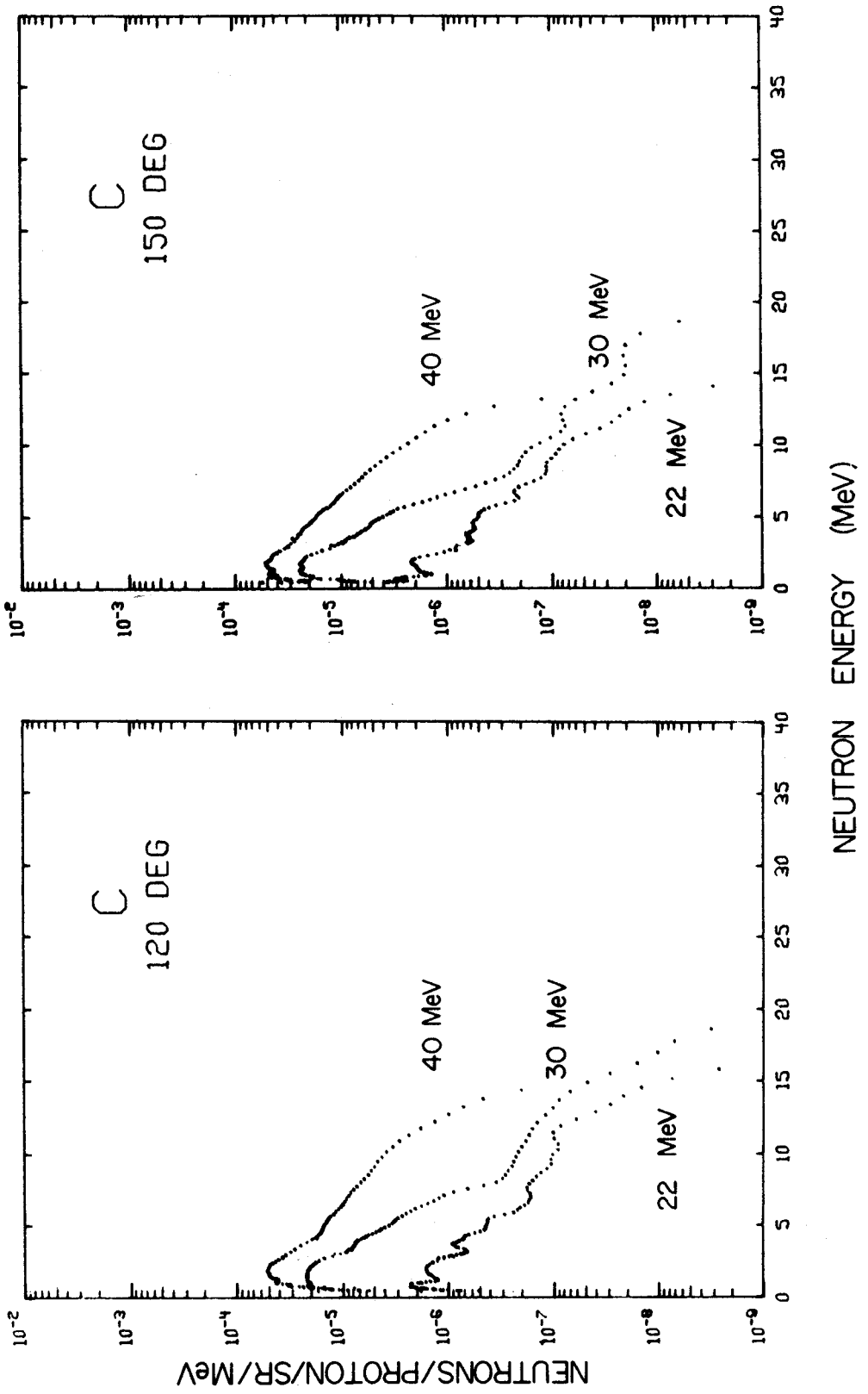

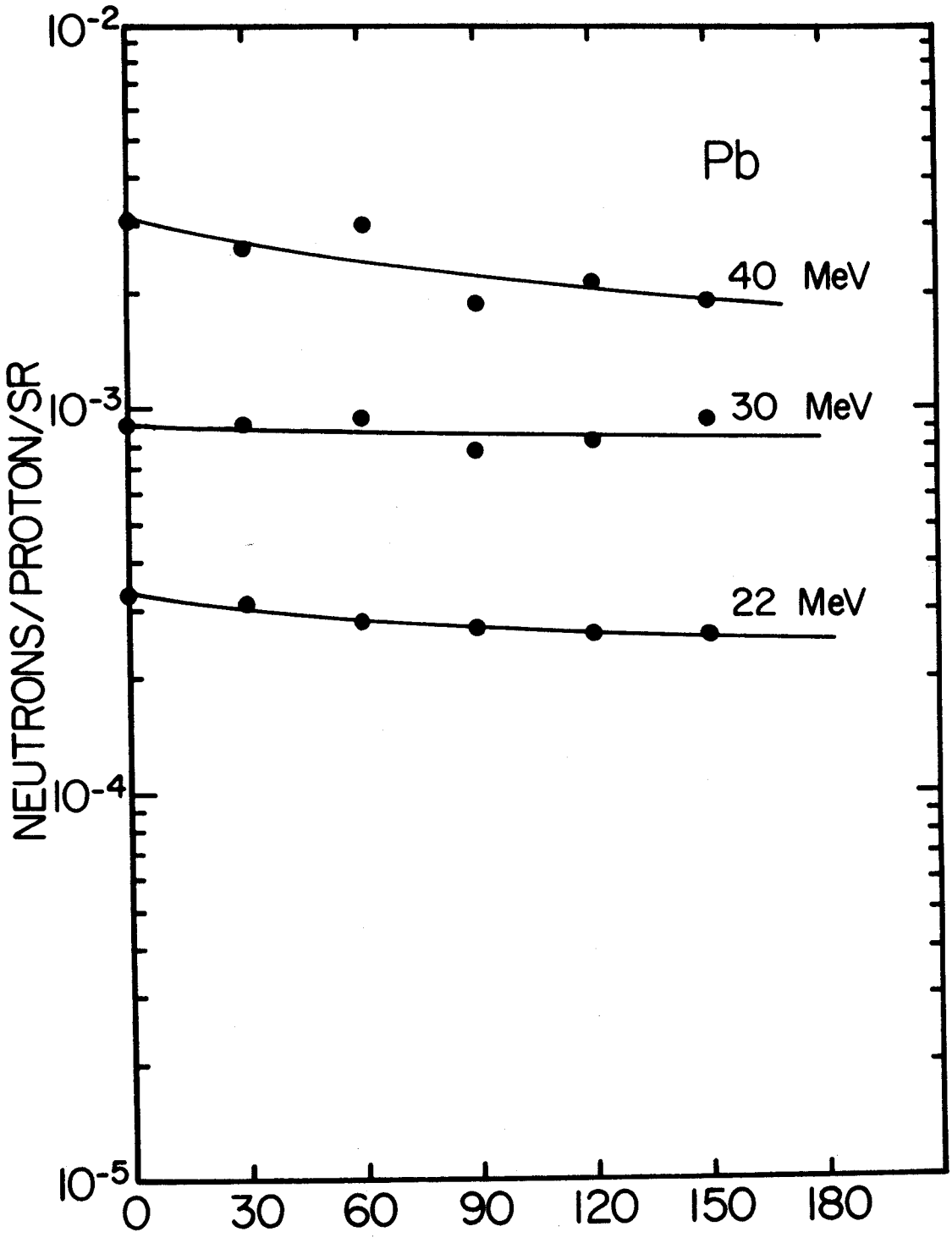

Figure 26. Neutron Angular Distributions

Figure 26. (continued)

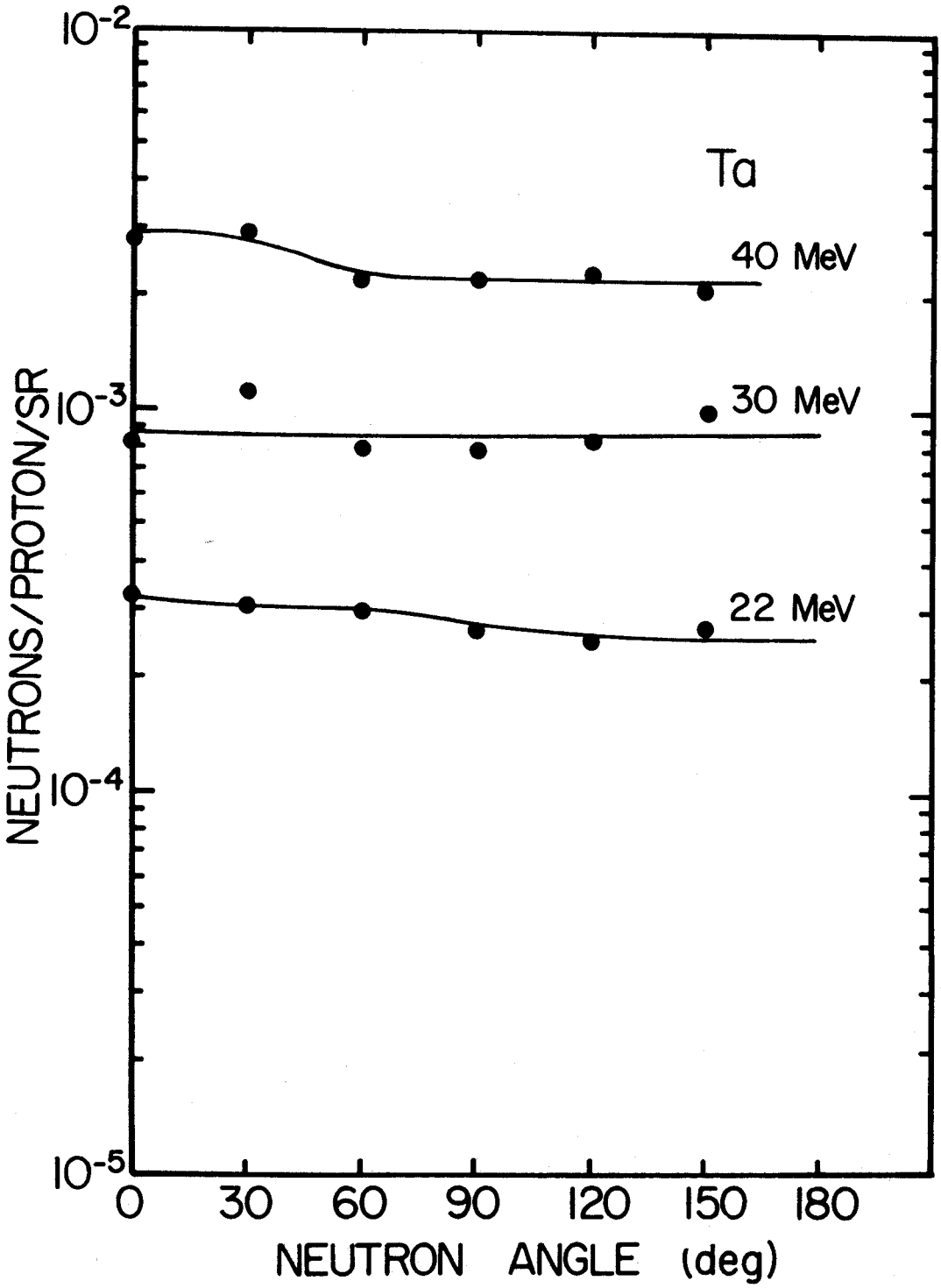

Figure 26. (continued)

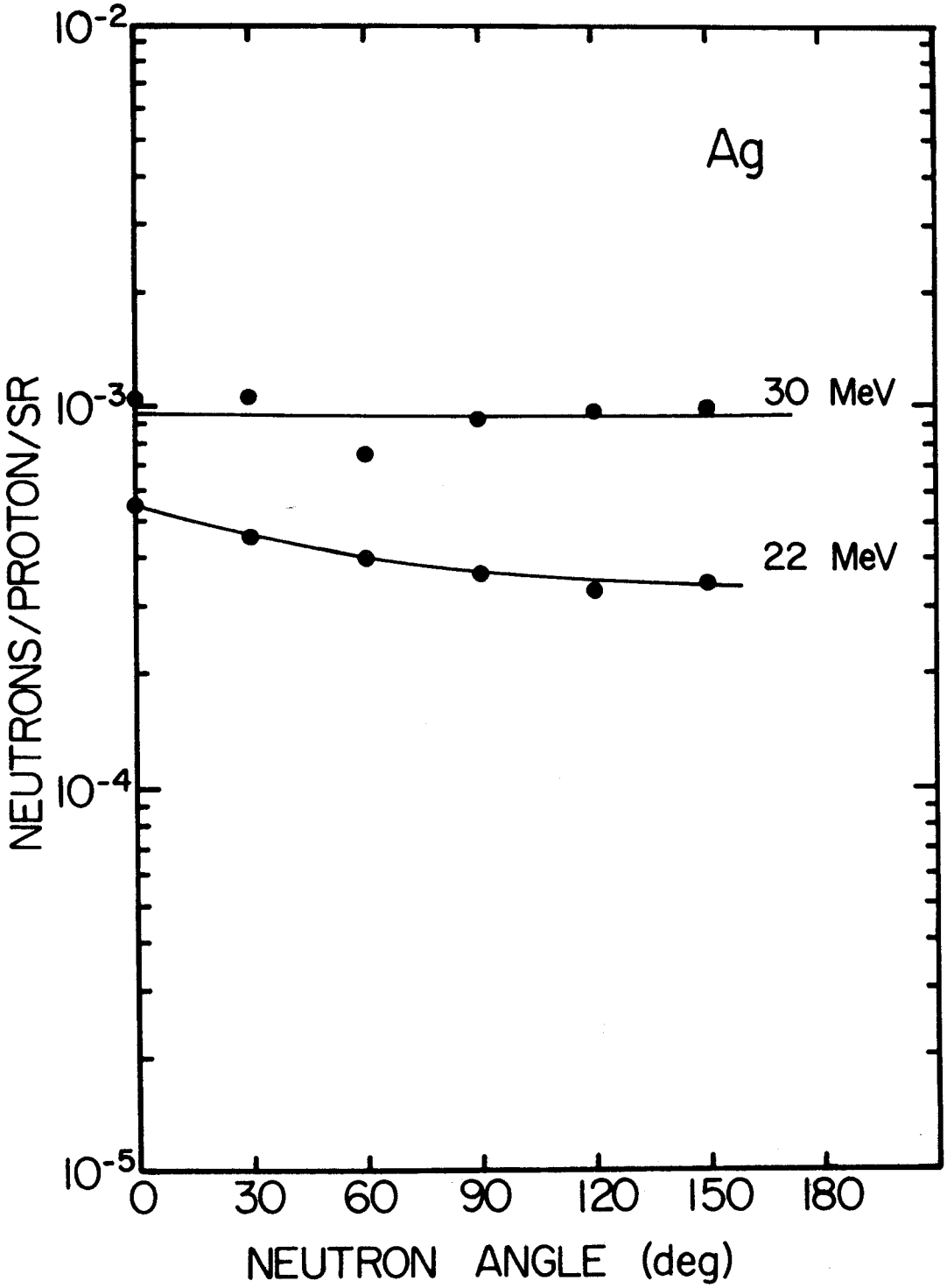

Figure 26. (continued)

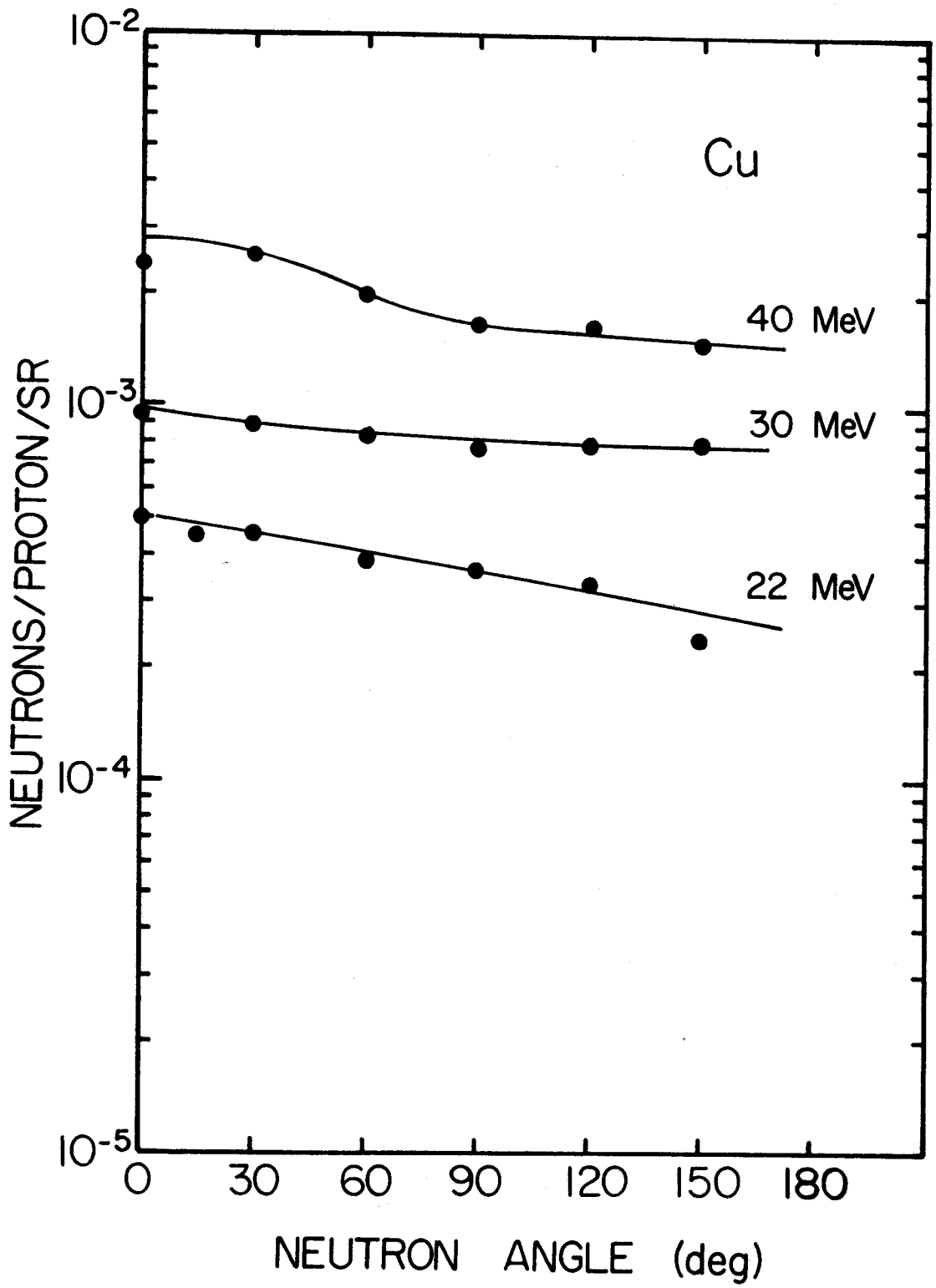

Figure 26. (continued)

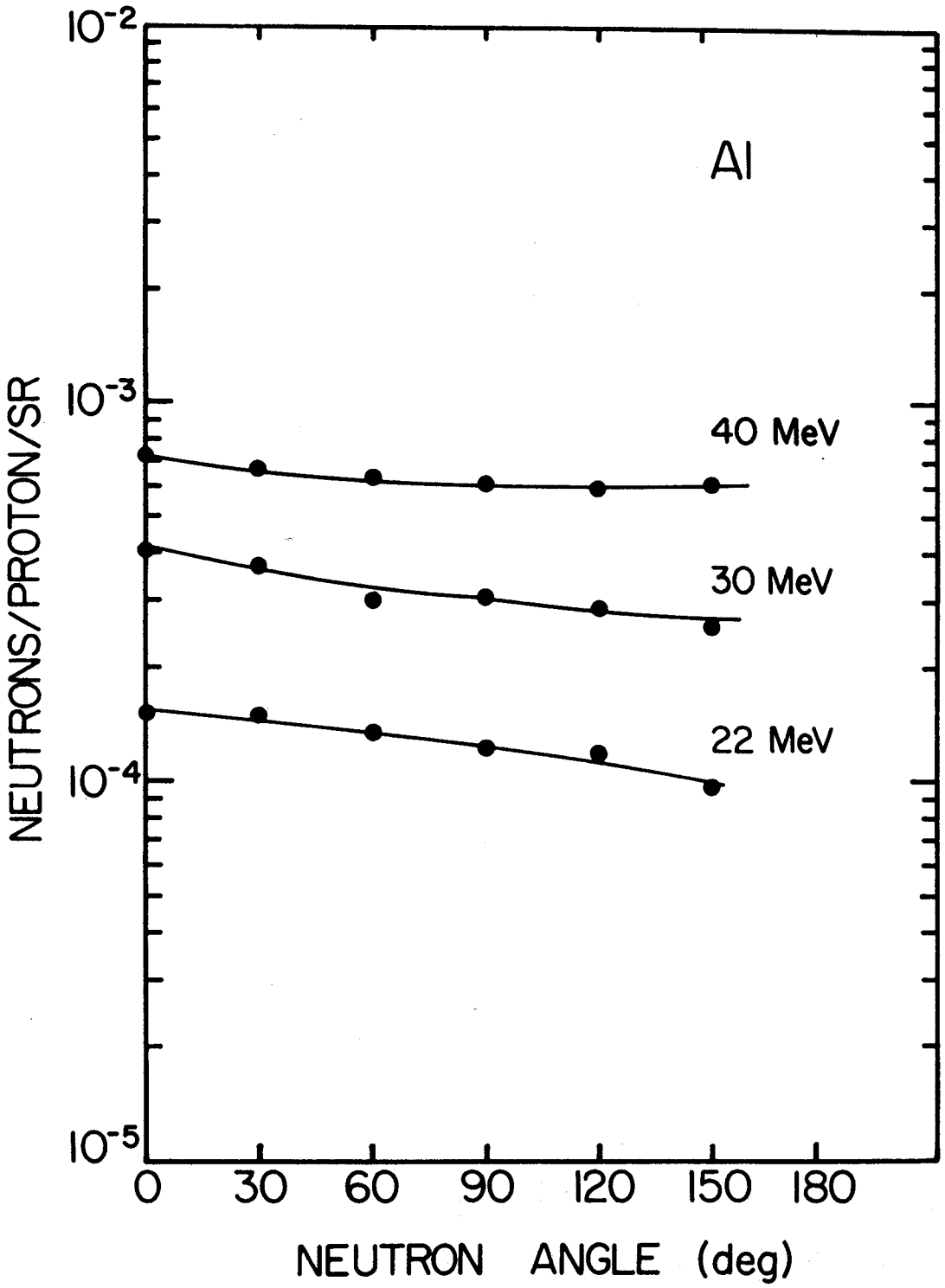

Figure 26. (continued)

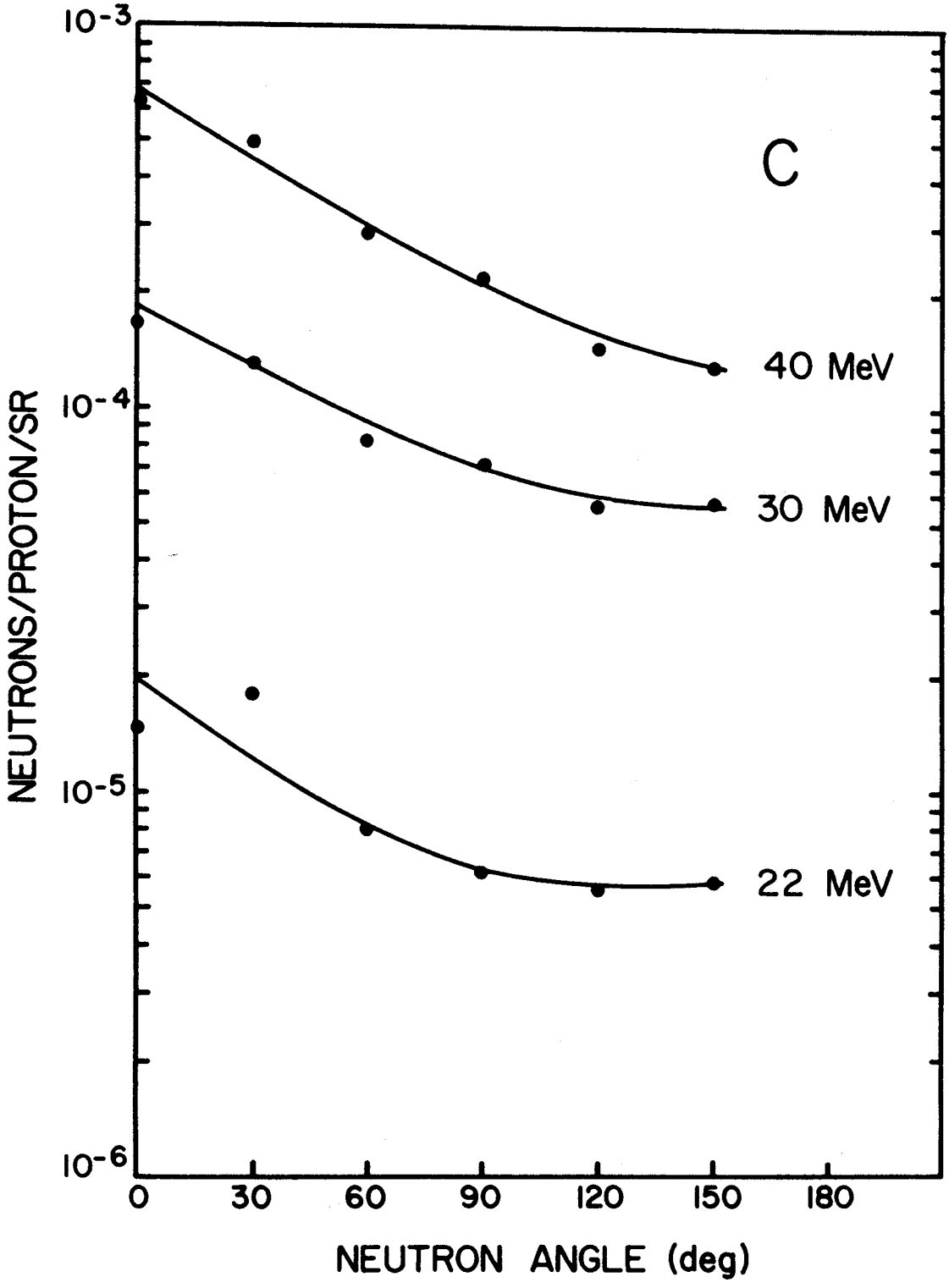

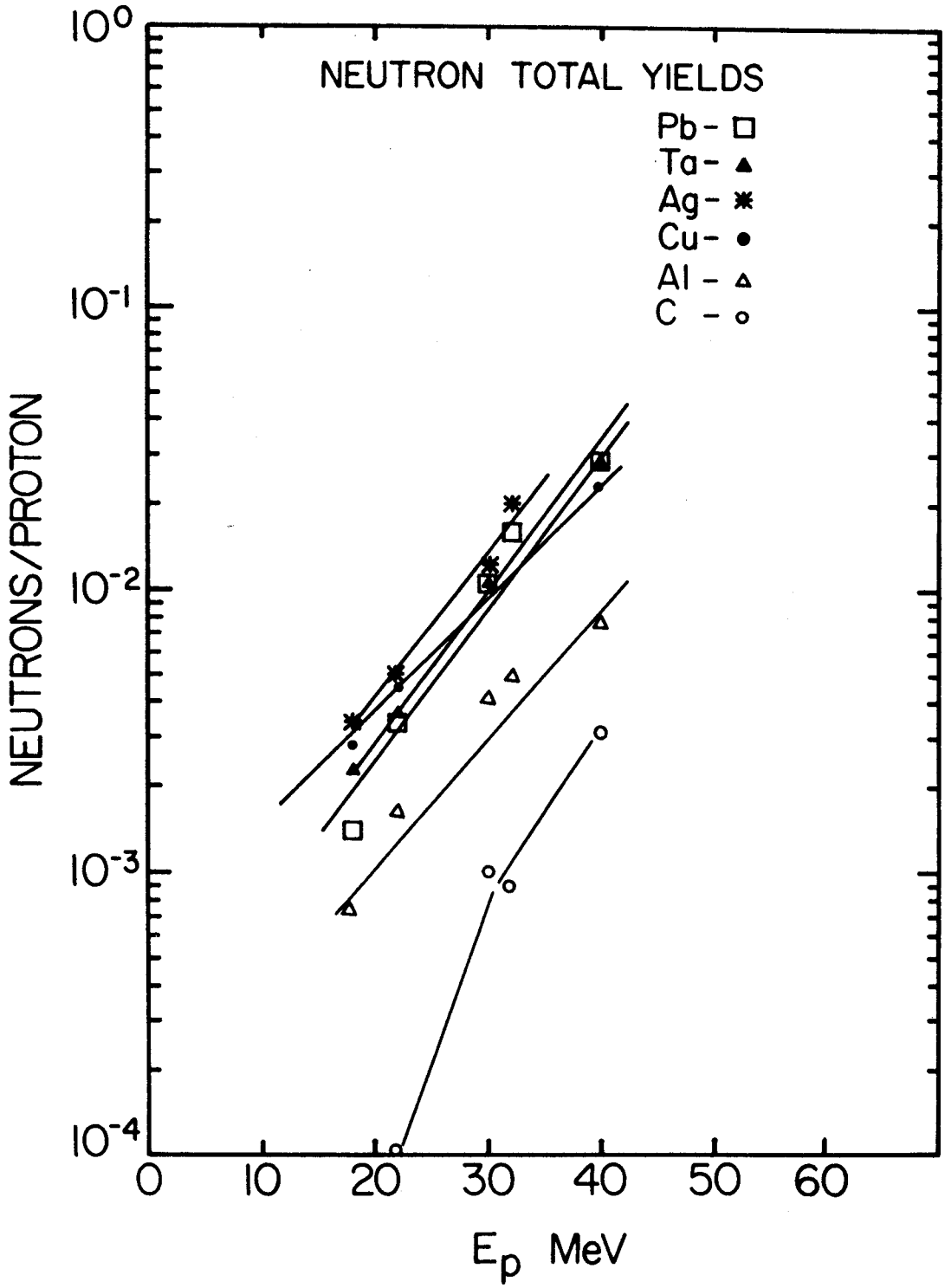

Figure 27. Neutron Total Yields. The 18 and 32 MeV data were taken from reference Ta 57.

both the absolute magnitude of the total yields and the behavior of these yields as a function of bombarding energy.

I. Estimate of Experimental Uncertainties

One of the principle sources of uncertainty in the experimental results is the uncertainty in the calculation of the neutron detection efficiency of the scintillator. The error in the calculation has been estimated (Ku 64) to be about $\pm$ 10%. This estimate was based upon the known errors in the measured neutron cross sections used in the calculation. The calculation has been investigated experimentally by several groups (We 62, Ga 61, Hu 70) and found to be accurate to within the experimental errors, which are typically about $\pm$ 15%. This latter value, $\pm$ 15%, was taken to be the error in the calculated efficiencies.

Possible errors in the normalization of the data due to faulty charge integration were noted previously. The energy spectra of the low-energy neutrons (0.5 - 3.5 MeV) were compared carefully with the corresponding spectra of the higher energy neutrons, and examined for agreement in both slope and magnitude in the region where they overlapped. Except for minor effects due to finite pulse height resolution at threshold, the "low" and "high" energy data agreed very well in slope. In cases where the magnitudes of two spectra differed in the region of overlap, the low energy spectra were scaled to match the high energy spectra. Only for a few spectra were the scaling factors different from unity by more than 15%.

In addition, the total gamma-ray yields from each target (in counts/μcoul), which should be isotropic, were examined for deviations from isotropy as an indication of faulty charge integration. For cases in which the high- and low-energy neutron yields did not agree in magnitude, the gamma yields for the low energy runs differed from isotropy by roughly the same amount as the neutron yields, 15%, so this was taken to be indicative of the error in the data due to faulty charge integration.

In any case, such adjustment of the normalization of the low energy data as described above is justifiable only if the results agree well with previous experimental data, as in Figure 27, and if analysis of the data yields reasonable values of extracted parameter r_o, as discussed in section V.

Except at detection threshold and the very highest neutron energies, where statistics are poor, the statistical error in the data is typically $\pm$ 4%.

So the data are estimated to be good to about $\pm$ 20%. The fractional non-compound yields as obtained in the next section depend only upon the uncertainty in the efficiency calculation and certain assumptions made in their derivation, which will be discussed in section V, also.

V. DATA ANALYSIS

A. Extraction of Nuclear Level Density and Radius Parameters

Perhaps the most distinguishing feature of the heavy (A > 60) element neutron energy spectra shown in Figure 25 is that each has two distinct components. The spectral shape of the low energy (< 7 MeV) neutrons, which have left their residual nuclei with relatively high excitation energies, is characteristic of an "evaporation" spectrum as predicted by the statistical fermi-gas model of the compound nucleus. The energy spectrum of neutrons with energies greater than 6 or 7 MeV, on the other hand, cannot be explained by such a model, and will be discussed in the next section.

The statistical fermi-gas model of the nucleus as developed and applied in sections II and III was used to analyze the evaporation portions of the neutron energy spectra in an attempt to determine the nuclear level density parameter a, and nuclear radius paramenter r_o. a chiefly affects the shape and slope of the evaporation neutron energy spectrum, while r_o affects its normalization.

All the spectra for a given target at a given bombarding energy were plotted on the same graph. The previously described program DECAY was run with a number of values for a and r_o, and the results of the calculations were plotted on the same graph for comparison with the data. A typical plot is shown in Figure 28 for the case of Ta at 40 MeV. The value of a which was considered to give the best fit to the data was $a = A/10\ MeV^{-1}$. The other two

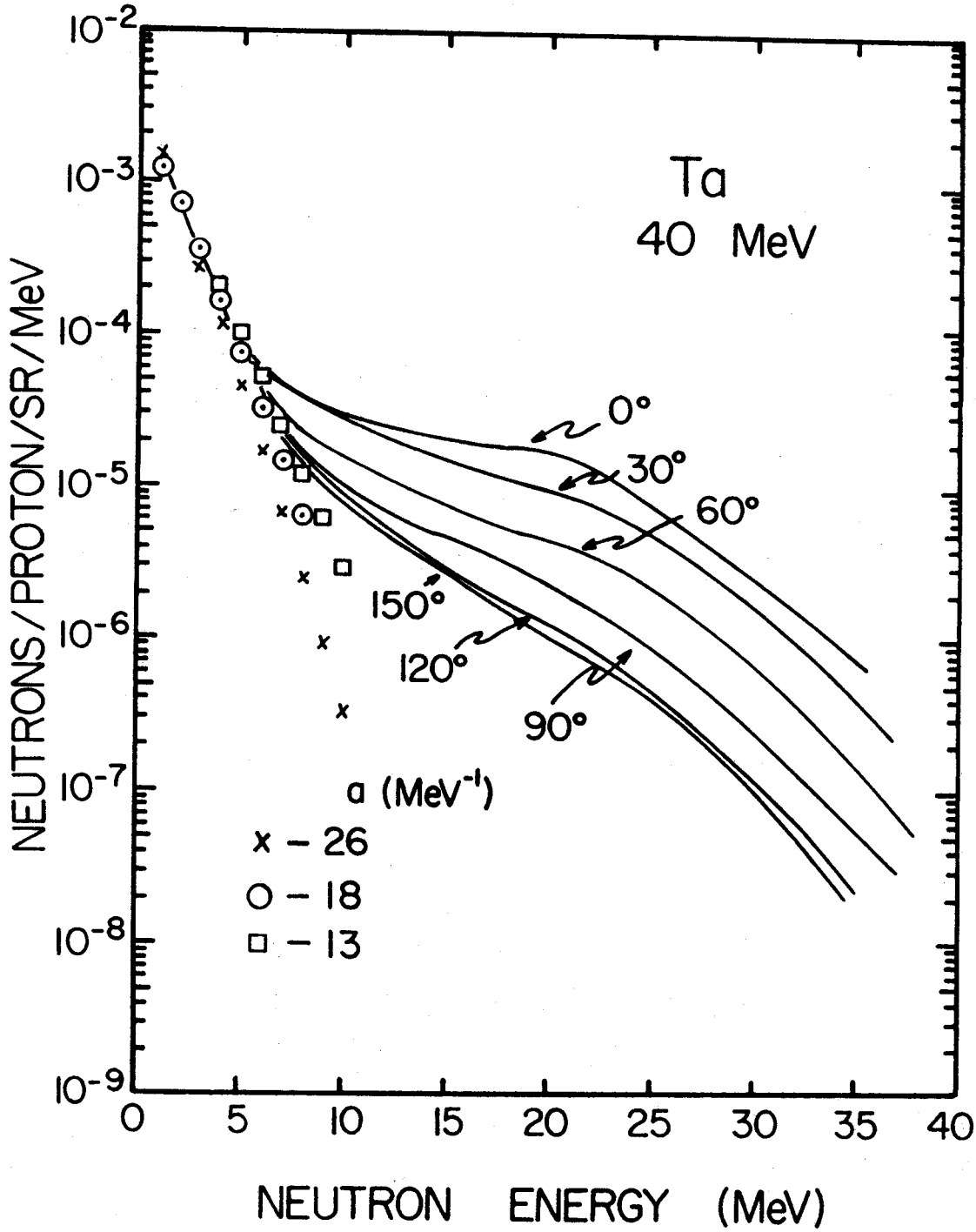

Figure 28. Comparison Between Evaporation Theory and Experimental Data. The Solid Curves Represent the Data.

sets of points correspond to the a values as indicated, which were considered just barely unacceptable; these values of a were considered to be indicative of the errors involved in using the model and in choosing the "best" fit. The targets thus analyzed were Cu, Ag, Ta, and Pb.

All fits to the data were chosen by eye. In view of the integral nature of the data and the simple assumptions employed in the calculations it was not deemed appropriate to employ χ^2-type fitting techniques.

Figure 29 shows the results of this method of analysis of the data; the error bars shown were determined by the method described above. The upper line plotted in this graph corresponds to a = A/11 MeV^{-1}, which is obtained from the form of the model developed by Lang and LeCouteur (La 54). This model considers explicitly the competition between neutron and proton emission, and for this reason is more relevant to this experiment than some older models, which did not consider proton emission at all.

In any case, the level density parameters obtained are in excellent qualitative agreement with both the simple and modified forms of the theory, and in reasonably good quantitative agreement with previous experimental values (Bo 62).

The experimental values of a determined here for Pb reproduce -- at least at 22 and 30 MeV -- a previously observed (Bo 62) and predicted (Ne 56) decrease in the level density attributed to shell closure (or near shell closure) in the Pb isotopes.

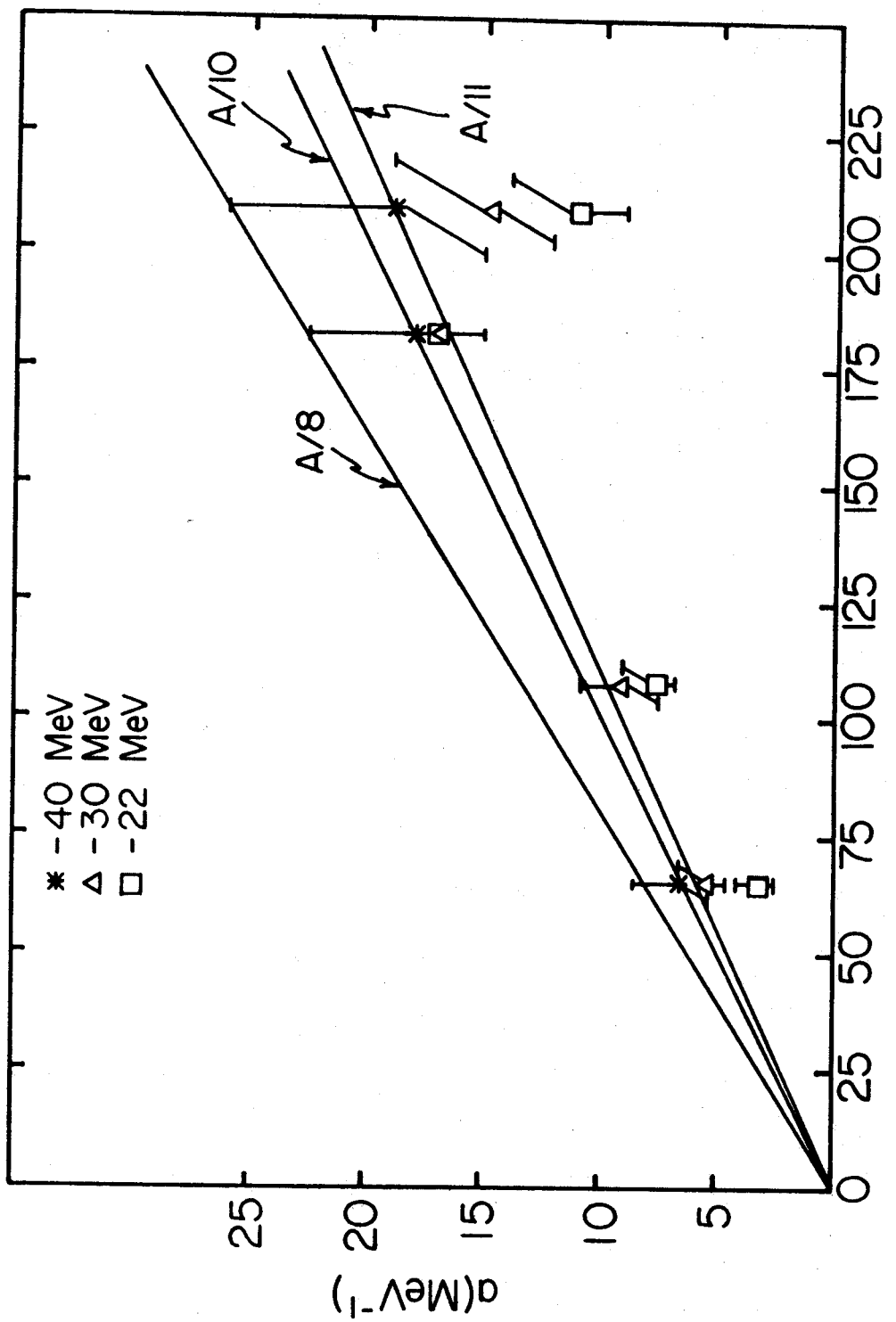

Figure 29. Extracted Nuclear Level Density Parameters as a Function of Mass Number

An apparent dependence of a upon bombarding energy is also indicated in the case of Pb. Such effects have been noted by other investigators (Wo 65, Si 62, Al 64) using other incident particles, lower bombarding energies, and other targets, so it is perhaps not too surprising to see it in some of the cases considered here. Such an effect, however, disagrees with the basic assumptions of the model, unless one offers as a possible explanation that the shell effects in lead, which are prominent at low bombarding and excitation energies and do not conflict with the model, decrease in importance as the excitation energy increases. In any case, the errors made here in extracting the values of a from the data do not allow such a statement to be made definitively without further experimental corroboration.

Similar statements might also be made about Cu, which is one proton removed from the Z = 28 closed proton shell, but, again, such conclusions should await further more detailed experimental results.

The values of r_o which gave the correct normalization for each target are shown plotted in Figure 30. The value of r_o for the heavy targets is 1.2f. This value is somewhat low compared to values generally used for r_o (1.3 - 1.6f) (Ta 58, Ha 62) in this sort of calculation. However this is consistent with the assumption that all of the flux lost from the incident beam goes into formation of compound nuclei which may subsequently decay only by neutron or proton emission. This assumption was necessitated by the unavailability of detailed information regarding the contributions of

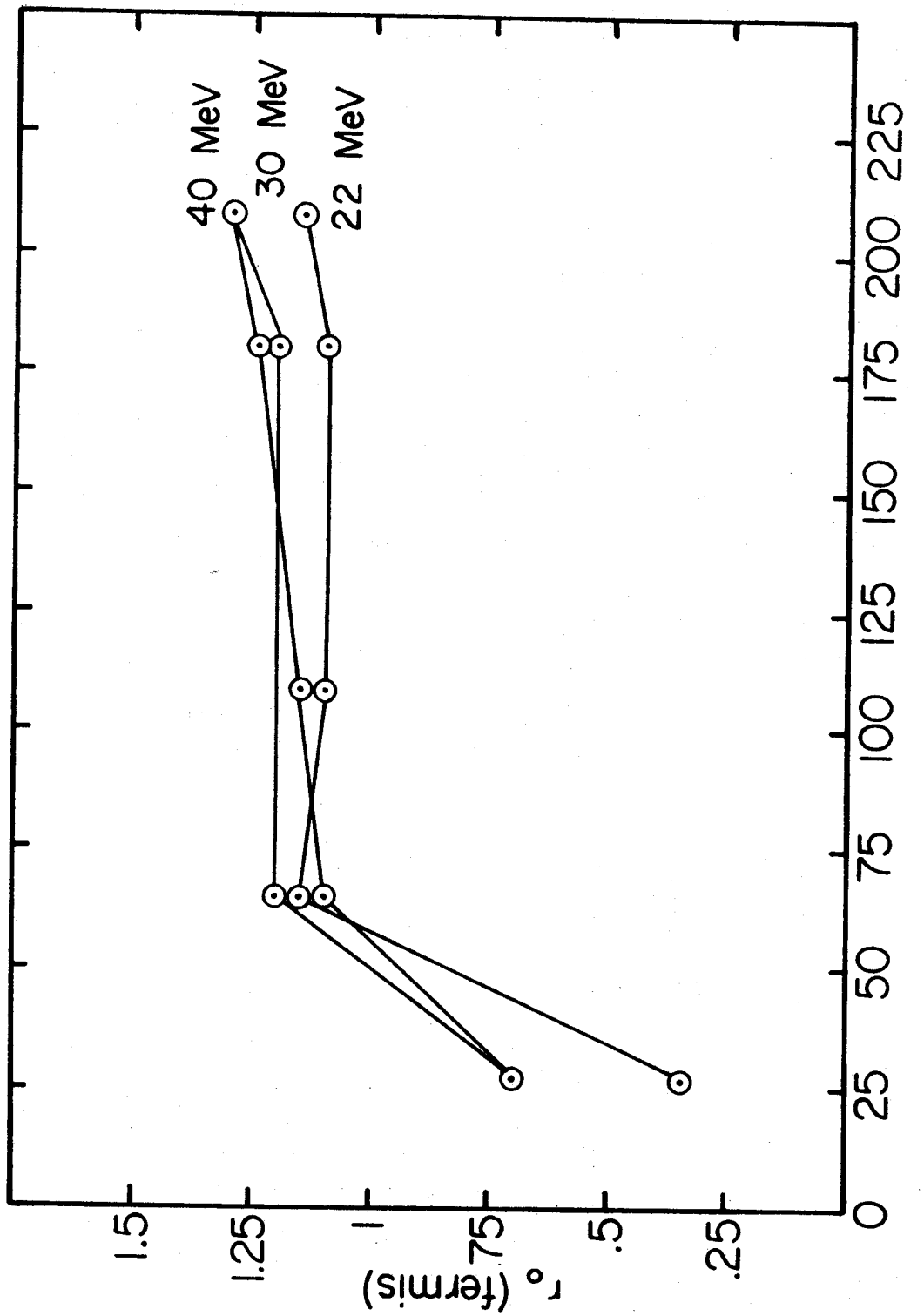

Figure 30. Extracted Nuclear Radius Parameters as a Function of Mass Number

all types of reactions and reaction mechanisms to total reaction cross sections. In fact it is hoped that this experiment may yield some information in this regard. While neutron evaporation was predominant in this experiment, other reaction mechanisms certainly can and do contribute to the total reaction cross sections at the bombarding energies used, so that the above assumption would lead to a somewhat smaller value of r_o than if these reactions were accounted for explicitly. A somewhat different approach will be employed in the next section to analyze the behavior of one of these other types of reactions.

One case where the assumptions of the model are not valid is that of Al at all bombarding energies used. The neutron energy spectra from this element do not have the shape characteristic of neutron evaporation, so one might suspect a breakdown of the model, and that suspicion is readily confirmed when analysis of these data is attempted in a manner similar to that employed for the heavier elements. As shown in Figure 30, the values obtained for r_o in this case are quite small compared to the values obtained for the other elements, which very likely indicates significant competition from other reactions and reaction mechanisms. In fact evaporation of protons, alphas and even heavier particles is much more likely in this situation than for the heavier elements, because the Coulomb barrier is not high enough to inhibit them very strongly. Furthermore, no suitable fit could be made to these energy spectra in order to obtain a value for the level density parameter.

None of this is unexpected, since Al is a light nucleus, and the lower limit for the validity of the statistical fermi-gas model is around A = 40 to A = 50 (Mo 53).

Carbon is a similar case. The statistical fermi-gas model is certainly not applicable to such a light nucleus, and from the shapes of the neutron energy spectra themselves, it is evident that the treatment which gave very good results for the heavy elements would give no meaningful results for carbon; thus, no attempt was made to analyze the carbon data in this fashion.

B. Extraction of Neutron Yields from Non-Compound Processes

The relatively flat neutron energy spectra extending to very high neutron energies (see Figure 25) cannot be explained by the simple statistical theory used in section VA. Such spectral shapes are not characteristic of neutron evaporation from a highly excited compound nucleus, and have been observed in (p,n) reactions (Gr 71, Ve 69) and (p,p') reactions (Ra 71). They have been interpreted by some authors (Gr 66, Cl 71, Bl 72) as evidence of a process involving the emission of particles from the compound nucleus during the equilibration period while the incident energy is being distributed among all the nucleons. This pre-equilibrium statistical model of nuclear reactions as developed by the above authors is derived from detailed consideration of the reaction mechanism. The model is based upon a stepwise sequence of nucleon-nucleon interactions inside the nucleus which tend to create ever more complicated many-particle-many-hole configurations.

In this way, the incident energy is eventually distributed among all the nucleons, and statistical equilibrium is finally reached. Pre-equilibrium emission occurs because at each stage in the sequence, particularly the beginning stages, there is a reasonable probability that a nucleon will be emitted into the continuum rather than undergo a subsequent collision with another nucleon.

Therefore, it was decided to extract the non-compound contribution to the total neutron yield in another manner which relies basically upon certain features of the data. Differential neutron energy spectra were obtained for each target at each angle by subtracting a thick target spectrum from the corresponding spectrum at the next highest bombarding energy; the only two such subtractions possible with three bombarding energies were to subtract the 22 MeV data from the 30 MeV data, and the 30 MeV data from the 40 MeV data. Then the evaporation spectrum was extrapolated to higher energies as shown in Figure 31, and subtracted from the experimental curve. These latter differences are then interpreted as the non-compound parts of the spectrum, as indicated in the figure. Above roughly 7 MeV the evaporation spectra are largely insignificant, and the values of the non-compound spectrum are equal to the experimental data points.

This type of analysis was applied only to Cu, Ag, Ta, and Pb. In the case of Al, no satisfactory distinction could be made between evaporation and non-compound spectra, and C cannot be discussed in any terms meaningful to either of the models under consideration.

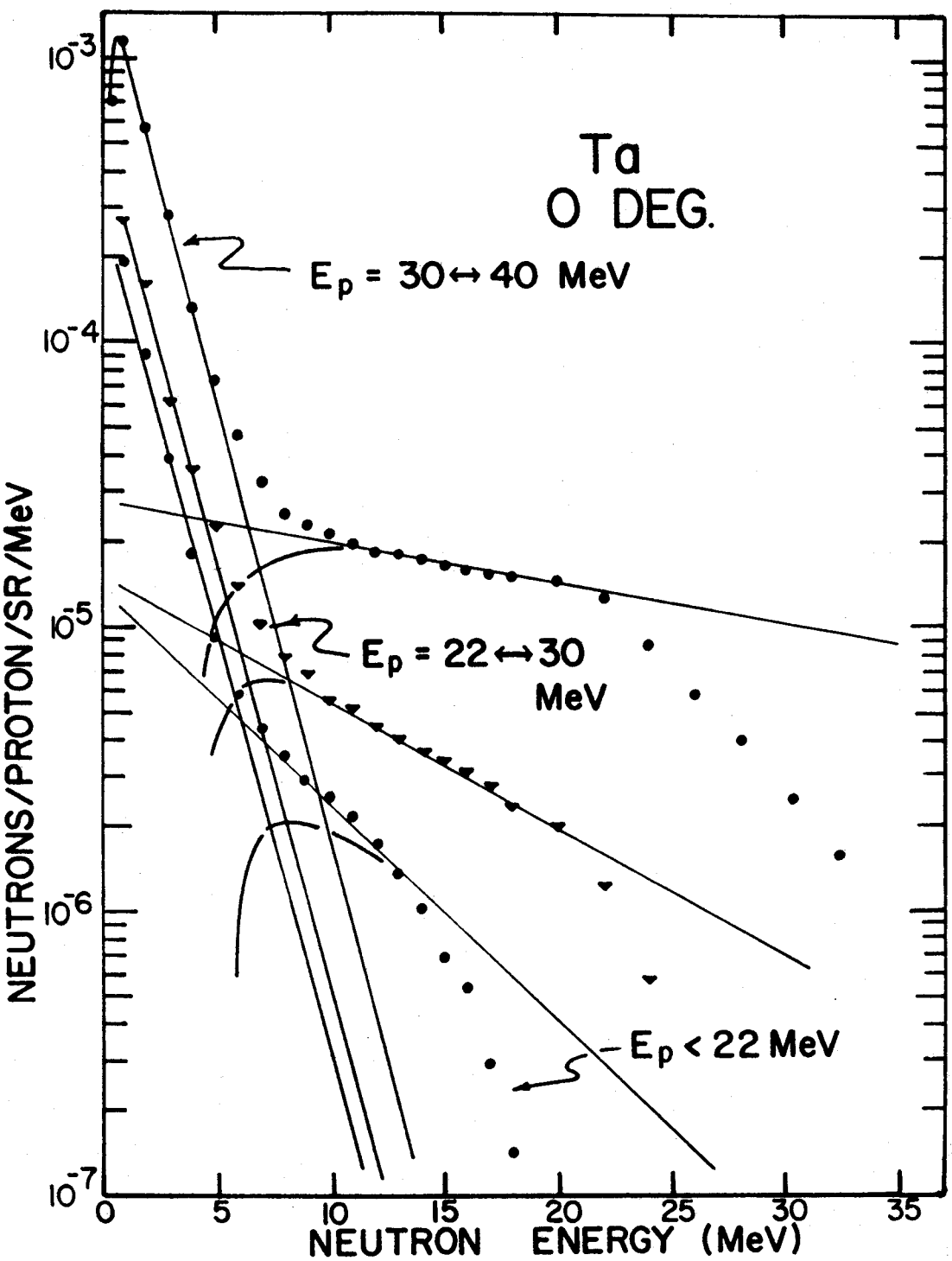

Figure 31. Differential Neutron Energy Spectra with Extrapolated Evaporation Spectra

Subtracting the spectra in such a way presents the data in the most differential form possible. It has the advantage that the bombarding energy is then reasonably well defined for a relatively "thin" target, and facilitates comparison with theory. It is worthwhile to note here that for the heavier targets at 22 MeV, the minimum bombarding energy which can result in significant neutron production is about 14 or 15 MeV, where the incident protons can no longer penetrate the Coulomb barrier. Hence the effective thickness of the targets, 7 or 8 MeV, compares favorably with the other two cases.

Following subtraction, the differential non-compound spectra were integrated over energy to obtain the total non-compound contribution at each angle for each bombarding energy range. These values were then plotted as the angular distributions shown in Figure 32. These angular distributions show a strong angular dependence, dropping off rapidly with increasing angle; this in itself is clear evidence of the non-compound nature of this part of the neutron spectrum. Figure 28 clearly shows the difference between the isotropic evaporation spectrum of neutrons with $E_n < 6$ MeV, and the marked angular variation of the energy spectrum of neutrons with higher energies.

These angular distributions were then integrated over angle to get the total contributions of non-compound reactions to the total neutron yields; which are shown in Figure 33 expressed as percentages of the total neutron yields for each energy range. However, these percentages are not yet the fractions of reactions leading to

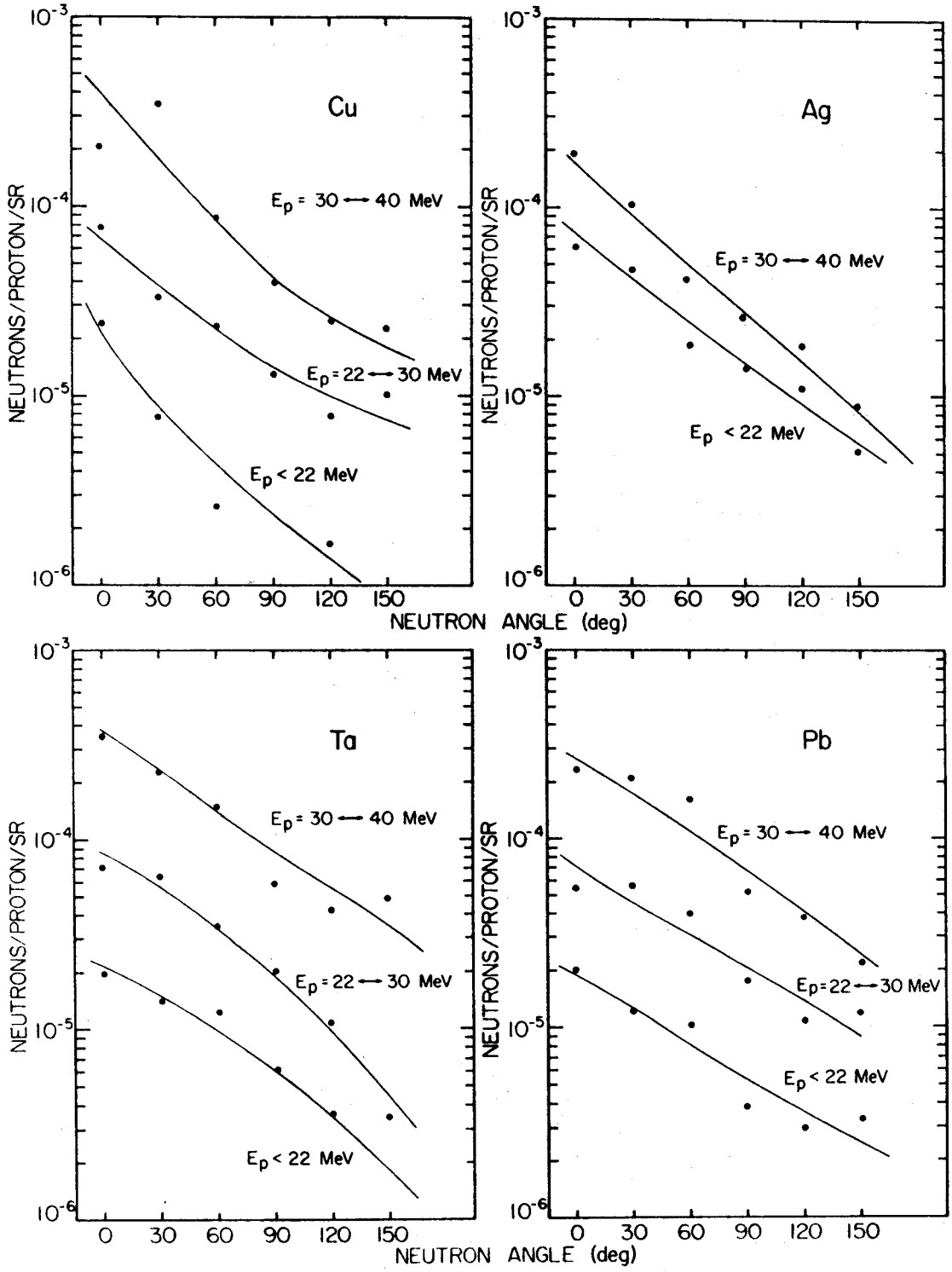

Figure 32. Non-Compound Neutron Angular Distributions

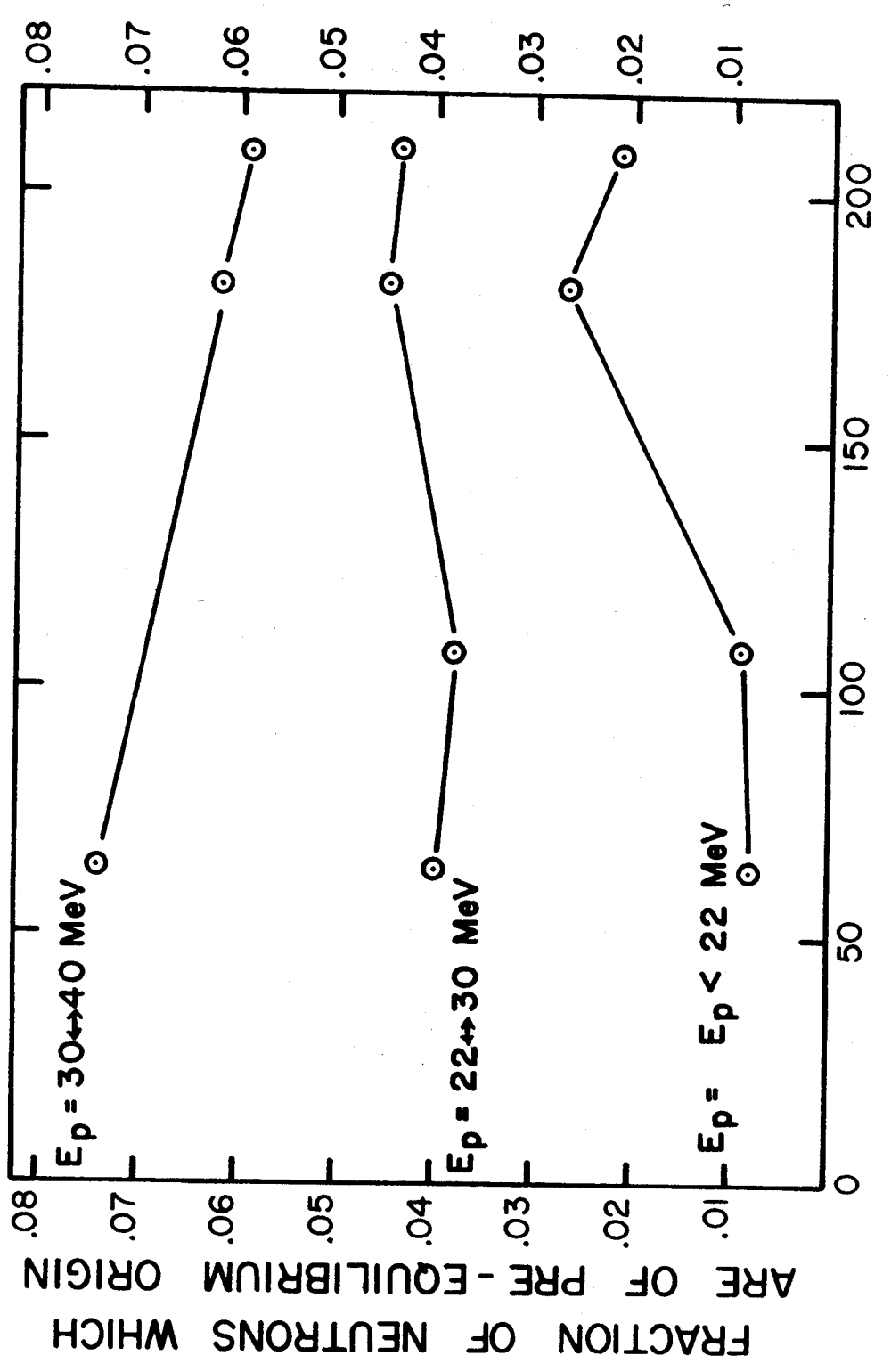

Figure 33. Total Non-Compound Neutron Yields

pre-equilibrium neutron emission occurring in each energy range; one more step is required to obtain these numbers, and the assumptions involved will introduce some model dependence into the analysis of the data in the manner described subsequently. Each compound nucleus which decays strictly by neutron evaporation will emit a number of neutrons; for Ta at 40 MeV, for example, four neutrons will be evaporated, with fewer emitted neurons at lower bombarding energies. This multiple evaporation must be accounted for in obtaining the probability for a nuclear reaction which results in pre-equilibrium neutron emission for each range of bombarding energy. The fractions of non-compound neutrons for each target in each bombarding energy range, as given in Figure 33, multiplied by the neutron evaporation multiplicity for the same case are the desired probability. Any calculation of evaporation multiplicities, by whatever method, must be based upon some assumptions regarding the decay of the equilibrium compound nucleus.

These multiplicities must be calculated somehow, and were in fact calculated by program DECAY as a necessary step in the calculation of the absolute neutron energy spectra used in the previous section. In so far as these multiplicities depend upon the assumptions upon which the calculations were based (and not just energetics), the probability values thus obtained also depend on those assumptions, the main one of which concerns the applicability of the statistical fermi-gas model to the experimental situation.

If this assumption is valid, the results of this procedure should also be valid, with only slight modifications which will be discussed shortly.

Also, in order to obtain values for pre-equilibrium neutron emission which can be compared with Blann's calculations, some estimate of pre-equilibrium proton emission must be made. Pre-equilibrium proton emission affects the values of the neutron multiplicities used in determining the pre-equilibrium neutron emission. Fortunately the dependence of this quantity on the pre-equilibrium proton emission is not too strong, as will be shown in the following example.

Let the probability for pre-equilibrium proton emission, P_p, be some fraction of that for pre-equilibrium neutron emission, P_n such that

$$P_p = xP_n \qquad (V - 1)$$

where x is a number between zero and unity. P_n is here the probability for a nuclear reaction resulting in pre-equilibrium neutron emission, which is obtained for a given case simply by multiplying the fraction of neutrons which are of pre-equilibrium origin as shown in Figure 33, by the appropriate neutron evaporation multiplicity; this evaporation multiplicity must be corrected to account for the competition between pre-equilibrium and compound-nuclear processes, and a new P_n calculated. Then the total pre-equilibrium emission probability is

$$P_{tot} = P_n + P_p = P_n\ (1 + x) \qquad (V - 2)$$

So, if M_o is the evaporation multiplicity obtained from program DECAY, which neglects pre-equilibrium emission, the new corrected multiplicity, M*, can be written as

$$M^* = M_o\ (1 - P_{tot}) + (M_o - 2.0)\ P_n + 1.5\ P_p \qquad (V - 3)$$

The first term accounts for the competition between pre-equilibrium and evaporation processes; the second term accounts for the reduction in the neutron multiplicity caused by removal of large amounts of energy by emitted pre-equilibrium particles. The number 2.0 inside the parentheses in the second term is a hypothetical value typical of the case of 30 to 40 MeV protons incident upon lead or tantalum; in cases such as copper at 22 MeV, where M_o was less than 2.0, 1.0 was used instead. The final term increases the multiplicity to account for pre-equilibrium proton emission, the factor 1.5 allows approximately for the fact that usually one, but seldom more than two neutrons can be evaporated following pre-equilibrium proton emission, at least at the excitation energies common in this experiment.

Finally, if F is the fraction of neutrons which are of pre-equilibrium origin, as shown in Figure 33, and P_n is the probability of a collision resulting in pre-equilibrium neutron emission, then

$$P_n = M^*\ F \qquad (V - 4)$$

The values of P_n obtained in this way are relatively insensitive to the value of x chosen in (V - 1); values of P_n were calculated for each spectrum with x = 0, .33, and 1.0, and in the case of Pb (40 - 30) the corresponding values of P are .235, .210, and .185. The higher and lower values of P_n were taken to be indicative of the errors made in the assumptions upon which the calculations were based. The values of P thus obtained can then be compared with the theoretical values calculated by Blann's theory as shown in Figure 34. The theoretical values were obtained by integrating the calculated pre-equilibrium neutron energy spectrum over energy, and dividing the result by the total reaction cross-section which was also calculated at the same time. As Figure 34 shows, the agreement between experiment and theory is reasonable in the case of Ta, and not quite as good in the case of Cu. Any disagreement is likely explainable by a combination of the following: (1) an error, particularly in the case of Cu, in estimating the effects of pre-equilibrium proton emission on the neutron evaporation multiplicity; (2) at the lowest excitation energy, binding energy effects which cause large fluctions in the pre-equilibrium emission as a function of mass number (Bl 72); (3) assumptions made in extracting the pre-equilibrium spectra from the experimental neutron energy spectra; and (4) need for modifications in the theory. In general, the agreement between the experiment and theory is rather good.

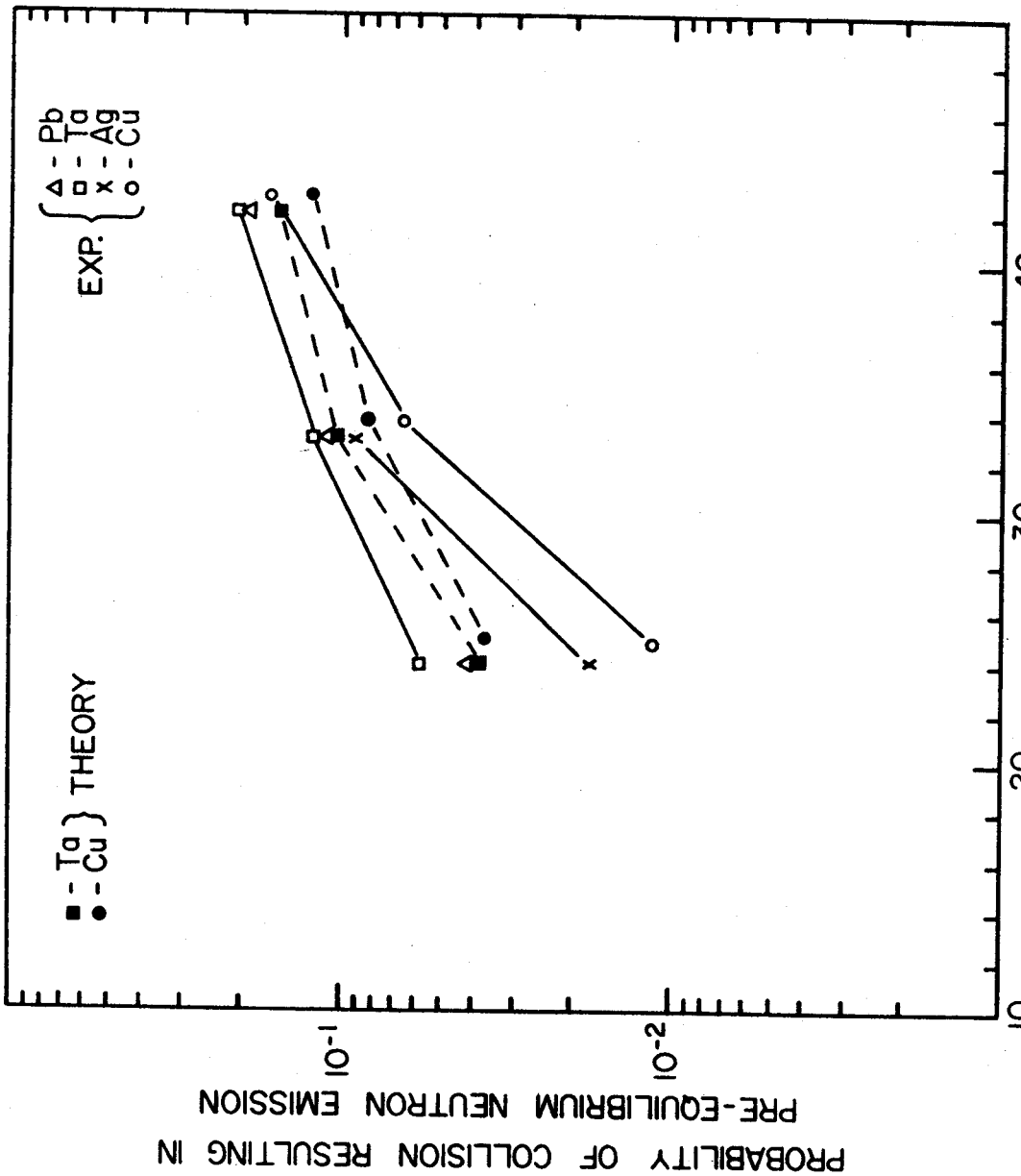

Figure 34. Probability for Collision Resulting in Pre-Equilibrium Neutron Emission

It is also of value to compare the experimental pre-equilibrium spectral shapes with the theoretical spectral shapes predicted by Blann's calculations.

It was mentioned at the beginning of this section that the pre-equilibrium statistical models in their current form cannot predict the angular variation of the pre-equilibrium spectrum. However, calculations have been developed (Bl 72) which do predict the shape of the total neutron spectrum, and these have been used in the analysis of other experimental data (Ve 71). The differential energy spectra were integrated over angle for each target and bombarding energy range to facilitate comparision with theory. The results of theory calculations for Ta and Cu are shown in Figure 35 along with the angular integrated experimental spectra. The theoretical and experimental curves appear to agree reasonably well with each other, apart from a slight difference in slope, which is not too severe. The experimental spectra are composites of many spectra generated over 10 MeV intervals of bombarding energy so it is to be expected that there would be some differences between the measured and calculated spectra. Given this limitation, the theory appears to be in very good qualitative agreement with the data and quite reasonable quantitative agreement as well.

The angular integrated energy spectra for each target and bombarding energy range are shown in Figure 36.

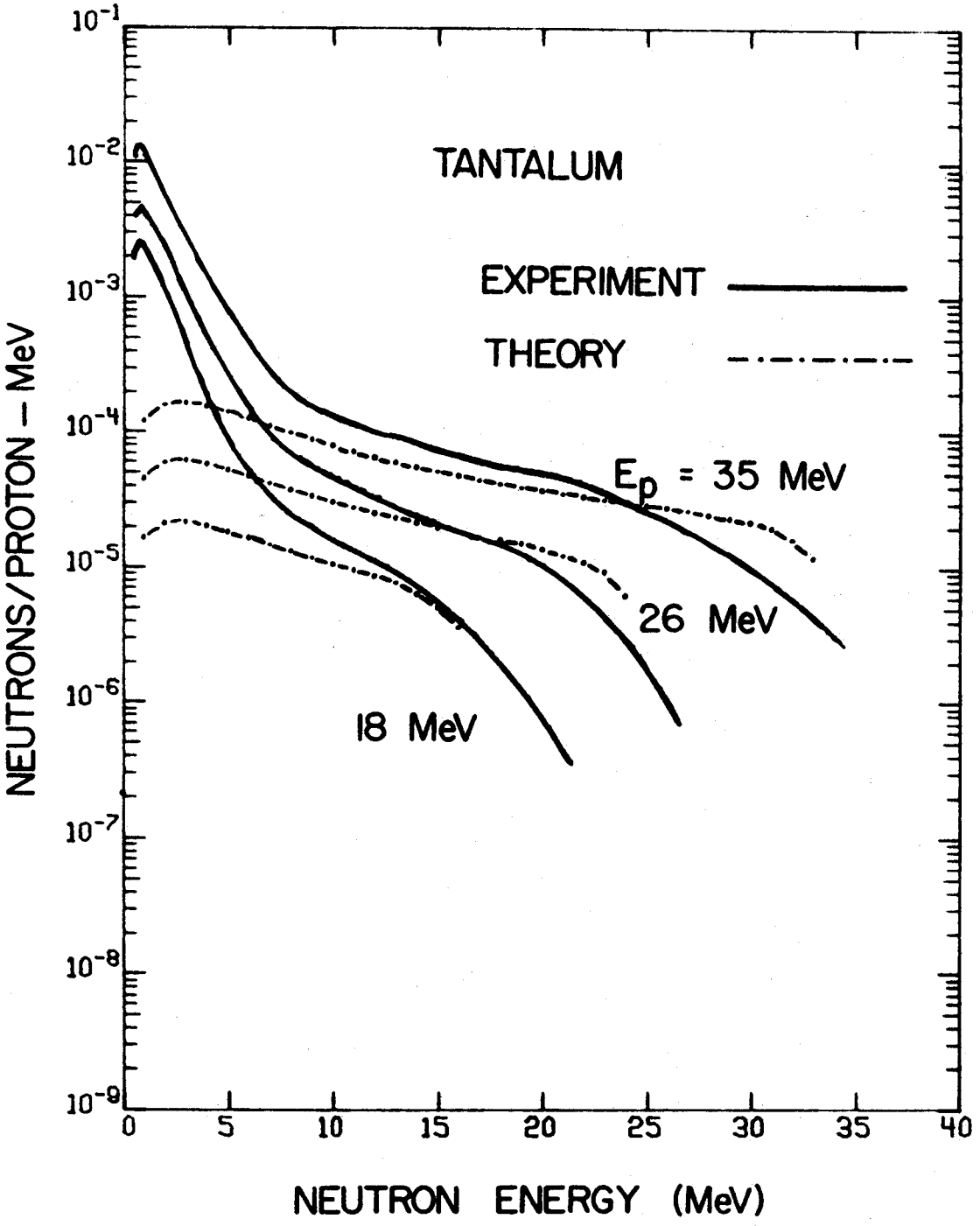

Figure 35. Theoretical and Experimental Angular-Integrated Neutron Energy Spectra

Figure 35. (continued)

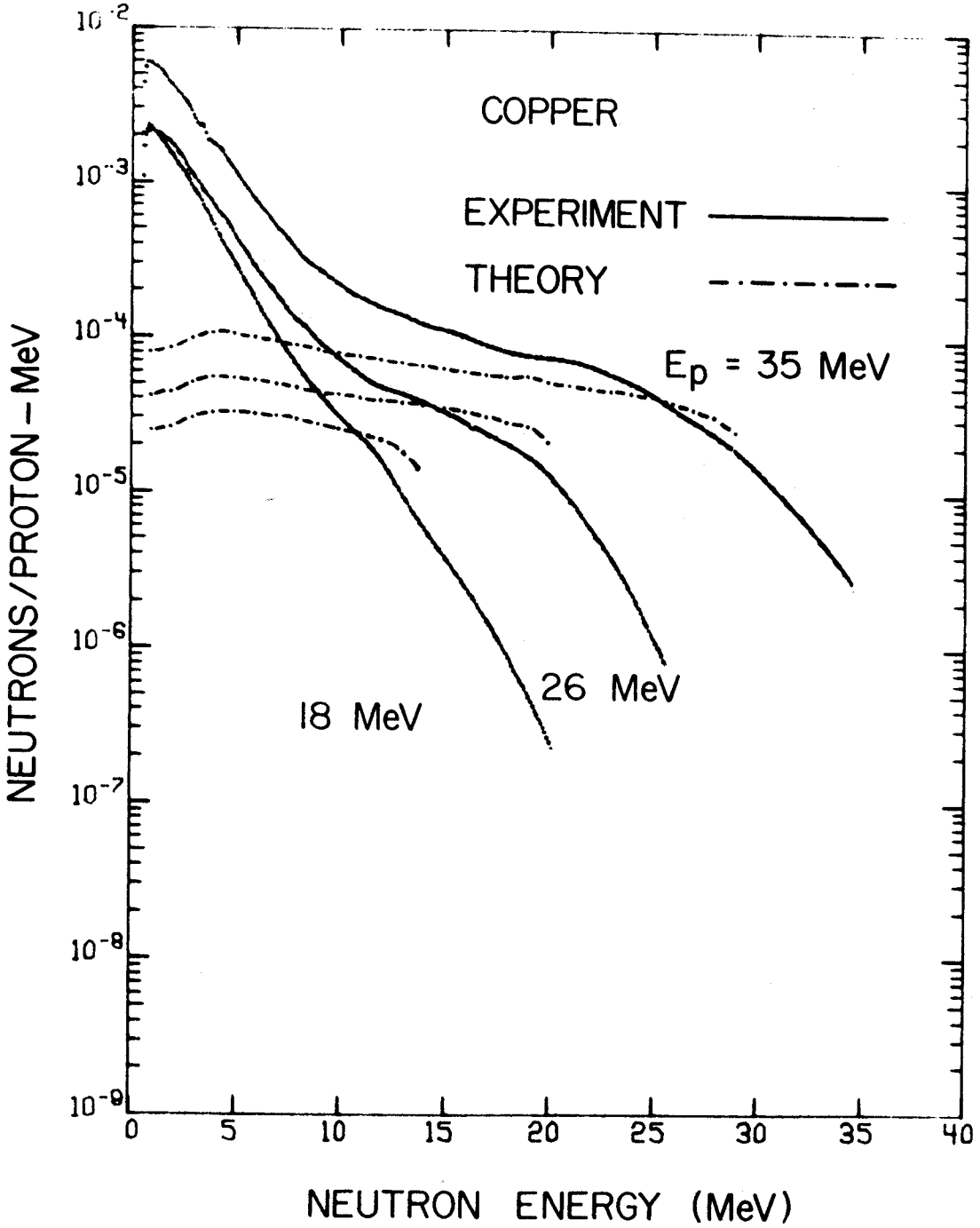

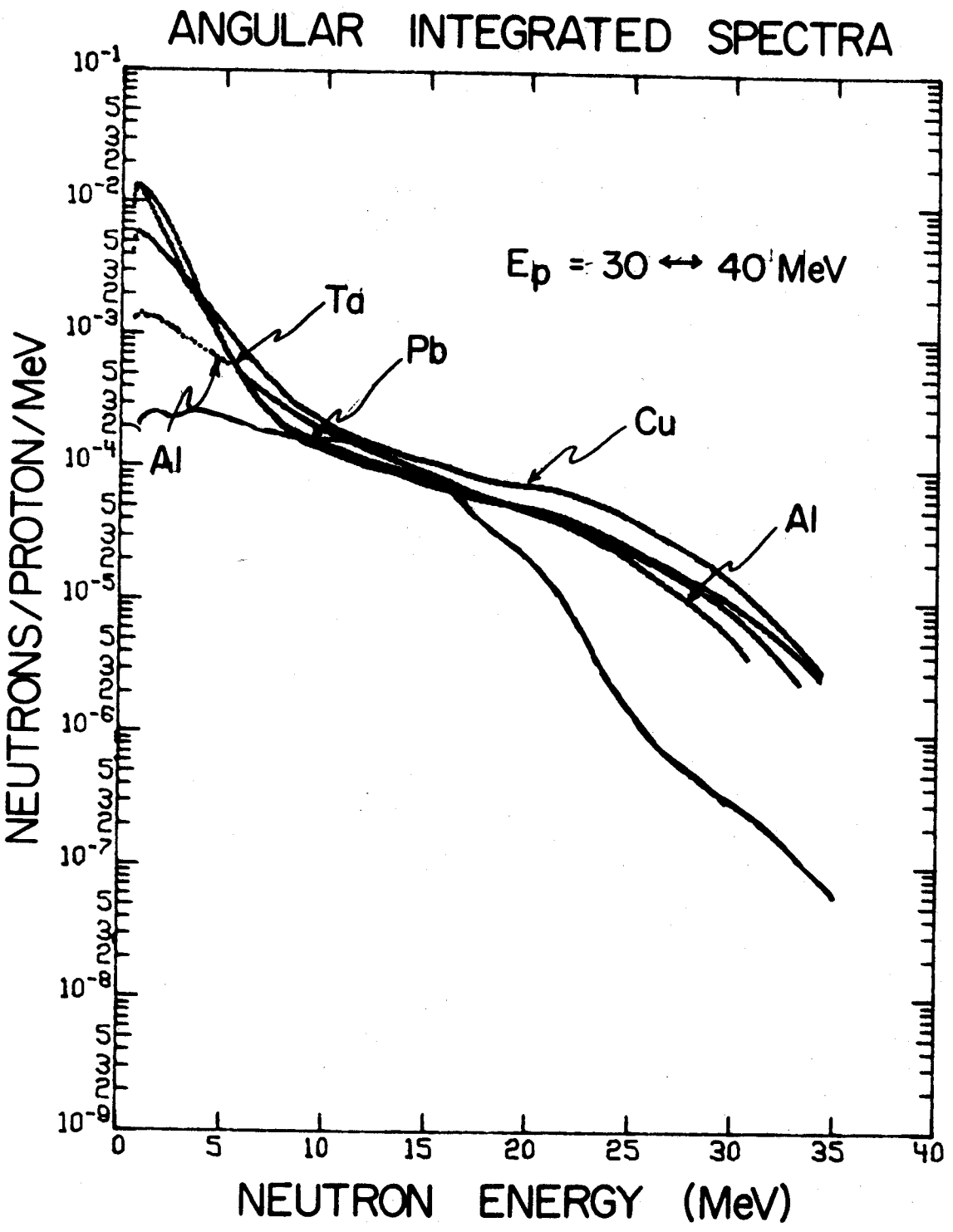

Figure 36. Angular Integrated Neutron Energy Spectra

Figure 36. (continued)

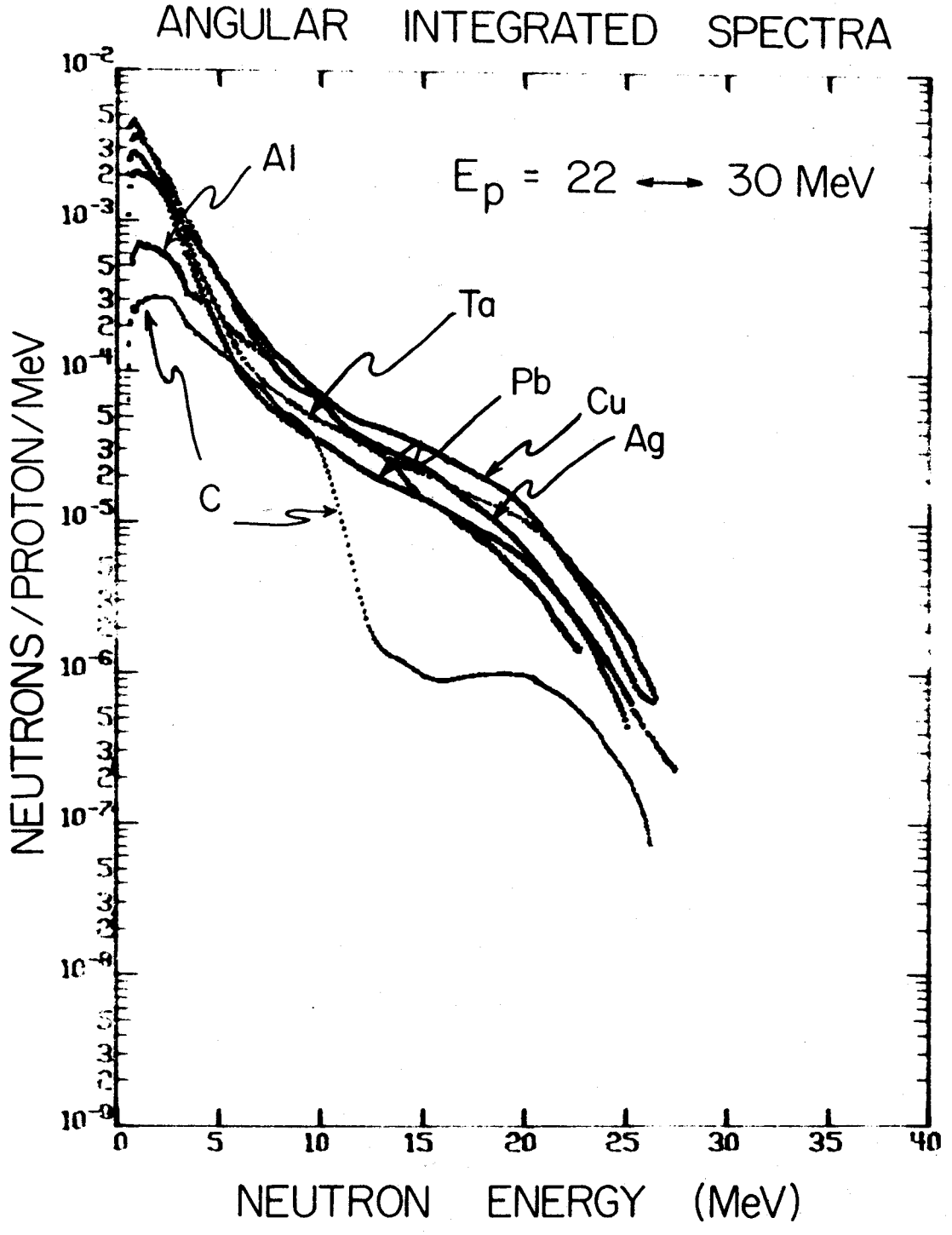

Figure 36. (continued)

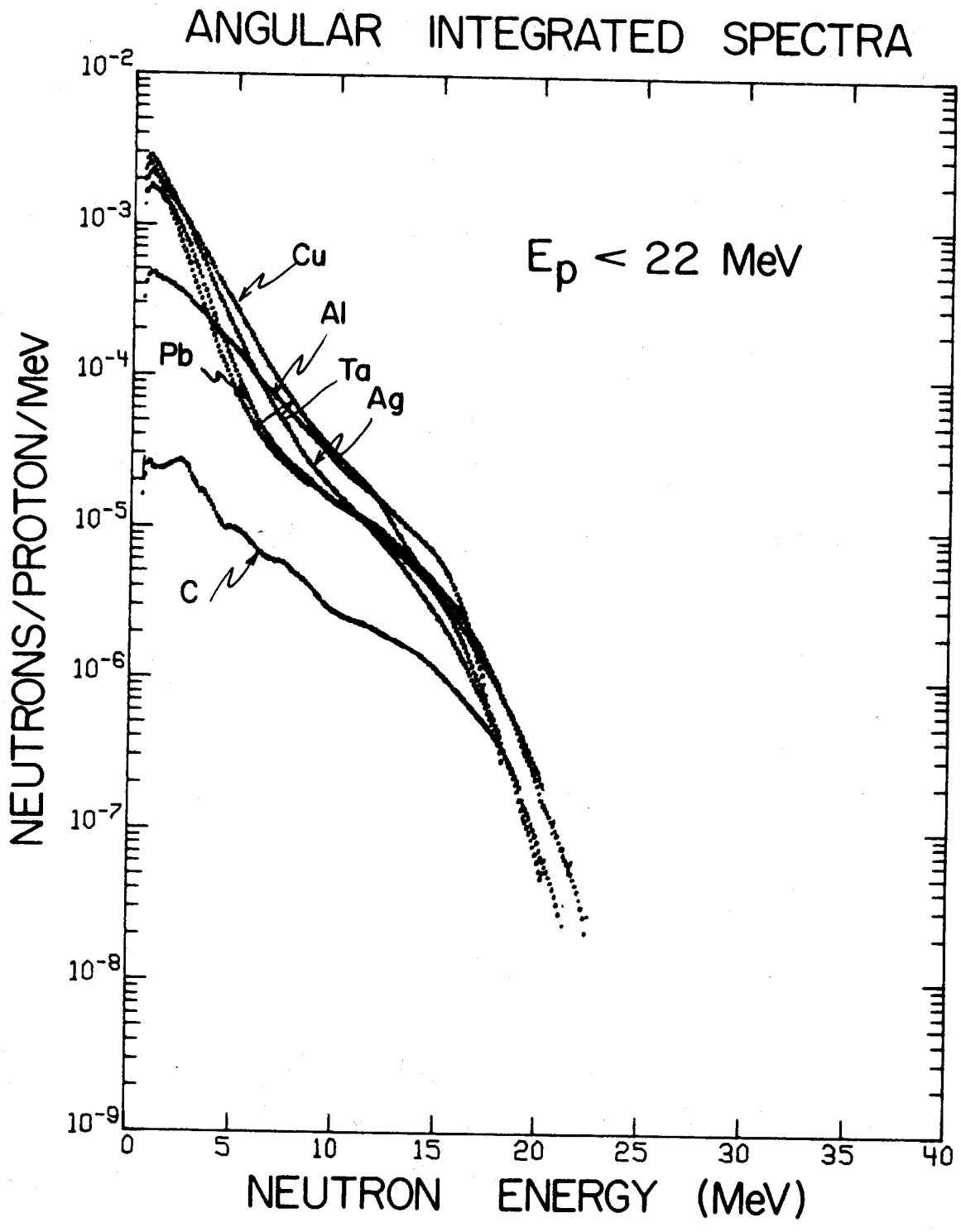

VI. CONCLUSIONS

Neutron yields from proton bombardment of thick targets were measured by the time-of-flight technique at proton energies of 22, 30, and 40 MeV. Time-of-flight spectra were measured for six natural targets -- C, Al, Cu, Ag, Ta, and Pb -- at laboratory angles of 0, 30, 60, 90, 120, and 150 degrees, covering the neutron energy range from 0.5 to 40 MeV. The data are of high quality; the overall experimental energy resolution, a function of the neutron energy, varied from $\pm$ 4% at 0.5 MeV to $\pm$ 2.5% at 40 MeV, and the statistical error was typically four to five percent; the overall experimental error is conservatively estimated to be about 20%, including a $\pm$ 15% error in the calculation of the efficiency of the neutron detector.

The statistical fermi-gas model of the nucleus as developed by LeCouteur appears to be able to describe adequately the neutron evaporation spectra measured in this experiment, at least for nuclei heavier than A = 50, even though emission of several particles is possible. Although determined at higher excitation energies, the values of r_o and a obtained from the foregoing analysis of the evaporation spectra are in quite good quantitative agreement with previous experimental results, and in the case of the level density parameter, are qualitatively in excellent agreement with theory, even to the extent of reproducing shell closure effects in certain of the nuclei investigated. Apart from these shell effects, no pronounced variation of the level density parameter with bombarding (or excitation) energy was noted.

The pre-equilibrium model developed by Blann describes quite well on an absolute basis the measured energy spectra of pre-equilibrium neutrons, and also, therefore the frequency with which pre-equilibrium processes occur, particularly in the heavier nuclei investigated in this experiment. The results of this experiment substantiate in large measure theoretically predicted variations of pre-equilibrium neutron emission with both mass number and excitation energy.

The probability of pre-equilibrium neutron emission determined by this experiment increases rapidly with excitation energy. For instance, the pre-equilibrium neutron emission from Ta increases by more than a factor of four between 22 and 40 MeV of bombarding energy. This is in rough agreement with theory, although detailed comparisons are difficult to make because the theoretical curve rises very steeply in this range of excitation energies. The shapes and magnitudes of the angular-integrated pre-equilibrium neutron spectra do not vary significantly with target mass number. This is true even for the case of ^{27}Al, so that the pre-equilibrium spectra are very similar for the range of mass from 27 to 208, at least in the cases investigated here. In as much as this model is still being developed and refined, it appears likely that modifications to the theory can lead to better agreement between these experimental data and theory, and so to a better understanding of the nuclear equilibration process. Much work is in progress to this end, and the results of this experiment very likely should be valuable in this effort. Further experiments with thin targets or a number of elements spanning the medium and heavy nuclei are highly desirable.

In view of the difficulty in distinguishing between the evaporation and pre-equilibrium neutron energy spectra in light nuclei ($A<50$) further more detailed study of these nuclei along the line of this experiment may lead to improved criteria and methods for determining the two spectral components, not only for light nuclei but for heavy nuclei as well. The results of this experiment indicate a strong need for refinement of both the evaporation and pre-equilibrium theories as applied to light nuclei.

This experiment is ahead of the development of pre-equilibrium models in that the angular distributions of the pre-equilibrium neutrons have been measured and found to be forward peaked, whereas the theoretical models, at their current stage of development, are unable to describe the angular dependence of the data. Every effort has been made to present the data in as useful a format as possible, and it is hoped that they will be of value to physicists -- both experimental and theoretical -- to whom a knowledge of neutron emission from highly excited nuclei is of interest.

REFERENCES

Al 61 K. Alexander and F. Goulding, Nucl. Instr. Meth. 13, 244 (1961).

Ba 71 D. Bayer, MSUCL-34, (Michigan State University, East Lansing, Michigan), 1971.

Be 63 D. Beard and A. McLellan, "Quantitative Theory of Nuclear Evaporation and Its Relation to Nuclear Matter", 1963 (unpublished).

Be 63 H. Bertini, "Monte Carlo Calculations on Intranuclear Cascades", ORNL-3383, 1963 (unpublished).

Bi 51 J. Birks, Proc. Phys. Soc. A64, 874 (1951).

Bl 52 J. Blatt and V. Weisskopf, Theoretical Nuclear Physics, J. Wiley and Sons, New York 1952.

Bl 72 M. Blann and A. Mignerey, Nucl. Phys. A186, 245 (1972).

Bo 36 N. Bohr, Nature 137, 344 (1936).

Bo 62 D. Bodansky, Ann. Rev. Nucl. Sci. 12, 79 (1962).

Bo 69 A. Bohr and B. Mottelson, Nuclear Structure, W. A. Benjamin, Inc., New York 1969.

Cl 71 C. Cline and M. Blann, Nucl. Phys. A172, 225 (1971).

Da 61 W. Daehnick and R. Sherr, Rev. Sci. Instr. 32, 666 (1961).

Ev 55 R. D. Evans, The Atomic Nucleus, McGraw-Hill, New York 1955, page 397.

Fe 50 E. Fermi, Nuclear Physics, J. Orear, A. H. Rosenfeld and R. A. Schluter, Eds. University of Chicago Press, 1950.

Ga 69 G. Garvey, W. Grace, R. Jaffe, I. Talmi and I. Kelson, Rev. Mod. Phys. 41, SI (1969).

Ga 70 D. Garber, L. Stromberg, M. Goldberg, D. Culleo and V. May, "Angular Distributions in Neutron-Induced Reactions, Vol. II, BNL 400 (1970).

Ge 68 D. Gedcke and W. MacDonald, Nucl. Instr. Meth. 58, 253 (1968).

Go 60 J. Gooding and H. Pugh, Nucl. Instr. Meth. 10, 189 (1960).

Gr 66 J. Griffin, Phys. Rev. Lett. 17, 478 (1966).

Gr 71 S. Grimes, J. Anderson, B. Pohl, J. McCuire and C. Wong, Phys. Rev. C 4, 607 (1971).

Ha 62 L. Hansen and R. Albert, UCRL-6686, 1962 (unpublished).

Hu 58 D. Hughes and R. Schwartz, "Neutron Cross Sections", BNL 325, U. S. Government Printing Office, 1958.

Hu 70 J. Hunt, C. Baker, C. Batty, P. Ford, E. Freidman and L. Williams, Nucl. Instr. Meth. 85, 269 (1970).

Ja 66 J. Janni, "Calculations of Energy Loss, Range, Pathlength, Straggling, Multiple Scattering, and the Probability of Inelastic Nuclear Collisions for 0.1 to 1000 MeV Protons", Air Force Weapons Laboratory Technical Report AFWL-TR-65-150 (1966).

Ki 58 C. Kittel, Elementary Statistical Physics, J. Wiley and Sons, New York 1958.

Ku 64 R. Kurz, University of California Report UCRL-11339, 1964 (unpublished).

Ku 67 L. Kull, "An Investigation of (p,d) Reactions in 1p Shell Nuclei", Thesis, Michigan State University, 1967 (unpublished).

La 54 J. Lang and K. LeCouteur, Proc. Phys. Soc. A67, 585 (1954).

La 71 H. Laumer, "Proton Induced Reactions on ^{14}N and ^{16}O and The Creation of Elements Lithium, Beryllium and Boron", Thesis, Michigan State University, 1971 (unpublished).

Le 50 K. LeCouteur, Proc. Phys. Soc. A63, 259 (1950).

Le 52 K. LeCouteur, Proc. Phys. Soc. A65, 718 (1952).

Mi 65 J. Millman and H. Taub, Pulse and Digital Circuits, McGraw-Hill, New York 1965.

Mo 53 P. Morrison, "A Survey of Nuclear Reactions" in Experimental Nuclear Physics, Vol. II, E. Segre, Ed., J. Wiley and Sons, New York 1953.

Ne 56 T. Newton, Can. J. Phys. 34, 804 (1956).

Ow 58 R. Owen, IEEE Trans. Nucl. Sci. NS-5, 198 (1958).

Pr 62 M. Preston, Physics of the Nucleus, Addison-Wesley, New York 1962.

Ra 71 G. Rao, R. Balasubramanian, B. Cohen, C. Fink and J. Degnan, Phys. Rev. C 4, 1855 (1971).

Ro 64 M. Roush, M. Wilson and W. Hornyak, Nucl. Instr. Meth. 31, 112 (1964).

Si 62 V. Sidorov, Nucl. Phys. 35, 253 (1962).

Sj 65 P. Sjolin, Nucl. Instr. Meth. 37, 45 (1965).

Ta 57 Y.-K. Tai, G. P. Millburn, S. N. Kaplan and B. J. Moyer, Phys. Rev. 109, 2086 (1957).

Ta 70 I. Taylor and J. Kalyna, Nucl. Instr. Meth. 88, 767 (1970).

Ve 65 V. Verbinski, J. Courtney, W. Burrus and T. Love, Proc. Amer. Nucl. Soc., Special Session Fast Neutron Spectroscopy, San Francisco (Dec. 1964) Shielding Division Report ANS-SD-2 (unpublished), 189 (1965).

Ve 68 V. Verbinski, W. Burrus, T. Love, W. Zobel, N. Hill and R. Textor, Nucl. Instr. Meth. 65, 8 (1968).

Ve 69 V. Verbinski and W. Burrus, Phys. Rev. 177, 1671 (1969).

We 62 C. Weigand, T. Elioff, W. Johnson, L. Auerbach, J. Lach and T. Ypsilantis, Rev. Sci. Instr. 33, 526 (1962).

Wi 62 C. Williamson, J.-P. Boujot and J. Picard, "Tables of Range and Stopping Power of Chemical Element for Charged Particals of Energy 0.05 to 500 MeV", CEA-Report R 3042, 1962.

Wo 65 R. Wood, R. Borchers and H. Barschall, Nucl. Phys. 71, 529 (1965).

Wr 53 G. Wright, Proc. Phys. Soc. A66, 777 (1953).

Ze 43 M. W. Zemansky, Heat and Thermodynamics, McGraw-Hill, New York 1943.

APPENDIX

```
      PROGRAM DECAY
      DIMENSION SPEC(400),E(400),TERM(16)
      COMMON/BLOCK2/RZERO
      COMMON/TABLE/TGTZ,TGTA,DENS,DX
      COMMON/BLOCK1/PARAM
      COMMON/BLOCK4/SPEC,E
      C=2.99793*10.0**10
      HBAR=6.5828*10.0**(-22)
      PI=3.14159
      READ 1,EP,TGTZ,TGTA,DENS,THICK,RZERO,PARAM
      PRINT 1, EP,TGTZ,TGTA,DENS,THICK,RZERO,PARAM
    1 FORMAT(7F10.4)
C     EP= INCIDENT PROTON ENERGY IN MEV
C     TGTZ = CHARGE OF TARGET NUCLEUS
C     TGTA = MASS NUMBER OF TARGET
C     DENS = DENSITY OF TARGET IN G/CM**3
C      THICK = TARGET THICKNESS IN CM
C     RZERO = NUCLEAR RADIUS PARAMETER IN FERMIS
C     PARAM = FACTOR TO ADJUST LEVEL DENSITY PARAMETER(A/PARAM)
      DUMMY=0.0
      WAP1=0.0
      WAP2=0.0
      DX=THICK/20.0
      JE=EP*10.0
      EPP=EP
      RHOT=DENS*6.02*10.0**23/TGTA
      R=RZERO*TGTA**0.3333333*10.0**(-13)
      FLUX=1.0
      DO 9 I=1,400
      SPEC(I)=0.0
      E(I)=0.0
    9 CONTINUE
   10 CONTINUE
      CALL DEDX(EP,DE)
      EPRIME=EP-0.5*DE
      IF(EPRIME.LE.0.0) GO TO 76
      IE=EPRIME*10.0
      WAVNUM=C*HBAR/((2.0*931.48*EPRIME*EPRIME*EPRIME)**0.5)
      RAD=R+WAVNUM
      COULBAR=TGTZ*10.0**(-13)/RAD
      IF(EPRIME.LE.COULBAR) GO TO 13
      SIGMA=PI*RAD**2*(1.0-COULBAR*R/(EPRIME*RAD))
      DFLUX=FLUX*(1.0-EXP(-RHOT*SIGMA*DX))
      PRINT 2,DFLUX,SIGMA
    2 FORMAT(4X,1PE11.4,4X,E11.4)
C     ASSUME ALL OF FLUX LOSS GOES TO FORM COMPOUND NUCLEUS
      Z=TGTZ+1.0
      A=TGTA+1.0
      IZ=TGTZ
      N=TGTA-TGTZ
      ICHK=MASSTHEO(AMASS1,IZ,N)
      IF(ICHK.EQ.1) GO TO 71
      I=Z
      IN=A-Z
      ICHK=MASSTHEO(AMASS2,I,IN)
      IF(ICHK.EQ.1) GO TO 75
C     COMPOUND NUCLEUS IS (Z,A)
C     COMPUTE AVAILABLE EXCITATION ENERGY FOR FIRST DECAY
      ESTAR=TGTA*EPRIME/A+AMASS1+7.9-AMASS2
```

```
      IF(ESTAR.LE.0.0) GO TO 81
C     CALCULATE RESIDUAL EXCITATION ENERGIES AND TEMPERATURES
C     FOR ALL NUCLEI IN CHAIN
      UN1=UXN(Z,A,ESTAR,TN1)
      UP1=UXP(Z,A,ESTAR,TP1)
      UN2=UXN(Z,A-1.,UN1,TN2)
      UP2=UXP(Z,A-1.,UN1,TP2)
      UN3=UXN(Z-1.,A-1.,UP1,TN3)
      UP3=UXP(Z-1.,A-1.,UP1,TP3)
      UN4=UXN(Z,A-2.,UN2,TN4)
      UP4=UXP(Z,A-2.,UN2,TP4)
      UN5=UXN(Z-1.,A-2.,UP2,TN5)
      UP5=UXP(Z-1.,A-2.,UP2,TP5)
      UN6=UXN(Z-1.,A-2.,UN3,TN6)
      UP6=UXP(Z-1.,A-2.,UN3,TP6)
      UN7=UXN(Z-2.,A-2.,UP3,TN7)
      UP7=UXP(Z-2.,A-2.,UP3,TN7)
      UN8=UXN(Z,A-3.,UN4,TN8)
      UP8=UXP(Z,A-3.,UN4,TP8)
      UN9=UXN(Z-1.,A-3.,UP4,TN9)
      UP9=UXP(Z-1.,A-3.,UP4,TP9)
      UP10=UXN(Z-1.,A-3.,UN5,TN10)
      UP10=UXP(Z-1.,A-3.,TP10)
      UN11=UXN(Z-2.,A-3.,UP5,TN11)
      UP11=UXP(Z-2.,A-3.,UP5,TP11)
      UN12=UXN(Z-1.,A-3.,UN6,TN12)
      UP12=UXP(Z-1.,A-3.,UN6,TP12)
      UN13=UXN(Z-2.,A-3.,UP6,TN13)
      UP13=UXP(Z-2.,A-3.,UP6,TP13)
      UN14=UXN(Z-2.,A-3.,UN7,TN14)
      UP14=UXP(Z-2.,A-3.,UN7,TP14)
      UN15=UXN(Z-3.,A-3.,UP7,UN15)
      UP15=UXP(Z-3.,A-3.,UP7,UP15)
      UN16=UXN(Z,A-4.,UN8,TN16)
      UP16=UXP(Z,A-4.,UN8,TP16)
C     CALCULATE EMISSION PROBABILITIES AND ENERGY SPECTRA
      CALL PROB(PN1,PP1,Z,A,TN1,TP1,ESTAR)
      TERM(1)=PN1
      IF(TERM(1).GT.0.0) CALL SPECTRUM(TERM(1),UN1,DELUX,A-1.)
      PRINT 3, PN1,PP1
    3 FORMAT(4X,'NEUTRON EMISSION PROBABILITY= ',E10.4,4X,
     $'PROTON EMISSION PROBABILITY= ',E10.4)
      CALL PROB(PN2,PP2,Z,A-1.,TN2,TP2,UN1)
      TERM(2)=TERM(1)*PN2
      IF(TERM(2).GT.0.0) CALL SPECTRUM(TERM(2),UN2,DELUX,A-2.)
      PRINT 3, PN2,PP2
      CALL PROB(PN3,PP3,Z-1.,A-1.,TN3,TP3,UP1)
      TERM(3)=PP1*PN3
      IF(TERM(3).GT.0.0) CALL SPECTRUM(TERM(3),UN3,DELUX,A-2.)
      PRINT 3,PN3,PP3
      CALL PROB(PN4,PP4,Z,A-2.,TN4,TP4,UN2)
      TERM(4)=TERM(2)*PN4
      IF(TERM(4).GT.0.0) CALL SPECTRUM(TERM(4),UN4,DELUX,A-3.)
      PRINT 3, PN4,PP4
      CALL PROB(PN5,PP5,Z-1.,A-2.,TN5,TP5,UP2)
      TERM(5)=PN1*PP2*PN5
      IF(TERM(5).GT.0.0) CALL SPECTRUM(TERM(5),UN5,DELUX,A-3.)
      PRINT 3,PN5,PP5
      CALL PROB(PN6,PP6,Z-1.,A-2.,TN6,TP6,UN3)
```

```
      TERM(6)=TERM(3)*PN6
      IF(TERM(6).GT.0.0) CALL SPECTRUM(TERM(6),JN6,DFLUX,A=3.)
      PRINT 3, PN6,PP6
      CALL PROB(PN7,PP7,Z=2.,A=2.,TN7,TP7,JP3)
      TERM(7)=PP1*PP3*PN7
      IF(TERM(7).GT.0.0) CALL SPECTRUM(TERM(7),JN7,DFLUX,A=3.)
      PRINT 3, PN7,PP7
      CALL PROB(PN8,PP8,Z,A=3.,TN8,TP8,JN4)
      TERM(8)=TERM(4)*PN8
      IF(TERM(8).GT.0.0) CALL SPECTRUM(TERM(8),JN8,DFLUX,A=4.)
      PRINT 3,PN8,PP8
      CALL PROB(PN9,PP9,Z=1.,A=3.,TN9,TP9,JP4)
      TERM(9)=TERM(2)*PP4*PN9
      IF(TERM(9).GT.0.0) CALL SPECTRUM(TERM(9),JN9,DFLUX,A=4.)
      PRINT 3, PN9,PP9
      CALL PROB(PN10,PP10,Z=1.,A=3.,TN13,TP10,JN5)
      TERM(10)=TERM(5)*PN10
      IF(TERM(10).GT.0.0) CALL SPECTRUM(TERM(10),JN10,DFLUX,A=4.)
      PRINT 3, PN10,PP10
      CALL PROB(PN11,PP11,Z=2.,A=3.,TN11,TP11,JP5)
      TERM(11)=TERM(1)*PP2*PP5*PN11
      IF(TERM(11).GT.0.0) CALL SPECTRUM(TERM(11),JN11,DFLUX,A=4.)
      PRINT 3, PN11,PP11
      CALL PROB(PN12,PP12,Z=1.,A=3.,TN12,TP12,JN6)
      TERM(12)=TERM(6)*PN12
      IF(TERM(12).GT.0.0) CALL SPECTRUM(TERM(12),JN12,DFLUX,A=4.)
      PRINT 3, PN12,PP12
      CALL PROB(PN13,PP13,Z=2.,A=3.,TN12,TP12,JP6)
      TERM(13)=TERM(3)*PP6*PN13
      IF(TERM(13).GT.0.0) CALL SPECTRUM(TERM(13),JN13,DFLUX,A=4.)
      PRINT 3,PN13,PP13
      CALL PROB (PN14,PP14,Z=2.,A=3.,TN14,TP14,JN7)
      TERM(14)=TERM(7)*PN14
      IF(TERM(14).GT.0.0) CALL SPECTRUM(TERM(14),JN14,DFLUX,A=4.)
      PRINT 3, PN14,PP14
      CALL PROB(PN15,PP15,Z=3.,A=3.,TN15,TP15,JP7)
      TERM(15)=PP1*PP3*PP7*PN15
      IF(TERM(15).GT.0.0) CALL SPECTRUM(TERM(15),JN15,DFLUX,A=4.)
      PRINT 3,PN15,PP15
      CALL PROB(PN16,PP16,Z,A=4.,TN16,TP16,JN8)
      TERM(16)=TERM(8)*PN16
      IF(TERM(16).GT.0.0) CALL SPECTRUM(TERM(16),JN16,DFLUX,A=5.)
      PRINT 3,PN16,PP16
      ACCUM=0.0
      DO 81 I=1,16
      ACCUM=ACCUM+TERM(I)
   81 CONTINUE
      PROB=ACCUM
      PRINT 4,PROB,EPRIME
    4 FORMAT(4X,'NUMBER OF NEUTRONS EMITTED= ',F5.2,'AT ',F5.2,' MEV')
      SERM=DFLUX*PROB
      DUMMY=DUMMY+SERM
      EP=EP+DE
      IF(EP.LE.0.0) GO TO 76
      FLUX=FLUX+DFLUX
      XAP1=XAP1+PROB*DFLUX
      XAP2=XAP2+DFLUX
      IF(EPRIME.LT.COULBAR) GO TO 13
      IF(EPP.LE.22.0) GO TO 10
```

```
      IF(EPP.LE.30.0.AND.EP.LE.22.0) GO TO 13
      IF(EP.LE.(EPP-10.0)) GO TO 13
      GO TO 10
   76 PRINT 8,DUMMY
    8 FORMAT(4X,'TOTAL NEUTRON YIELD= ',F6.4,' NEUTRONS/PROTON')
      ACC=0.0
   77 DO 72 I=1,JE
      SPEC(I)=SPEC(I)/(4.0*PI)
      PRINT 6, E(I),SPEC(I)
    6 FORMAT(4X,F5.2,1PE11.4)
      ACC=ACC+SPEC(I)*0.1
   72 CONTINUE
      ACC=ACC*4.0*PI
       PRINT 7, ACC
    7 FORMAT(4X,'INTEGRATED ENERGY SPECTRUM = ',F6.4,' NEUTRONS/PROTON')
      GO TO 80
   13 CONTINUE
      PLICITY=AMAP1/AMAP2
      PRINT 11,PLICITY,EPP,EP
   11 FORMAT(5X,'AVERAGE NEUTRON MULTIPLICITY=',F4.2,2X,'BETWEEN',2X,
     $F5.2,2X,'AND',2X,F5.2,2X,'MEV')
      AMAP1=0.0
      AMAP2=0.0
      EPP=EP
      IF(EP.LE.22.0)  EPP=22.0
      IF(EPRIME.LT.COULBAR) GO TO 76
      GO TO 10
   71 PRINT 5,IZ,N
      GO TO 80
   75 PRINT 5,I,IN
    5 FORMAT(4X,'NUCLEUS Z = ',I2,'N =',I3,' IS NOT IN TABLE')
   80 END
```

```
      SUBROUTINE PROB(PN,PP,Z,A,T1,T2,EX)
      COMMON/BLOCK1/PARAM
      TEMPP=SP(Z,A)
      IF(TEMPP.EQ.(-1000.0)) GO TO 50
      TEMPN=SN(Z,A)
      IF(TEMPN.EQ.(-1000.0)) GO TO 50
      BARR=VP(Z,A)
      AMBDAL=2.0*(A/PARAM)**0.5
      IF(EX.LE.0.0) GO TO 50
      PRINT 2, Z,A,TEMPP,TEMPN,BARR,EX
    2 FORMAT(4X,'Z=',I2,' A=',I3,' SP=',F6.2,'SN=',F6.2,' BARRIER=',
     $F6.2,' EX=',F6.2)
      RP=EX-TEMPP-BARR
      RN=EX-TEMPN
      IF(RP.LT.1.7*T2) GO TO 30
      RATIO=(RN/RP)**0.25*EXP(AMBDAL*(RN**0.5-RP**0.5))
      PN=RATIO/(RATIO+1.0)
      PP=1.0/(RATIO+1.0)
      IF(PP.LT.0.05) GO TO 10
      IF(PN.LT.0.05) GO TO 20
      RETURN
   10 PP=0.0
      PN=1.0
      RETURN
   20 PP=1.0
      PN=0.0
      RETURN
   30 PP=0.0
      RN=EX-TEMPN
      IF(RN.LT.1.7*T1) GO TO 40
      PN=1.0
      RETURN
   40 PN=0.0
      RETURN
   50 PN=0.0
      PP=0.0
      RETURN
      END
```

```
      FUNCTION UXP(Z,A,U,T)
      COMMON/BLOCK1/PARAM
      TEMP=SP(Z,A)
      IF(TEMP.EQ.(-1000.0)) GO TO 20
      EX=U-TEMP-VP(Z,A)
      IF(EX.LE.0.0) GO TO 20
      T=(-1.7+ SQRT(2.89+4.0*A*EX/PARAM))*PARAM/A/2.0
      UXP=EX-1.7*T
      IF(UXP.LT.0.0) GO TO 20
      RETURN
   20 UXP=0.0
      T=0.0
      RETURN
      END
```

```
      FUNCTION UXN(Z,A,U,T)
      COMMON/BLOCK1/PARAM
      TEMP=SN(Z,A)
      IF(TEMP.EQ.(-1000.0)) GO TO 20
      EX=U-TEMP
      IF(EX.LE.0.0) GO TO 20
      T=(-1.7+ SQRT(2.89+4.0*A*EX/PARAM))*PARAM/A/2.0
      UXN=EX-1.7*T
      IF(UXN.LT.0.0) GO TO 20
      RETURN
   20 UXN=0.0
      T=0.0
      RETURN
      END
```

```
      FUNCTION SP(Z,A)
      IZ=Z
      IN=A-Z
      ICH1=MASSTHEO(AMASS1,IZ,IN)
      IF(ICH1.EQ.1) GO TO 10
      JZ=Z+1.0
      ICH2=MASSTHEO(AMASS2,JZ,IN)
      IF(ICH2.EQ.1) GO TO 10
      SP=AMASS2+7.9-AMASS1
      RETURN
   10 SP=-1000.0
      RETURN
      END
```

```
      FUNCTION SN(Z,A)
      IZ=Z
      IN=A-Z
      ICHK1= MASSTHES(AMASS1,IZ,IN)
      IF(ICHK.EQ.1) GO TO 10
      JN=IN-1
      ICHK2=MASSTHES(AMASS2,IZ,JN)
      IF(ICHK2.EQ.1) GO TO 10
      SN=AMASS2+8.1-AMASS1
      RETURN
   10 SN=-1000.0
      RETURN
      END
```

```
      FUNCTION VP(Z,A)
      COMMON/BLOCK2/RZERO
      VP=Z/(RZERO*A**(0.3333333))
      RETURN
      END
```

```
      SUBROUTINE DEDX(E,DE)
      COMMON/TABLE/TGTZ,TGTA,DENS,DX
C     TGTZ IS TARGET CHARGE
C     TGTA IS TARGET MASS NUMBER
C     E IS PARTICLE ENERGY
C     PRM IS PARTICLE MASS(=1.0)
C     PTZ IS PARTICLE CHARGE (=1.0)
      PRM=1.0
      PTZ=1.0
      Z=TGTZ
      A=931.478
      A=1.0+(1.0/((E/A)**2+2.0*E/A))
      BETAS2=1.0/A
      BETA=BETAS2**(0.5)
C     QMAX IS MAXIMUM MOMENTUM TRANSFER TO ELECTRON FROM INCIDENT PARTICLE
      QMAX=1.022/((1.0/BETAS2-1.0)*(1.0+1.0/1835.0)**2+(1.0+2.0*E/(1836.
     $**31.441)))
C     XION IS AVERAGE IONIZATION ENERGY OF TARGET MATERIAL
      XION=1.0
      IF(Z.LT.2.) GO TO 8
      XION=XION+0.25*EXP(-100.0/Z)
    8 XION=XION*EXP(Z**(-0.6666667)-8.33/(Z*Z)+25.0402/(Z*Z*Z)-18.3840/(
     $Z*Z*Z*Z))
      XION=XION*Z*11.80E-06
      AY=(1.022*QMAX/(1.0/BETAS2-1.0))**0.5/XION
      A=137.037*BETA*1.253314
      B=EXP(-A)
      A=EXP(A)
      ZI=(A-B)/(A+B)
C     ZI IS THE EMPIRICALLY CORRECTED CHARGE OF THE PARTICLE
      RHO=1.0+0.035*(1.0+SQRT(Z))
      RHOI=1.0/RHO
C     DENSITY CORRECTION DELTA IS IGNORED
      DELTA=0.0
      DEDX=0.30711*Z*ZI*ZI/(TGTA*BETAS2)
      DEDX=DEDX*(ALOG(AY/(1.0+EXP(-(AY**RHOI))))**RHO)-BETAS2+DELTA)
      DE=DEDX*DENS*DX
      PRINT 1,DE
    1 FORMAT(4X,'DE= 'F5.2,' MEV')
      RETURN
      END
```

```
      SUBROUTINE SPECTRUM (P,EMX,DFLUX,A)
      COMMON/BLOCK1/PARAM
      COMMON/BLOCK4/SPEC,E
      DIMENSION E(400),SPEC(400),DUMMY(400)
    4 FORMAT(4(4X,E10.4))
      IF (EMX.LE.0.0) GO TO 11
      ANORM=P*DFLUX
      APRIME=A/PARAM
      SUM=0.0
      IE=10.0*EMX
      IF(IE.LE.0) GO TO 11
      DO 10 I=1,IE
      E(I)=0.1*I-0.05
      TEMP=EMX-E(I)
      DUMMY(I)=E(I)*EXP(2.0*SQRT(APRIME*TEMP))
      SUM=SUM+0.1*DUMMY(I)
   10 CONTINUE
      DO 20 I=1,IE
      SPEC(I)=SPEC(I)+ DUMMY(I)*ANORM/SUM
   20 CONTINUE
   11 RETURN
      END
```